DYNAMIC LIGHT SCATTERING STUDY OF FLEXIBLE LIQUID CRYSTALLINE N-MERS THAT FORM THE TWIST-BEND NEMATIC PHASE

A dissertation submitted

to Kent State University in partial

fulfillment of the requirements for the

degree of Doctor of Philosophy

by

Zeinab Parsouzi Azad Sharabiani

August 2019

Dissertation written by

Zeinab Parsouzi Azad Sharabiani

B.S., Kharazmi University, IRAN, 2006

M.S., Amirkabir University of Technology (Tehran Polytechnic), IRAN, 2009

M.A., Kent State University, USA, 2017

PhD, Kent State University, USA, 2019

Approved by

Dr. Samuel Sprunt _____, Chair, Doctoral Dissertation Committee

Dr. James T. Gleeson _____, Members, Doctoral Dissertation Committee

Dr. Antal Jakli _____

Dr. Kambiz Ghazinour_____

Dr. Min-Ho Kim _____

Accepted by

Dr. James T. Gleeson _____, Chair, Department of Physics

Dr. James L. Blank _____, Dean, College of Arts and Sciences

TABLE OF CONTENTS

TABLE OF CONTENTS……...III

LIST OF FIGURES……...VIII

DEDICATION.....**XIX**

ACKNOWLEDGEMENTS .....**XX**

CHAPTER 1 INTRODUCTION..... **1**

1.1 INTRODUCTION TO LIQUID CRYSTALS 1

1.2 CLASSIFICATION ACCORDING TO MOLECULAR ORDER..... 2

1.3 NEMATIC PHASE..... 3

1.3.1 UNIAXIAL AND BIAXIAL NEMATIC..... 3

1.3.2 CHIRAL NEMATIC (CHOLESTERIC)..... 5

1.3.3 TWIST-BEND NEMATIC PHASE 7

1.4 ELEMENTARY SMECTIC PHASES..... 11

1.4.1 SMECTIC A:..... 11

1.4.2 SMECTIC C:..... 12

1.5 DYNAMIC LIGHT SCATTERING..... 13

1.6 HYDRODYNAMIC MODES: 13

1.7 DYNAMIC LIGHT SCATTERING FROM LIQUID CRYSTALS 15

1.8 SCOPE AND OBJECTIVE OF THIS DISSERTATION..... 15

1.9 REFRENCES: 17

CHAPTER 2 BASICS OF DYNAMIC LIGHT SCATTERING..... **23**

2.1 INTRODUCTION 23
2.2 THEORY OF QUASI-ELASTIC LIGHT SCATTERING (QELS) 24
2.3 DIGITAL PHOTON CORRELATION 28
2.4 LIGHT SCATTERING FROM DIRECTOR FLUCTUATIONS IN A UNIAXIAL NEMATIC PHASE 30
2.4.1 ELASTIC FREE ENERGY OF A UNIAXIAL NEMATIC PHASE AND NORMAL MODES 30
2.4.2 DYNAMICS OF THE DIRECTOR MODES 33
2.4.3 OPTICAL SELECTION RULES FOR UNIAXIAL NEMATIC 35
2.4.4 RELATION OF SCATTERING VECTOR TO INCIDENT AND SCATTERING ANGLES IN THE LIGHT SCATTERING EXPERIMENT 37
2.5 EXPERIMENTAL SET UP FOR DYNAMIC LIGHT SCATTERING 39
2.5.1 OVEN AND HOT STAGE WITH OPTICAL ACCESS FOR LIGHT SCATTERING 42
2.5.2 LASER LIGHT SOURCE 45
2.5.3 POWER METER 46
2.5.4 LONG DISTANCE OPTICAL MICROSCOPE 46
2.5.5 The GPX TIME–DIGITIZING CORRELATOR AND PHOTODETECTORS 47
2.6 REFRENCES 50

CHAPTER 3 FLUCTUATION MODES OF A TWIST-BEND NEMATIC LIQUID CRYSTAL 53

3.1 INTRODUCTION 53

3.2 CHEMICAL STRUCTURES OF STUDIED MATERIALS 55

3.3 EXPERIMENTAL LIGHT SCATTERING GEOMETRIES 58

3.3.1 GEOMETRY G1 58

3.3.2 GEOMETRY G2 60

3.4 DLS RESULTS FOR DIFFERENT GEOMETRIES 62

3.4.1 RESULTS FOR GEOMETRY G1 62

3.4.2 RESULTS FOR GEOMETRY G2 65

3.5 THEORETICAL MODEL AND COMPARISON TO EXPERIMENTAL RESULTS 74

3.5.1 FLUCTUATION MODES IN THE NEMATIC PHASE 78

3.5.2 COMPARISON OF THEORY TO EXPERIMENTAL RESULTS FOR THE NEMATIC PHASE 80

3.5.3 FLUCTUATION MODES IN THE TWIST-BEND NEMATIC PHASE 82

3.5.4 COMPARISON OF THEORY TO EXPERIMENTAL RESULTS FOR THE TWIST-BEND PHASE 88

3.6 SUMMARY 92

3.7 REFERENCES 93

CHAPTER 4 LIGHT SCATTERING STUDY OF THE "PSEUDO- LAYER" COMPRESSION ELASTIC CONSTANT IN A TWIST-BEND LIQUID CRYSTAL 95

4.1 INTRODUCTION 96

4.2 LIGHT SCATTERING GEOMETRY 98

4.3 RESULTS AND DISCUSSION 102

4.3.1 LIGHT SCATTERING CORRELATION FUNCTION 102

4.3.2 RELAXATION RATES VERSUS ROCKING ANGLE χ 104

4.3.3 RELAXATION RATE VERSUS SCATTERING ANGLE θ 107

4.3.4 TEMPERATURE DEPENDENCE OF THE PSEUDO-LAYER COMPRESSION MODULUS $\boldsymbol{Beff}$ 110

4.4 SUMMARY 115

4.5 REFERENCES 116

CHAPTER 5 PRETRANSITIONAL BEHAVIOR OF VISCOELASTIC PARAMETERS AT THE NEMATIC TO TWIST-BEND NEMATIC TRANSITION IN FLEXIBLE N-MERS 118

5.1 INTRODUCTION 118

5.2 EXPERIMENTAL DETAILS 119

5.2.1 STUDIED MATERIALS 119

5.2.2 LIGHT SCATTERING PROCEDURE AND GEOMETRIES 122

5.3 RESULTS 127

5.4 DISCUSSION 136

5.5 SUMMARY 143

5.6 REFERENCES 144

CHAPTER 6 CONCLUSION 147

LIST OF FIGURES

Figure 1-1: Molecular structure of 4-cyano-4´-pentylbiphenyl (5CB). 3

Figure 1-2: (a) uniaxial nematic; (b) biaxial nematic(from: C. T. Imrie and P. A. Henderson, "Liquid crystal dimers and higher oligomers: Between monomers and polymers," *Chem. Soc. Rev.*, vol. 36, no. 12, pp. 2096–2124, 2007) [9]. 4

Figure 1-3: Splay, twist, and bend of uniaxial nematic directors (image by N.J. Mottram, University of Strathclyde, 2010, https://www.slideshare.net/nigelmottram/nonlocal-effects-in-models-of-liquid-crystal-materials)..... 5

Figure 1-4: Twisting of the cholesteric phase, p is the pitch(Source: http://barrett group.mcgill.ca/tutorials/liquid_crystal/LC03.htm)[10]. 6

Figure 1-5: (a) DTC5C9 dimer, I 162°C N 124°C N_{TB} 85°C (SmX) 77°C Cr, (b) DTC5-C9-DTC-C9-DTC5 trimer, I 192°C N 145°C N_{TB}, (c) DTC5-C9-DTC-C9-DTC-C9-DTC5 tetramer, I 205°C N 168°C N_{TB}. 7

Figure 1-6: Schematics of director arrangement in (a) N phase (b) N_{TB} phase (c) Cholesteric N^* Phase (image by: V. Borshch *et al.*, 2013) [13]. (d) Showing heliconical director n in N_{TB} phase with cone angle β, helical pitch $p0$ and helical polarization field P. 9

Figure 1-7: POM textures of CB7CB under cross polarizers showing uniformly aligned, N_{TB} phases with focal conic domains. The direction of rubbing is shown by the axis r (source: G. Babakhanova *et al.*, 2017) [34]..... 10

Figure 1-8: FFTEM textures and corresponding Fast Fourier transform (FFT) patterns of CB7CB in N_{TB} phase with uniform structure. The pitch is 8.05 nm viewed in the planes parallel to the optic axis. The arrows in figure point towards domain boundaries of average extension 26 nm, which are roughly perpendicular to the N_{TB} layers. Presence of domains is also revealed by a diffuse intensity pattern in FFT, marked by a white arrow(image by: by: V. Borshch *et al.,* 2013) [13]..... 11

Figure 1-9: Schematic representation of smectic liquid crystal phases, left: smectic A; right: smectic C [37]. 12

Figure 2-1: Light of incident polarization $\boldsymbol{i}$ and wave vector ki with center frequency ωi is scattered in all direction from a transparent medium and arrives at the detector at position r with respect to the center of illuminated volume with wave vector kf, center frequency ωf, polarization f, and scattering vector $q = kf - ki$. The total radiated field at the detector is the superposition of the fields radiated from all infinitesimal volumes $d3r'$ at position $r'$with respect to the center of the illuminated volume. In quasi-elastic scattering $\omega i = \omega f$ and $ki2 = kf2$(Source: Reproduced from K. P. Neupane PhD dissertation 2009 [6])..... 25

Figure 2-2: Coordinate system that illustrates the normal modes of the director for uniaxial nematic liquid crystal (Source: reproduced from T. Ostapenko PhD dissertation, 2011 [16]). 31

Figure 2-3: DLS set-up with planar cell alignment. ki, kf are incident and scattering wave vector. i, f are polarization of incident and scattering light. 38

Figure 2-4: Schematic diagram of the experimental light scattering apparatus set up. 40

Figure 2-5: Photograph of dynamic light scattering set up in the lab. 41

Figure 2-6: Custom made oven for sample cell 43

Figure 2-7: temperature controller Model PTC10 44

Figure 2-8: Left: Rotation stage in DLS set-up. Right: Instec hot stage model HCS400. 45

Figure 2-9: Genesis^{TM} MX STM/SLM laser and power supply(Image from: https://www.coherent.com/lasers/laser/genesis-mx-slm-series)..... 45

Figure 2-10: Ophir Photonics Orion laser power/energy meter..... 46

Figure 2-11: Long distance optical microscope. 47

Figure 2-12: Diagram shows Auto-correlation in DLS set-up..... 48

Figure 2-13: Diagram shows Cross-correlation in DLS set-up. 49

Figure 3-1: Chemical structure of the monomer (top) and dimer (bottom) compounds utilized for the present study. The 70/30 wt% mixture exhibits a N-N_{TB} phase transition at 94.2 °C. 56

Figure 3-2 [8]: Polarizing microscope textures for a 5-μm-thick homeotropically aligned sample of the studied mixture. The optic axis is normal to the image plane, and the sample is placed between crossed polarizers. (a) Separate regions of N and N_{TB} phases observed at the transition between the two; the boundary is marked by the dashed line. Both regions are uniform and dark, indicating high-quality homeotropic alignment of the director n in the nematic and pitch axis t in the N_{TB} phase. (b) Under an applied ac voltage (5 V @ 10 KHz), a second-order Freedericsz transition

(reorientation of n in the center of the sample) is observed in the nematic region, while the N_{TB} region is unchanged. (c) Under higher voltage (7 V @ 10 KHz), the N_{TB} region undergoes a first-order reorientation of t in the form of nucleating toroidal focal conic domains (FCDs) and expanding stripes of splay and saddle-splay deformations of t. (d) Several seconds after the voltage has been switched off, the nematic region relaxes back to the homeotropic state, whereas the N_{TB} region relaxes considerably slower. 57

Figure 3-3: Light scattering geometry G1. 59

Figure 3-4: Light scattering geometry G2 61

Figure 3-5: Top panel: Normalized time correlation DLS correlation functions of the scattered light intensity taken in the nematic phase of the studied 70/30 mixture for geometry G1 with ($T - TTB = +6$ ℃) and scattering angle $\theta = 60$ ∘. Bottom panel: Normalized correlation data taken in the N_{TB} phase for geometry G1 with ($T - TTB = -1.1$ ℃) and $\theta = 60$ ∘. 63

Figure 3-6**:** Dependence of the relaxation rate $\Gamma 1n$ of the director mode detected in geometry G1 on the square magnitude of the scattering vector $q \perp 2$. Top panel: Nematic phase with $T - TTB = +6$℃. Bottom panel: Twist bend nematic phase with $T - TTB = -1.1$℃. 64

Figure 3-7: Top panel: Normalized time correlation functions of the scattered light intensity taken in the nematic phase of the 70/30 mixture for (a) geometry G2 with **(**$T - TTB = 16.2$℃) and angles $\theta i = 15°$, $\theta = 40°$(b) G2 with $T - TTB =$

16.2℃ and $\theta i = 15°$, $\theta = 0°$ (“dark” director geometry). Solid lines represent fits to double exponential decay, in (b), the slower component stretched. Bottom panel: Normalized correlation data taken in the N_{TB} phase for (a) geometry G2 with $T - TTB = -0.93℃$ and $\theta i = 15°$, $\theta = 40°$, (b) G2 with $T - TTB = -2.5℃$ and $\theta i = 35°$, $\theta = 0°$ (dark director geometry). Solid lines are single exponential fits, for (a) and double exponential in (b). 66

Figure 3-8: Dependence of the relaxation rates of the fluctuation modes detected in geometry G2 on scattering wavenumber $q \perp$. Circles and squares correspond to relaxation rates $\Gamma 2n$and $\Gamma 2p$ of the hydrodynamic director and nonhydrodynamic polarization modes detected in scattering geometry G2 in the middle of the nematic phase $T - TTB = 25℃$. The scattering angle θ ranges from −5° to 45° for fixed incident angle $\theta i = 15°$. The slope of the line through the data on the log-log plot for $\Gamma 2n$ is 2, indicating $\Gamma 2n \propto q2$. Diamonds and triangles correspond to relaxation rate $\Gamma 2t$ of the nonhydrodynamic pitch axis fluctuations at temperatures ($T - TTB = -0.85℃$ and $-8℃$) respectively, in the N_{TB} phase. These data are limited to higher q (or θ in the range 25° or 35° to 65°) due to a large component of background scattering at lower q, whose effect is exacerbated because of the low scattering intensity from fluctuations in the N_{TB} phase in the G2 geometry. 68

Figure 3-9 : Temperature dependency of correlation function of the scattered light intensity ($\boldsymbol{\Gamma 2t}$) taken in the twist-bend phase of the 70/30 mixture for geometry G2 with $\boldsymbol{\theta i = 15°}$, $\boldsymbol{\theta = 40°}$. 69

Figure 3-10 Temperature dependence of relaxation rates associated with director fluctuations detected in scattering geometry G2 in the uniaxial nematic phase ($\Gamma 2n$ for $T > T_{TB}$, circles in main figure and inset) and twist-bend phase ($\Gamma 2t$ for $T < T_{TB}$, squares in main figure) with fixed $\theta i = 15°$ and $\theta = 40°$. The solid line is a fit of $\Gamma 2t$ to the linear temperature dependence predicted by the theoretical model discussed in sec. 3.5.4. 70

Figure 3-11: Temperature dependence of the relaxation rate of polarization fluctuations in the nematic (diamonds in main figure and inset for $\theta i = 15°$ and $\theta = 40°$) and N_{TB} (triangles in main figure for $\theta i = 35°$, $\theta = 0°$) phases. The solid lines in both panels are fits of $\Gamma 2p$ to calculated results from the theoretical model presented in sec.3.5.4. 71

Figure 3-12: Temperature dependence of the inverse of the total scattering intensity ($\mathbf{I2-1}$)recorded in geometry G2 for $\boldsymbol{\theta i = 15°}$ and $\boldsymbol{\theta = 40°}$. The solid line is a linear fit of the data for $T < T_{TB}$ discussed further in sec. 3.5.4. The inset is a blow up of data in the nematic phase. 73

Figure 3-13: Left diagram: Schematic representation of the N_{TB} phase structure, showing heliconical director n (with cone angle β and helical pitch $t0$) and helical polarization field P. Right diagram: Frame of reference used to describe spatial variations of the average director or pitch axis, t, on length scales much longer than the pitch. The orthogonal unit vectors $e1$and $e1$ form a right-handed system with t. The xyz axes are fixed in the laboratory frame. 77

Figure 3-14: Visualization of certain fluctuation modes in the N_{TB} phase. Small cylinders represent the heliconical director field $n(r)$, and surfaces represent the pseudolayers with layer normal N. (a) Ground state. (b) Hydrodynamic mode with wave vector $q = 0$, with uniform rotation of $n(r)$ and hence uniform displacement of pseudo-layers; this mode has no energy cost with respect to the ground state. (c) Nonhydrodynamic tilt mode, with the coarse-grained director t [average of $n(r)$] tilted with respect to pseudolayer normal. (d) Hydrodynamic mode with $q = qz$, with z-dependent rotation of $n(r)$ and z-dependent displacement of pseudo-layers (leading to compression and dilation). (e) Hydrodynamic mode with $q = qx$, with x-dependent rotation of $n(r)$ and x-dependent displacement of pseudo-layers (leading to curvature), accompanied by tilt so that t remains normal to pseudo-layers.(with permission from Prof. J. V. Selinger) 87

Figure 4-1: Schematic views of the heliconical molecular organization in the nematic twist bend (N_{TB}) phase. The dark arrows represent the orientation of the local molecular long axis (or heliconical director n), which is nonpolar. Red arrows indicate a helically modulated polar vector (p), which represents a shape or electric polarization arising from the bent conformation of a dimer that contains an odd-numbered CH_2 linkage between the two aromatic core groups. The indicated planes, separated by one pitch length (t0), define a slab-like ‘‘pseudo-layer’’ that are associated with the heliconical structure. 97

Figure 4-2: Simulation of the pseudo-layer bending/compression mode in the N_{TB} phase, when q ⊥ and qz are both nonzero. The dark arrows represent the pseudo-layer normal (and average director t) with permission from Prof. J.V. Selinger, Kent State University. 98

Figure 4-3: Light scattering geometry for the study of the pseudo-layer bending/compression mode in the N_{TB} phase, with the ‘‘rocking’’ angle χ indicated. The normally incident laser light (wavevector ki, incident angle θi) is polarized vertical to the scattering plane (and parallel to the average director $t0$ when $\chi = 0°$). Horizontally-polarized scattered light (wavevector ks is collected at angle θ). The fluctuation wavevector probed is $q = ks - ki$. 101

Figure 4-4: Top: Typical light scattering correlation functions obtained in the N_{TB} phase at $\mathbf{T - TTB = -2.6}$℃ and for normal incidence, scattering angle $\boldsymbol{\theta = 40°}$, and rocking angles $\boldsymbol{\chi = 0°}$ (right plot) or $\mathbf{30°}$ (left plot). Solid lines are fits to a slightly stretched single exponential decay. Bottom: Textures of the N_{TB} phase recorded by polarizing microscopy at $\mathbf{T - TTB = -0.6}$℃ and for angle $\boldsymbol{\chi = 0°}$ (left) and $\mathbf{16°}$ (right). The position of the scattering volume is also recorded, allowing us to confirm no translation of the illuminated volume when the sample is rocked. The weak stripe texture visible for $\boldsymbol{\chi = 0°}$ is probably due to pseudo-layer shrinkage at the cell surfaces; it caused no significant static scattering. (Yellow double arrows indicate the orientattions of polarizer and analyzer placed in the optical path on either side of the sample.)..... 103

Figure 4-5: Dependence of the relaxation rate in the nematic phase on the rocking angle χ for a temperature $T - TTB = 1.9$ ℃. The dashed line represents the average value. 105

Figure 4-6: Dependence of the relaxation rate $\Gamma 1\mathrm{t}$ of the pseudo-layer undulation mode on the rocking angle χ for two temperatures, $\mathrm{T} - \mathrm{TTB} = -1.4$ ℃ (green diamonds) and -2.6 ℃ (blue circles), in the N_{TB} phase of studying sample, and for scattering angle $\theta = \theta m = 40°$. For χ between 0 and 30°, qz spans from 0 to 3.9×106 m $-$ 1, while q $\perp$ ranges from. 7.6×106 to 6.5×106 m $- 1$. The solid lines are fits described in the text. 106

Figure 4-7: Relaxation rate $\Gamma 1n$ versus $\sin 2\theta$ for rocking angle $\chi = 30°$ in the N phase ($T - TTB = 4.5$ ℃). Over the range of the data points, qz varies from 0.48×106 to $3.6 \times 106\ m - 1$ and $q \perp$ from 1.2×106 to $6.3 \times 106\ m - 1$.The solid line is a linear fit as described in the text. 108

Figure 4-8: Relaxation rate $\Gamma 1t$ versus $\sin 2\theta$ for rocking angle $\chi = 30°$ in the N_{TB} phase ($T - TTB = -2.5$ ℃). Over the range of the data points, qz varies from 0.48×106 to $3.6 \times 106\ m - 1$ and $q \perp$ from 1.2×106 to $6.3 \times 106\ m - 1$.The solid line is a fit to Eq. (4.4) 109

Figure 4-9: Temperature dependence of the inverse scattered intensity $\mathrm{I1t} - 1$ from the 70/30 mixture for scattering angle $\theta = \theta\mathrm{m} = 40°$ and rocking angle $\chi = 30°$. The solid line in the top panel is a fit of the data to the *T* dependence predicted by

Eq.(4.8) combined with Eqs.(4.6) and (4.7). In the bottom panel, the solid line is a fit of the data to the combination of Eqs.(4.8), (4.5)and (4.6)..... 112

Figure 4-10: The quantity $I1tT-1-I1tTTB-1x$ calculated from the data in the N_{TB} phase, as a function of $T-TTB$ and a fit to a straight line.(a) $x=1$ (b) $x=23$ (c) $x=13$ (d) $x=12$..... 115

Figure 5-1: Molecular structures of (a) MCT5 monomer, **I** 116.5℃ **N** 34℃ **Cr**, (b) DTC5C9 dimer, **I** 162℃ **N** 124℃ **N_{TB}** 85℃ **(SmX)** 77℃ **Cr**, (c) DTC5-C9-DTC-C9-DTC5 trimer, **I** 192℃ **N** 145℃ **N_{TB}**, (d) DTC5-C9-DTC-C9-DTC-C9-DTC5 tetramer, **I** 205℃ **N** 168℃ **N_{TB}**. 120

Figure 5-2: POM Polarizing optical microscopy textures of Nematic and N_{TB} phase respectively, the (a,d) dimer, (b,e) trimer and (c,f) tetramer under cross polarizers. The stripes in panels (d,e,f) are characteristic of the twist-bend nematic phase. 121

Figure 5-3: Light scattering geometries utilized. Subscripts 1 (3) denote conditions for collection of pure splay (bend) scattering, where the equilibrium director is oriented perpendicular (parallel) to the scattering plane, and scattering angle set to the "magic" angle (see text) for normal incidence. Almost pure twist scattering (subscript 2) is selected when the equilibrium director lies in the scattering plane and the laboratory scattering angle is set to the smallest feasible value (2˚ in our case). In all three cases, the incident and scattered light polarizations (displayed by double-ended arrows) are normal and parallel to the scattering plane, respectively. 123

Figure 5-4: Reduced temperature dependences of the nematic elastic constants. (a) – (c): Splay ($K11$), twist ($K22$), and bend ($K33$) constants for the dimer, trimer, and tetramer; (d): The ratio $K11K22$ with the theoretical threshold value for a N_{TB} phase indicated by a horizontal dashed line. 129

Figure 5-5: Reduced temperature dependences of the nematic orientational viscosities in the studied n-mers. (a) – (c): $\eta splay$, $\eta twist-bend$, $\eta bend$; (d): The ratio $\eta twist-bend\ \eta splay$..... 131

Figure 5-6: Elastic constants (a) and viscosities (b) as a function of reduced temperature in the N phase of the monomer MCT5. T_{NCr} is the temperature of the nematic to crystal transition. 132

Figure 5-7: Splay (K11, top panel) and twist (K22, bottom panel) elastic constants plotted as a function of temperature relative to the nematic-isotropic transition for the studied n-mers..... 134

DEDICATION

To my Father and Mother, Morteza and Fatemeh who were the first teachers in my life.

ACKNOWLEDGEMENTS

Here I have an opportunity to acknowledge the people who helped and supported me during my graduate life in Kent State University.

I would like to express my special appreciation and thanks to my advisor, Prof. Samuel N. Sprunt. I would like to thank you for the support, encourage and mentoring my research. Your advice on both research as well as on my career have been invaluable. During my research in Kent State University, I always had the chance to discuss and publish under his supervision and had opportunity of attending various conferences inside and outside of USA.

Prof. James T. Gleeson and Prof. Antal Jakli as my co-advisors always had great contribution in my research, I would like to thank them for their constructive suggestions and discussions.

A very special gratitude goes to Prof. Jonathan Selinger and Prof. Oleg lavrentovich for their collaboration and great teamwork. The theoretical work of twist-bend nematic was developed by Dr. Selinger and his team. Prof. Lavrentovich shared his lab and facilities fruitfully with us and always had discussions and ideas for developing my research. They had great impact in success of my research and I really appreciate their helpful collaboration.

I would like to thank Dr. Alan Baldwin who always helped me to figure out the software and hardware issues with experimental set-up in our lab.

All the love and respects go to Prof. Robin Selinger for her thoughts, helps and unconditional support. I do appreciate her.

Next, I would like to thank all Physics faculties and staffs who thought me all physics courses and guided me toward my degree. Being in Physics department was an honor for me and I deeply appreciate every single support for me in this journey.

I had great friends and collaboration: Pavan Kumar, Shokir Pardaev, Greta Babakhanova, Volodymyr Borshch, Shaikh Shamid, Mojtaba Rajabi, Salma Begum, Pritam Mandal, Mona Mirheidari, Ahlam Nemati, Sasan Shadpour, Rony Saha, Prabesh Gyawali, Parastoo Maleki.. I would like to thank their collaboration and support in my PhD life.

All my heart and soul would appreciate my parents Morteza and Fatemeh and my siblings Monireh and Amin, you are my inspiration in the life. I appreciate your encourage, patience and support the whole my life.

I finally thank the love of my life, Dr. Mohammad Nopoush, for not only being a great support, but also for helping and teaching me Physics. I am grateful to have you in my life.

My Little daughter Ayleen, mom loves you and thanks for being with me during my experiments and all hard days of getting PhD.

Zeinab Parsouzi

June 2019, Kent, Ohio

CHAPTER 1

INTRODUCTION

1.1 INTRODUCTION TO LIQUID CRYSTALS

Liquid crystals (LCs) are phases of condensed matter that exhibit a degree of ordering intermediate between conventional solid and liquid states[1]. For this reason, they are often referred to as “mesophases” (“meso” = middle). Due to their responsiveness to applied mechanical, electric, and optical fields, liquid crystals are the basis of various electro-optical device, display, and sensor technologies that have grown explosively in recent decades and are now ubiquitous in our everyday lives [2].

Liquid crystals may be broadly classified in two groups. In thermotropic LCs, the molecular constituents are small organic molecules consisting of a rigid core structure to which one or more flexible hydrocarbon chains are attached. Transitions between mesophases are primarily driven by changing temperature. The second group, lyotropic LCs, is formed by dispersions of amphiphilic or surfactant molecules in a suitable solvent; their phase transitions are driven primarily by changes in composition or the concentration

of components. Lyotropics are significant for their role in biological systems (e.g., cell membranes)[3]. In this dissertation we will focus exclusively on thermotropic LCs.

1.2 CLASSIFICATION ACCORDING TO MOLECULAR ORDER

Both thermotropic and lyotropic mesophases may be further classified according to their molecular ordering and symmetry.

In the **nematic** mesophase, one or more axes of the anisotropic molecules (mesogens) spontaneously align along distinct directions in space [1]**.** However, the positional correlations between molecules are short-ranged – i.e., the molecular centers of mass are essentially randomly positioned in space, as in a simple liquid. Thus, nematic phases are orientationally ordered, but positionally disordered.

Elementary **smectic** phases, in addition to nematic orientational order, exhibit positional order in one dimension. The molecules are arranged in two-dimensional layers, which are stacked along the third dimension. In some smectics within each layer, the molecular positions are random; thus, the individual layers are liquid-like.

Columnar phases possess orientational order along one spatial direction and are positionally ordered in two other, orthogonal directions (i.e., in the plane perpendicular to the axis of orientational order). The individual molecules forming the columnar phase are typically disk shaped, and stack in columns, which pack in a two-dimensional rectangular or hexagonal lattice in the plane perpendicular to the column axis [4]. There is no positional order parallel to this axis; the columns can freely slide parallel to one another.

1.3 NEMATIC PHASE

The nematic phase (N) is typically formed by achiral elongated, rod-like organic molecules. A classic example is shown in Figure 1-1. Achiral means the molecule (averaged over its conformational degrees of freedom) cannot be distinguished from its mirror image[4].

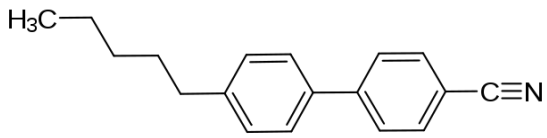

Figure 1-1: Molecular structure of 4-cyano-4´-pentylbiphenyl (5CB).

The nematic phase may subdivided into several distinct classes: achiral uniaxial, cholesteric (chiral nematic), biaxial, and, most recently, orientationally modulated nematics known as splay-bend and twist-bend phases[5].

1.3.1 UNIAXIAL AND BIAXIAL NEMATIC

In the uniaxial nematic phase, the liquid crystal molecules (or mesogens) align along a single direction in space called the director, which is described by a unit vector $\hat{n}$**.** For rod-shaped thermotropic LCs, $\hat{n}$ corresponds to the average direction of the molecular long axis. Physical properties of the uniaxial nematic are invariant under inversion of $\hat{n}$**;** thus, the exchange of $\hat{n}$ with $-\hat{n}$ is a symmetry operation. A schematic representation of the uniaxial nematic phase is shown in Figure 1-2(a).

A biaxial nematic phase, with two orthogonal axes of orientational order described by directors $\hat{n}$, $\hat{m}$ with $\hat{n} \perp \hat{m}$, was first demonstrated in lyotropic LCs[6]. The existence of a biaxial thermotropic nematic phase remains controversial after claims of its discovery in bent-shaped molecules were published in the early 2000s[7]. The biaxial nematic phase is illustrated in Figure 1-2 (b) for plank-like molecules[8].

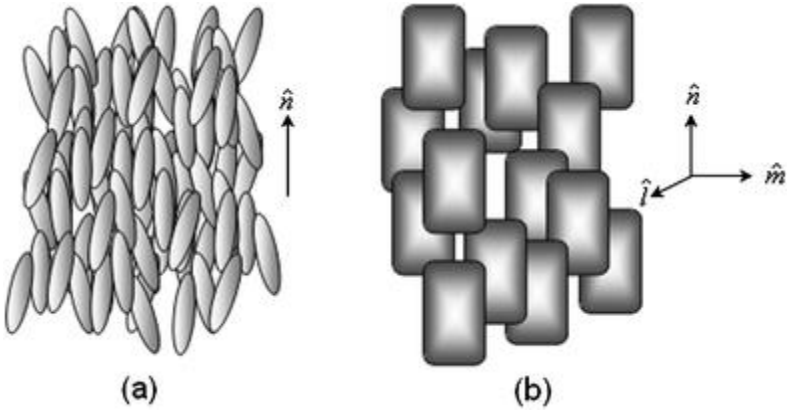

Figure 1-2: (a) uniaxial nematic; (b) biaxial nematic(from: C. T. Imrie and P. A. Henderson, "Liquid crystal dimers and higher oligomers: Between monomers and polymers," *Chem. Soc. Rev.*, vol. 36, no. 12, pp. 2096–2124, 2007) [9].

In a uniaxial nematic phase, spatial variations (or gradients) in the director $\hat{n}$ that contribute to the orientational elastic energy of the nematic may be classified as "splay", "twist", or "bend" deformations of the field $\hat{n}(r)$. These deformations are depicted in Figure 1-3.

Figure 1-3: Splay, twist, and bend of uniaxial nematic directors (image by N.J. Mottram, University of Strathclyde, 2010, https://www.slideshare.net/nigelmottram/nonlocal-effects-in-models-of-liquid-crystal-materials).

The orientational elastic energy density of a uniaxial nematic may be constructed from these three types of deformation as[1].

$$F_N = \int d\vec{r}\ f_N(\vec{r}) = \int d\vec{r}\,[\frac{K_{11}}{2}\left(\vec{\nabla}.\hat{n}\right)^2 + \frac{K_{22}}{2}\left(\hat{n}.\vec{\nabla}\times\hat{n}\right)^2 + \frac{K_{33}}{2}\left(\hat{n}\times\vec{\nabla}\times\hat{n}\right)^2\,] \quad (1.1)$$

where K_{11}, K_{22}, and K_{33} are orientational elastic constants corresponding to splay, twist, and bend deformations, respectively. They have SI units of Newton (N).

1.3.2 CHIRAL NEMATIC (CHOLESTERIC)

Elongated, chiral molecules can form a chiral nematic phase (N^* phase), also called the cholesteric phase. Molecular chirality arises when the mirror image of a molecule (after averaging over internal degrees of freedom) cannot be superimposed on the original (Our hands are simple examples of chiral objects.) In the cholesteric phase, rod-like molecules twist in space about a short axis of the molecules, forming a right- or left-handed helical structure along this axis (Figure 1-4). The spatial period of the helical rotation is called the

pitch (p_0), and is typically of order 1-100 micron (10^{-6}m)[1][3]. In any plane perpendicular to the helical axis, the long axis of the molecules is uniformly oriented. Thus, if $\hat{z}$ is taken as the helical axis, the average long molecular axis may be described by a helical director field,

$$F_N = \int d\vec{r}\ f_N(\vec{r}) = \int d\vec{r}\,[\frac{K_{11}}{2}\left(\vec{\nabla}.\hat{n}\right)^2 + \frac{K_{22}}{2}\left(\hat{n}.\vec{\nabla}\times\hat{n} - q_0\right)^2 + \frac{K_{33}}{2}\left(\hat{n}\times\vec{\nabla}\times\hat{n}\right)^2\,] \quad (1.2)$$

Where $q_0 = \pm 2\pi/p$. The helical structure is purely an orientational "wave"; there is no positional ordering of the molecular centers of mass in any dimension.

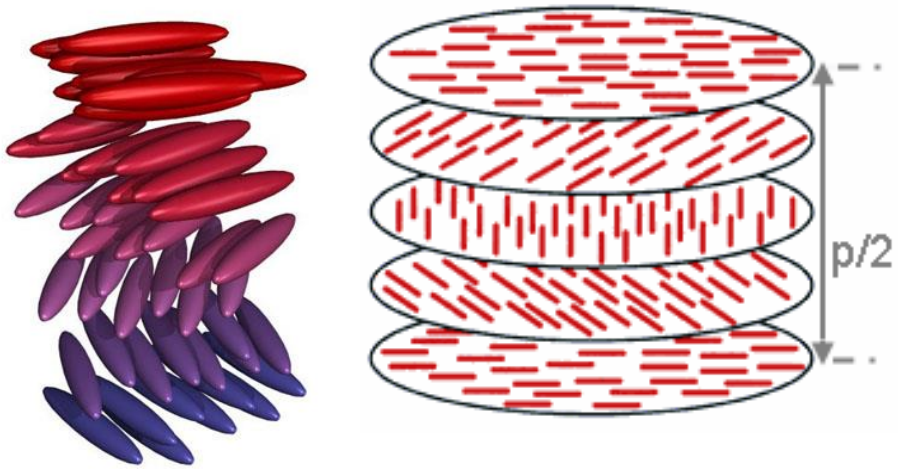

Figure 1-4: Twisting of the cholesteric phase, p is the pitch(Source: http://barrett group.mcgill.ca/tutorials/liquid_crystal/LC03.htm)[10].

1.3.3 TWIST-BEND NEMATIC PHASE

We have mentioned earlier the possibility of two other nematic phases in which the molecular orientation is modulated in space instead of being uniform – namely, the so-called splay-bend and twist-bend nematic phases. In these phases, the modulation is "programmed" in by the close packing of molecules with a preference for conformational bend. Since it is not possible to fill space homogeneously with a uniform bend in the director field $\hat{n}$, the molecules must additionally either splay or twist in a periodic fashion [11]to maintain a constant mass density.

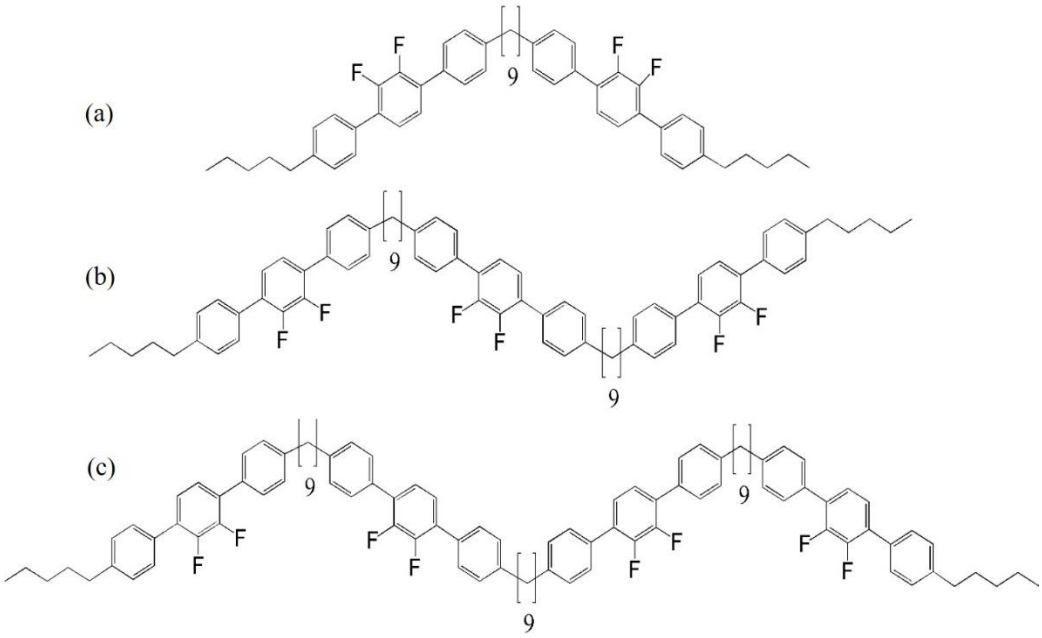

Figure 1-5: (a) DTC5C9 dimer, I 162°C N 124°C N_{TB} 85°C (SmX) 77°C Cr, (b) DTC5-C9-DTC-C9-DTC5 trimer, I 192°C N 145°C N_{TB}, (c) DTC5-C9-DTC-C9-DTC-C9-DTC5 tetramer, I 205°C N 168°C N_{TB}.

So far, only the combination of bend and twist – the twist-bend nematic (N_{TB}) phase – has been positively identified[5][12]–[20], initially in systems of achiral dimeric molecules. Liquid crystal dimers are composed of two relatively rigid organic core units connected by a flexible hydrocarbon (CH_2) linkage. When this linkage contains an odd number of carbon atoms, an overall conformational bend is favored – a prototypical example is shown in Figure 1-5: (a)– and this promotes the twist-bend modulation. Subsequently, tell-tale indications of the N_{TB} phase have also been observed in higher n-mers (e.g., trimers and tetramers)[21]–[24], where three or more rigid core units are linked by odd-membered hydrocarbon chains Figure 1-5: (b),(c).

The N_{TB} phase is observed for temperatures below the usual uniaxial nematic (N) phase. It was first predicted by Meyer[24] and later elaborated on theoretically by Dozov [11], Shamid and Selinger [25], and studied via molecular simulations by Kleman [26] and by Memmer [27].

The orientationally-modulated structure of the N_{TB} phase is depicted in Figure 1-6. For convenience of illustration, the LC n-mers are replaced by cylinders. The cylinder axis represents the average long axis of an n-mer. This axis traces out a heliconical structure [4][13], which is described by a local director field of the form:

$$\hat{n} = \hat{z}\cos\beta + \hat{x}\sin\beta\cos(q_0 z) + \hat{y}\sin\beta\sin(q_0 z) \tag{1.3}$$

Here β is the cone angle (tilt of $\hat{n}$ away from the helical modulation axis $\hat{z}$), and $q_0 = 2\pi/p_0$ is the wavenumber of the modulation. The limit $\beta = 0$ represents a uniaxial nematic with $\hat{n} = \hat{z}$, while $\beta = \pi/2$ corresponds to the cholesteric phase with pitch

$2\pi/q_0$. Models describing different mechanisms for a phase transition from the uniaxial N phase to the N_{TB} phase, which will be of interest for analyzing the experimental results presented in this dissertation, will be discussed in later chapters.

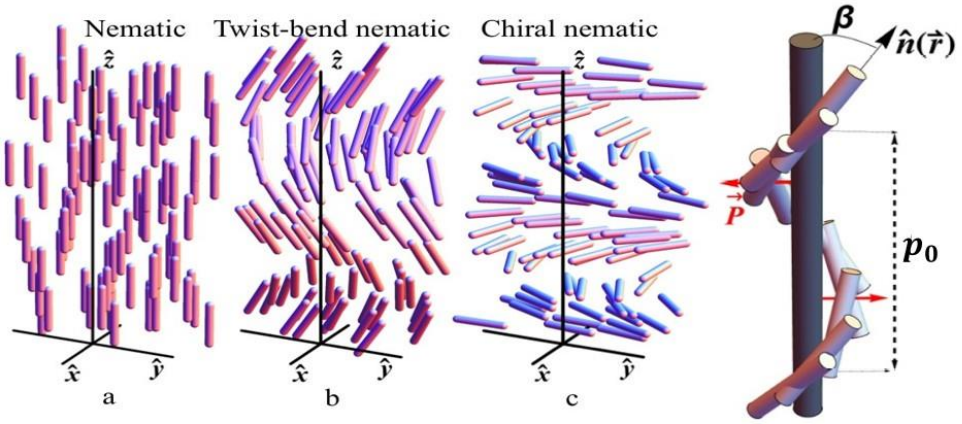

Figure 1-6: Schematics of director arrangement in (a) N phase (b) N_{TB} phase (c) Cholesteric N^* Phase (image by: V. Borshch *et al.*, 2013) [13]. (d) Showing heliconical director $\hat{n}$ in N_{TB} phase with cone angle β, helical pitch p_0 and helical polarization field $\vec{P}$.

The N_{TB} phase possesses certain unusual properties. It has a spontaneous chiral structure [28,29], even though in most cases the molecules are achiral. Domains of right- and left-handed heliconical arrangement of the molecules coexist. The pitch of the helicoid is remarkably short – of order 10 nm (a few molecular lengths), roughly 100 times smaller than a typical cholesteric pitch. The optical texture of the N_{TB} phase shows focal-conic (Figure 1-7) and striped textures[12][17][26][30]–[32] that resemble textures in smectic liquid crystals caused by defects in the smectic layer orientation [33]. In the N_{TB} phase there is no mass density wave and thus no "true" layering of molecules. The smectic-like

defect textures have been ascribed to distortions of “pseudo-layers”, defined by slabs of the heliconical structure with a thickness equal to one pitch.

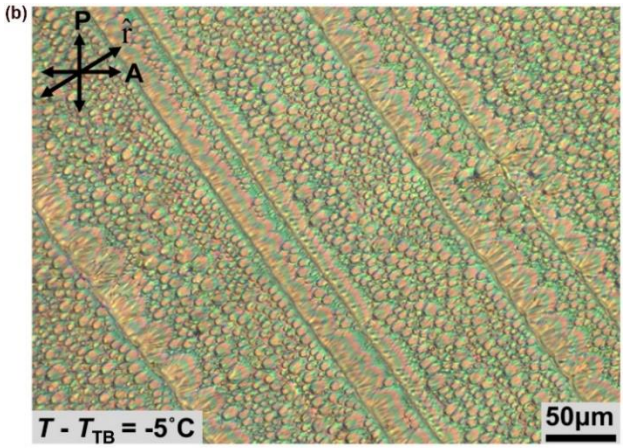

Figure 1-7: POM textures of CB7CB under cross polarizers showing uniformly aligned, N_{TB} phases with focal conic domains. The direction of rubbing is shown by the axis $\hat{\mathbf{r}}$ (source: G. Babakhanova *et al.*, 2017**)** [34].

Results from freeze fracture transmission electron microscopy (FFTEM)[5][13] [14][35], such as those shown in Figure 1-8 confirm the pseudo-layered N_{TB} structure, with “layer” spacing of order ~10 nm [13][17][28][33][35].

Finally, although the N_{TB} phase shows no evidence of a macroscopic polarization, a flexoelectric effect [36] associated with spontaneous bending of $\hat{n}$ and the recent observation of an electroclinic effect [15] in the N_{TB} phase suggest that a short-pitch helical polarization field is tied to the heliconical director structure. In fact, a recent theory [25] describing the transition between uniaxial and twist-bend nematic phases invokes such a polarization field as the primary order parameter.

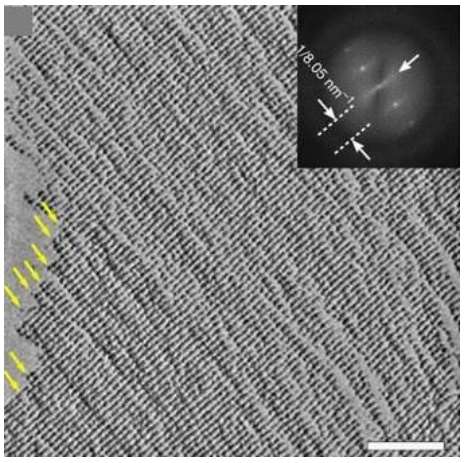

Figure 1-8: FFTEM textures and corresponding Fast Fourier transform (FFT) patterns of CB7CB in N_{TB} phase with uniform structure. The pitch is 8.05 nm viewed in the planes parallel to the optic axis. The arrows in figure point towards domain boundaries of average extension 26 nm, which are roughly perpendicular to the N_{TB} layers. Presence of domains is also revealed by a diffuse intensity pattern in FFT, marked by a white arrow(image by: by: V. Borshch *et al.*, 2013) [13].

1.4 ELEMENTARY SMECTIC PHASES

We consider the smectic-A and C phases of simple rod-like LC molecules.

1.4.1 SMECTIC A:

The molecules in a smectic A (SmA) phase are parallel to each other and arranged in layers with their long axes are normal to the layer plane, Figure 1-9 left. In each layer, the centers of mass of molecules are positionally disordered as in a fluid; thus when the layers are stacked, there is translational order only in the direction along the layer normal (one dimensional mass density wave). Optically the SmA is uniaxial because of its continuous rotational symmetry about the layer normal [1][3].

1.4.2 SMECTIC C:

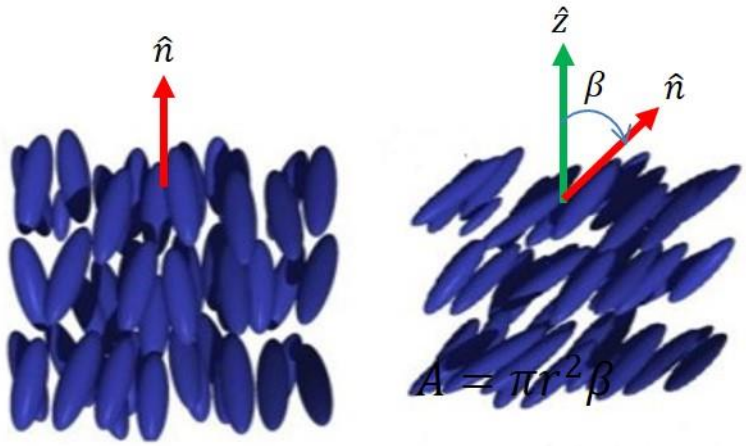

Figure 1-9: Schematic representation of smectic liquid crystal phases, left: smectic A; right: smectic C [37].

Like the SmA phase, the molecules in the smectic C (SmC) phase are layerd along one dimension, but their average long axis is tilted away from layer normal, Figure 1-9 right. The tilt is confirmed by x-ray scattering, which shows that the diffuse peaks arising from short-range side-to-side correlations between molecules lie along an axis in q-space that makes an acute angle with respect to the axis of the Bragg peaks that are produced by the 1D layer structure. (In a SmA phase, the angle would be 0˚.) The SmC is optically biaxial due to the broken continuous symmetry about the layer normal: The index of refraction for polarized light propagating perpendicular to the average molecular long axis and parallel to the tilt plane is no longer equivalent to the index for light propagating perpendicular to both the long axis and the tilt plane.

1.5 DYNAMIC LIGHT SCATTERING

Dynamic light scattering (DLS) is a powerful technique for studying liquid crystal properties – notably, viscoelastic parameters such as orientational elastic constants and viscosities – as well as fundamental aspects of LC ordering and ordering transitions through the characteristics of collective molecular fluctuation modes. In the scattering process, large numbers of molecules are involved so a continuum approach – e.g., continuum elasticity theory and hydrodynamics – are used to describe and analyze the fluctuation modes that contribute to the scattering [38].

1.6 HYDRODYNAMIC MODES:

After a small disturbance from thermal equilibrium of a system with many degrees of freedom, almost every degree of freedom will relax to its equilibrium value in times determined by microscopic interactions in the system. However, there are some collective motions which decay more slowly, and have frequencies and/or relaxation rates proportional to some power of their wavenumber (inverse wavelength). These "long-lived" degrees of freedom or hydrodynamic modes, which have an important role in light scattering, arise from conservation laws or continuous broken symmetries [39].

As a simple example, in conventional fluids, five hydrodynamic equations describe the conservation of mass, momentum and energy. Density, temperature and three components of momentum are the "slow" variables that appear in these equations. The solutions of these equations of motion represent two propagating modes (longitudinal sound waves) and three diffusive modes (two transverse shear waves and one mode

associated with temperature or entropy fluctuations). Typical frequencies for these modes are in the range of megahertz to gigahertz, and optical interferometric techniques, which detect shifts in the frequency of the incident light and broadening of the linewidth, are used to probe them.

Goldstone first demonstrated theoretically that spontaneous symmetry breaking is another source of "slow" hydrodynamic modes [40]. Consider a liquid crystal in the isotropic phase. There is continuous translational symmetry in all three spatial dimensions and also continuous rotational symmetry about any axis. During the phase transition from isotropic to uniaxial nematic, continuous symmetry breaks for rotations around two independent axes perpendicular to the director $\hat{n}$. (The symmetry around these two axes is reduced from continuous to discrete, two-fold rotations.) Goldstone's theorem then implies two "broken symmetry" fluctuation modes – independent fluctuations in the orientation of $\hat{n}$ ("director modes") – that tend to restore continuous rotational symmetry. Adding these two director modes to the five normal fluid hydrodynamic modes (from conservation laws) results in seven hydrodynamic modes that characterize a uniaxial nematic [39][41].

In smectic A and C phases, in addition to the broken rotational symmetry of the nematic, continuous translational symmetry is reduced to a discrete symmetry in one dimension (i.e., along the layering direction). This introduces an additional hydrodynamic variable – the layer displacement u – that acts to restore the full translational symmetry.

1.7 DYNAMIC LIGHT SCATTERING FROM LIQUID CRYSTALS

Light incident on a slab of liquid crystal material is scattered due to spatio-temporal inhomogeneities in the material's dielectric properties. For example, in the case of a nematic LC, the two thermal fluctuation modes of the director mentioned in the previous section scatter light copiously [38]. De Gennes first calculated the dependence of this scattering on light polarization, material elastic constants, anisotropic dielectric constants, and the wavevector of the fluctuations [42]. In the case of a smectic A, the strongest light scattering comes from undulatory motions of the smectic layers, which cause the director to "splay out" as it follows the curvature of the deformed layer. In a smectic C, the tilted director can rotate around the layer normal without any motion of the layer planes, resulting in substantial light scattering. Generally, the director modes couple more strongly to light than the other hydrodynamic modes (such as density or temperature fluctuations), because they directly modulate the large dielectric anisotropy of the LC and because they cost less energy than the other modes.

1.8 SCOPE AND OBJECTIVE OF THIS DISSERTATION

This dissertation presents a DLS study of director fluctuation modes in the N_{TB} phase and at the uniaxial nematic to N_{TB} phase transition in certain liquid crystal dimers, trimers, and tetramers (n-mers, with n = 2,3,4). These materials consist of two, three or four common mesogenic core units connected by odd-membered methylene (CH_2) spacers. Our primary objectives are: (1) To measure viscoelastic parameters (orientational elastic constants and viscosities) in the nematic phase above the N – N_{TB} transition and to

determine the pretransitional behavior of these parameters, and (2) To characterize the broken symmetry modes in the N_{TB} phase and to compare their wavevector and temperature dependences to different theoretical models of the mechanisms that stabilize the N_{TB} structure.

The remainder of this dissertation is organized as follows:

Chapter 2: We review the theoretical background for light scattering from director fluctuations in a uniaxial nematic, and describe the scattering selection rules and experimental set-up employed in our studies.

Chapter 3: We present our experimental results on fluctuation modes in the N_{TB} phase of a dimer/monomer mixture, which shows a nearly continuous N–N_{TB} transition. We compare these results to the predictions of a model due to Shamid and Selinger [25], which postulates a helical polarization wave as the order parameter for the N_{TB} phase.

Chapter 4: We discuss an experimental light scattering geometry for measuring the elastic constant for compression of the "pseudo-layered" structure of the N_{TB} phase, and we report results for the temperature dependence of this parameter. These results allow us to make a comparison to predictions from two different theoretical models that describe the development of the N_{TB} phase.

Chapter 5: In this chapter, we extend our studies to higher n-mers – specifically, trimer and tetramer compounds, which are homologs of the dimer investigated in Chapters 3 and 4 – that exhibit the textures and other tell-tale indications of a pseudo-layered N_{TB} phase. We report measurements of the orientational elasticities and viscosities of the n = 2 – 4

homologous n-mers, focusing on their behavior near the N–N_{TB} transition. We show that this pretransitional behavior agrees qualitatively with a "coarse-grained" analysis of local models for the N_{TB} ordering process. This result confirms that on length scales large compared to the helicoidal pitch, the N – N_{TB} transition has the same symmetry as the nematic to smectic-A transition.

Chapter 6: We summarize our key findings, and suggest directions for future research.

1.9 REFRENCES:

[1] P.G.De Gennes and J.Prost, *The Physics of Liquid Crystals*. Oxford: Clarendon Press, 1993.

[2] "'Polymers and Liquid Crystals Virtual Lab,'" *Case Western Reserve University,*. .

[3] P. S. E.B.Priestly, P.J.Wojtowicz, *Introduction to Liquid Crystals*. New York and London: Plenum Press, 1976.

[4] M. Čopič, "Nematic phase of achiral dimers spontaneously bends and twists," *PNAS,* vol. 110, p. 15931, 2013.

[5] D. Chen, J. H. Porada, J. B. Hooper, A. Klittnick, Y. Shen, and M. R. Tuchband, "Chiral heliconical ground state of nanoscale pitch in a nematic liquid crystal of achiral molecular dimers," vol. 110, no. 40, 2013.

[6] L. J. Yu, A. Saupe, "Observation of a biaxial nematic phase in potassium laurate-1-decanol-water mixtures," *Phys. Rev. Lett.,* vol. 45, p. 1000–1003, 1980..

[7] G. R. Luckhurst, "Biaxial Nematic Liquid Crystals: Fact or Friction," *Thin Solid*

Films, pp. 393, 40–52, 2001.

[8] M. Lehmann and J. Seltmann, “Low temperature enantiotropic nematic phases from V-shaped, shape-persistent molecules,” *Beilstein J. Org. Chem.*, vol. 5, pp. 1–9, 2009.

[9] C. T. Imrie and P. A. Henderson, “Liquid crystal dimers and higher oligomers: Between monomers and polymers,” *Chem. Soc. Rev.*, vol. 36, no. 12, pp. 2096–2124, 2007.

[10] C. J. Barrett, "Barrett Research Group," McGill Chemistry, [Online]. Available: http://barrett-group.mcgill.ca/tutorials/liquid_crystal/LC03.htm.

[11] I. Dozov, “On the spontaneous symmetry breaking in the mesophases of achiral banana-shaped molecules,” *Europhys. Lett.*, vol. 56, no. 2, pp. 247–253, 2001.

[12] M. Cestari *et al.*, “Phase behavior and properties of the liquid-crystal dimer 1 , 7 - bis (4-cyanobiphenyl-4 -yl) heptane : A twist-bend nematic liquid crystal,” vol. 031704, pp. 1–20, 2011.

[13] V. Borshch, Y. K. Kim, J. Xiang, M. Gao, A. Jákli, V. P. Panov, J. K. Vij, C. T. Imrie, M. G. Tamba, G. H. Mehl and O. D. Lavrentovich, Nat. Commun., 2013, 4, 1–8..

[14] D. Chen, M. Nakata, R. Shao, M. R. Tuchband, M. Shuai, U. Baumeister, W. Weissflog, D. M. Walba, M. A. Glaser, J. E. Maclennan and N. A. Clark, Phys. Rev. E - Stat. Nonlinear, Soft Matter Phys., 2014, 89, 1–5.

[15] C. Meyer, G. R. Luckhurst, and I. Dozov, “Flexoelectrically Driven Electroclinic

Effect in the Twist-Bend Nematic Phase of Achiral Molecules with Bent Shapes," vol. 067801, no. August, pp. 1–5, 2013.

[16] E. Gorecka *et al.*, "Do the short helices exist in the nematic TB phase ?," *Liq. Cryst.*, vol. 42, no. 1, pp. 1–7, 2015.

[17] V. P. Panov *et al.*, "Spontaneous Periodic Deformations in Nonchiral Planar-Aligned Bimesogens with a Nematic-Nematic Transition and a Negative Elastic Constant," vol. 167801, no. OCTOBER, pp. 15–18, 2010.

[18] P. A. Henderson, C. T. Imrie, P. A. Henderson, C. T. I. Methylene-linked, P. A. Henderson, and C. T. Imrie, "Methylene-linked liquid crystal dimers and the twist-bend nematic phase Methylene-linked liquid crystal dimers and the twist-bend nematic phase," vol. 8292, 2011.

[19] K. Adlem *et al.*, "Chemically induced twist-bend nematic liquid crystals , liquid crystal dimers , and negative elastic constants," vol. 022503, pp. 1–8, 2013.

[20] V. Görtz, C. Southern, N. W. Roberts, H. F. Gleeson, and J. W. Goodby, "Unusual properties of a bent-core liquid-crystalline fluid," *Soft Matter*, vol. 5, no. 2, pp. 463–471, 2009.

[21] R. J. Mandle, "Soft Matter The dependency of twist-bend nematic liquid crystals on molecular structure : a progression from dimers to trimers , oligomers and polymers," *Soft Matter*, vol. 12, pp. 7883–7901, 2016.

[22] R. J. Mandle and J. W. Goodby, "RSC Advances Progression from nano to macro science in soft matter systems : dimers to trimers and oligomers in twist-bend liquid

crystals †," pp. 34885–34893, 2016.

[23] R. J. Mandle, M. P. Stevens, and J. W. Goodby, "Developments in liquid-crystalline dimers and oligomers," *Liq. Cryst.*, vol. 44, no. 12–13, pp. 2046–2059, 2017.

[24] F. P. Simpson, R. J. Mandle, J. N. Moore, and J. W. Goodby, "and macro-sciences in supermolecular," no. I, pp. 5102–5110, 2017.

[25] S. M. Shamid, S. Dhakal, and J. V Selinger, "Statistical mechanics of bend flexoelectricity and the twist-bend phase in bent-core liquid crystals," vol. 052503, no. May, pp. 1–11, 2013.

[26] M. Kleman, "PHYSICAL REVIEW E 98 , 032705 (2018) Defects in the twist-bend nematic phase : Stabilities and instabilities of focal conic domains and related topics," vol. 032705, pp. 1–8, 2018.

[27] R. Memmer, "Liquid crystal phases of achiral banana-shaped molecules : a computer simulation study Liquid crystal phases of achiral banana-shaped molecules : a computer simulation study †," vol. 8292, 2010.

[28] V. P. Panov *et al.*, "Microsecond linear optical response in the unusual nematic phase of achiral bimesogens," *Appl. Phys. Lett.*, vol. 99, no. 26, 2011.

[29] L. Beguin, J. W. Emsley, M. Lelli, A. Lesage, G. R. Luckhurst, B. A. Timimi and H. Zimmermann, J. Phys. Chem. B, 2012, 116, 7940–7951.

[30] P. A. Henderson and C. T. Imrie, "Methylene-linked liquid crystal dimers and the twist-bend nematic phase," *Liq. Cryst.*, vol. 38, no. 11–12, pp. 1407–1414, 2011.

[31] V. P. Panov, R. Balachandran, J. K. Vij, M. G. Tamba, A. Kohlmeier, and G. H.

Mehl, “Field-induced periodic chiral pattern in the Nx phase of achiral bimesogens,” *Appl. Phys. Lett.*, vol. 101, no. 23, pp. 1–5, 2012.

[32] S. M. Salili, C. Kim, S. Sprunt, J. T. Gleeson, O. Parri, and A. Jákli, “Flow properties of a twist-bend nematic liquid crystal,” *RSC Adv.*, vol. 4, no. 101, pp. 57419–57423, 2014.

[33] M. G. Friedel, “Les états mésomorphes de la matière (The mesomorphic states of matter),” *Ann. Phys.*, vol. 18, pp. 273–474, 1922.

[34] G. Babakhanova *et al.*, “Elastic and viscous properties of the nematic dimer CB7CB,” vol. 062704, pp. 1–12, 2017.

[35] R. R. R. De Almeida *et al.*, “Nanostructure and dielectric properties of a twist- bend nematic liquid crystal mixture,” *Liq. Cryst.*, vol. 41, no. 11, pp. 1661–1667, 2014.

[36] R. B. Meyer, “Piezoelectric Effects in Liquid Crystals,” *Phys. Rev. Lett.*, vol. 22, 1969.

[37] I. Dierking, “Chiral liquid crystals: Structures, phases, effects,” *Symmetry (Basel).*, vol. 6, no. 2, pp. 444–472, 2014.

[38] S. Kumar, *Liquid Crystals,Experimental Study of Physical Properties and Phase Transitions*. Cambridge: Cambridge University Press, 2011.

[39] P. C. Martin, O. Parodi, and P. S. Pershan, "Unified Hydrodynamic Theory for Crystals, Liquid Crystals, and Normal Fluids," *Phys. Rev. A* , vol. 6, no. 2401, 1972.

[40] J. Goldstone, “Field theories with « Superconductor » solutions,” *Nuovo Cim.*, vol. 19, no. 1, pp. 154–164, 1961.

[41] G. Brown, *Advances in Liquid Crystals*. New York: Academic Press, 1979.

[42] C. A. PG De Gennes, “Fluctuations d’orientation et diffusion Rayleigh dans un cristal nématique,” *Sci.*, vol. 266, no. 15, 1968.

CHAPTER 2

BASICS OF DYNAMIC LIGHT SCATTERING

In this chapter, the theoretical background and formulation of the light scattering experiment performed in this dissertation are presented. Details of scattering from director fluctuations in nematic liquid crystal, along with relevant optical selection rules to isolate director modes, are reviewed.

2.1 INTRODUCTION

Light scattering probes structure and dynamics of matter on length scales comparable to an optical wavelength. In classical electro-magnetic theory, light scattering is result of coupling of incoming light to inhomogeneities in the dielectric properties of the material. These can be due to intermolecular or intramolecular fluctuations, or static variations, of these properties. The intensity, spectral shift, or spectral broadening of the scattered light, analyzed as a function of the scattering vector $\vec{q} = \vec{k}_f - \vec{k}_i$ and light polarization, contains information about the number and nature of hydrodynamic modes of the system [1] Here $\vec{k}_i$, $\vec{k}_f$ are the wavevectors of the incident and scattered light.

As we discussed in section 1-6 (Chapter 1), hydrodynamic modes in liquid crystals originate from conservation laws for mass, energy and momentum or from broken symmetries[2] . In LCs, the scattered light from fluctuations of conserved quantities is ~10^6 times weaker than that from orientational (broken symmetry) fluctuations of the optical axis, or director. To study the director modes, Rayleigh scattering – or quasi-elastic scattering characterized by a negligible energy transfer (frequency shift) – is typically employed.

2.2 THEORY OF QUASI-ELASTIC LIGHT SCATTERING (QELS)

We review the theory of QELS based on classical electrodynamics [3]–[5]. Consider a plane wave with electric field of the form

$$\vec{E}_i(\vec{r},t) = \hat{\imath}E_0 \exp i\,(\vec{k}_i.\vec{r} - \omega_i t) \tag{2.1}$$

with amplitude E_0, wavevector $\vec{K}_i$, angular frequency ω_i and linear polarization $\hat{\imath}$, that impinges on a nonconducting, nonmagnetic, non-absorbing dielectric medium, Figure 2-1.

This electric field polarizes the molecules of the medium and the resulting oscillating dipoles emit electromagnetic radiation in all directions. The intensity of the scattered light in any given direction is a sum over the illuminated sample volume. If the dielectric constant (or tensor in the case of a LC) is spatially uniform, then this sum will simply produce transmitted light in the same direction as the incident light, with no scattering off this direction. In a uniaxially anisotropic medium (such as a nematic liquid

crystal) with average molecular alignment along a direction $\hat{n}_0$(the director), the dielectric tensor at position $\vec{r}'$ and time t' in the sample may be written[7],

$$\overleftrightarrow{\varepsilon}(\vec{r}',\, t') = \bar{\varepsilon}\overleftrightarrow{I} + \delta\overleftrightarrow{\varepsilon}(\vec{r}',\, t') \tag{2.2}$$

where $\delta\overleftrightarrow{\varepsilon}(\vec{r}',\, t')$ is the non-uniform contribution due to thermal fluctuations, $\overleftrightarrow{I}$ is the second rank identity tensor, and $\bar{\varepsilon} = (2\varepsilon_\perp + \varepsilon_\parallel)/3$ [8] is the average dielectric constant with $\varepsilon_\perp$, $\varepsilon_\parallel$ being the dielectric constants for light polarized perpendicular and parallel to $\hat{n}_0$, respectively.

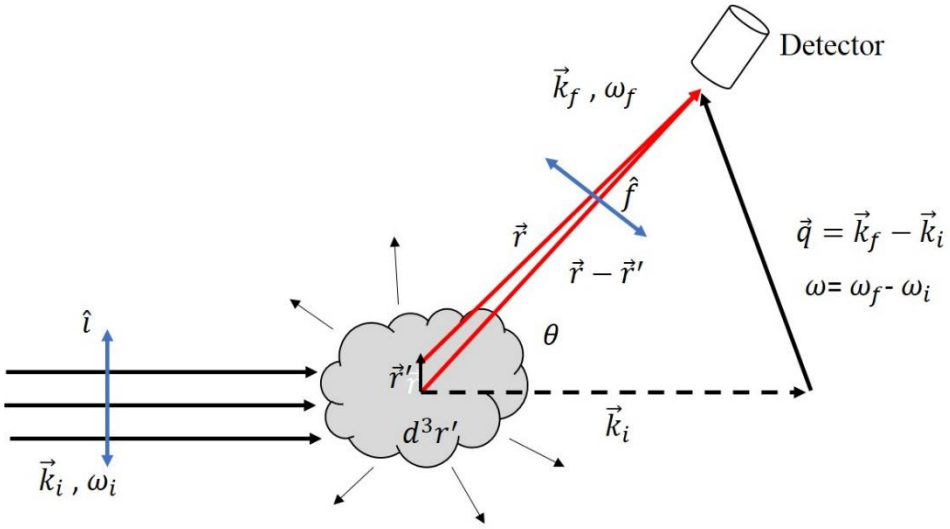

Figure 2-1: Light of incident polarization $\hat{\boldsymbol{\imath}}$ and wave vector $\vec{\boldsymbol{k}}_{\boldsymbol{i}}$ with center frequency $\boldsymbol{\omega_i}$ is scattered in all direction from a transparent medium and arrives at the detector at position $\vec{\boldsymbol{r}}$ with respect to the center of illuminated volume with wave vector $\vec{\boldsymbol{k}}_{\boldsymbol{f}}$, center frequency $\boldsymbol{\omega_f}$, polarization $\hat{\boldsymbol{f}}$, and scattering vector $\vec{\boldsymbol{q}} = \vec{\boldsymbol{k}}_{\boldsymbol{f}} - \vec{\boldsymbol{k}}_{\boldsymbol{i}}$. The total radiated field at the detector is the superposition of the fields radiated from all infinitesimal volumes $\boldsymbol{d^3r'}$ at position $\vec{\boldsymbol{r}}'$with respect to the center of the illuminated volume. In quasi-elastic scattering $\boldsymbol{\omega_i = \omega_f}$ and $\left|\vec{\boldsymbol{k}}_{\boldsymbol{i}}\right|^2 = \left|\vec{\boldsymbol{k}}_{\boldsymbol{f}}\right|^2$(Source: Reproduced from K. P. Neupane PhD dissertation 2009 [6]).

From classical radiation theory, it can be shown the electric field of the light scattered by the dielectric fluctuations at a position $\vec{r}$ outside the sample (where $\varepsilon = \varepsilon_0$) and at a time *t*, and polarized along an analyzer direction $\hat{f}$, is given by [7],

$$\vec{E}_s(\vec{r},t) = -\frac{k_f^2 E_0}{4\pi\varepsilon_0 r} e^{i(\hat{k}_f\cdot\vec{r}-\omega_i t)} \int d^3\, r' \hat{f} \cdot [\hat{k}_f \times (\hat{k}_f \times \delta\overleftrightarrow{\varepsilon}(\vec{r}',\, t')\cdot\hat{\imath})] e^{-i\vec{q}\cdot\vec{r}'} \tag{2.3}$$

Here $\vec{q} = \vec{k}_f - \vec{k}_i$ is the scattering vector, which represents the electromagnetic momentum transfer to the sample, and we have used $\omega_f = \omega_i$ (no frequency shift for QELS), and replaced t' with t because fluctuations is much slower than the time it takes for light to propagate from the sample position at $\vec{r}'$ to the detector at $\vec{r}$. Eq. (2.3) also assumes single scattering – i.e., the sample is sufficiently thin so that the probability incident photons scatter more than once within the sample is negligible. We can simplify the integrand in Eq. (2.3) by using the "BAC-CAB" identity for the double cross product, and noting that $\hat{f}\cdot\hat{k}_f = 0$. This gives:

$$-\hat{f}\cdot\left[\hat{k}_f \times \left(\hat{k}_f \times \delta\overleftrightarrow{\varepsilon}(\vec{r}',\, t')\cdot\hat{\imath}\right)\right] = \hat{f}.\delta\overleftrightarrow{\varepsilon}.\hat{\imath} = \delta\varepsilon_{if}(\vec{r},t) \tag{2.4}$$

Then Eq. (2.3) becomes:

$$\vec{E}_s(\vec{r},t) = -\frac{k_f^2 E_0}{4\pi\varepsilon_0 r} e^{i(\vec{K}_f\cdot\vec{r}-\omega_i t)} \int d^3\, r' e^{-i\vec{q}\cdot\vec{r}'} \delta\varepsilon_{if}(\vec{r}',t) \tag{2.5}$$

When the fluctuations in $\overleftrightarrow{\varepsilon}$ relax on time scales longer than $\sim 10^{-7}$ seconds, they are effectively probed by time-domain analysis of the scattered light, and specifically

through the time correlation function of the scattered light intensity ($I_s = E_s E_s^*$), defined by

$$\langle I_s\,(0) I_s(\tau)\rangle = \langle E_s^*(0)\; E_s(0) E_s^*(\tau)\; E_s(\tau)\rangle \equiv \lim_{T\to\infty} \frac{1}{T}\int_0^T I_s\,(t) I_s(t+\tau) dt \tag{2.6}$$

Here τ is the time delay between the intensity measurements, $\langle \ldots \rangle$ is a time average, which is equivalent to an average over thermally excited states of $\overleftrightarrow{\varepsilon}$ (configurational average) when the system is in thermodynamic equilibrium [5]. If the scattering is collected from large number of spatially uncorrelated subvolumes, then the fluctuations of I_s are a statistical process governed by a Guassian probability distribution [9] and four-point field correlation function in Eq. (2.6) reduces to the sum of two-point correlations:

$$\langle I_s\,(0) I_s(\tau)\rangle = \langle E_s^*(0)\; E_s(0) E_s^*(\tau)\; E_s(\tau)\rangle = |\langle E_s^*(0) E_s(\tau)\rangle|^2 + \langle |E_s(0)|^2\rangle^2 \tag{2.7}$$

Using Eq. (**2.5**), the time correlation function of the scattered field will be:

$$\langle \vec{E}_s^*(\vec{r},0)\; \vec{E}_s(\vec{r},\tau)\rangle = -\frac{k_f^4 |E_0|^2}{(4\pi\varepsilon_0)^2 r^2} e^{i\omega_i \tau} \int d^3 r' \int d^3 r'' e^{-i\vec{q}\cdot(\vec{r}''-\vec{r}')} \langle \delta\varepsilon_{if}(\vec{r}',0)\delta\varepsilon_{if}(\vec{r}'',\tau)\rangle \tag{2.8}$$

The integrals over illuminated volume V are just Fourier transforms of $\delta\varepsilon_{if}$, so that

$$\langle E_s^*(\vec{r},0)\; E_s(\vec{r},\tau)\rangle = \frac{k_f^4 |E_0|^2 V^2}{(4\pi\varepsilon_0)^2\, r^2}\; \langle \delta\varepsilon_{if}^*(\vec{q},\,0)\delta\varepsilon_{if}(\vec{q},\,\tau)\rangle e^{-i\omega_i\tau} \tag{2.9}$$

One then needs to calculate $\langle \delta\varepsilon_{if}^{*}(\vec{q},\, 0)\delta\varepsilon_{if}(\vec{q},\, \tau)\rangle$ for the particular system of interest. We will consider this further in sec. 2.4 below.

2.3 DIGITAL PHOTON CORRELATION

In the dynamic light scattering (DLS) technique, scattered light is collected on a detector – typically, a photomultiplier tube (PMT) – and converted into a time series of current pulses each representing a single (or a few) photons. The photocurrent is converted to a voltage, amplified, and passed through a discriminator circuit, from which it emerges as temporal sequence of logic level pulses. In a time-domain analysis – a method known as photon correlation spectroscopy (PCS) – these pulses are correlated in time using a combination custom hardware and software developed by Dr Alan Baldwin at Kent State University. The time correlation function of the scattered intensity, $\langle I_s\,(0) I_s(\tau)\rangle$, is thereby obtained.

In an autocorrelation measurement, the signal from a single PMT is correlated with the signal from the same PMT at later times. One of the limitations of autocorrelation is the finite resolving time ("dead time") of the PMT for two photons closely spaced in time. The typical dead time is on the order of tens of nanoseconds, and causes an artificial drop in $\langle I_s\,(0) I_s(\tau)\rangle$ when $\tau < 100$ nsec. A second significant limitation is "afterpulsing" – i.e., current pulses generated by reflections of photoelectrons as they cascade through the pulse amplification section of the PMT. Afterpulsing produces large false autocorrelation at delay times τ in the range 50 nsec – 1 μsec.

Both limitations can be overcome by cross correlating the signal from two independent photomultipliers, each illuminated with ~50% of the collected scattered light. Separate photons still can arrive at the second detectors within the dead time of the first one and can be accurately counted. Also, afterpulses between two independent detectors are uncorrelated. To implement the cross-correlation method, we split the collected scattered light using a 50/50 non-polarizing beam splitter, and passed the two output beams to two PMTs of the same type and model.

Normalized field and intensity correlation functions are defined as [10], [11],

$$g^{(1)}(\tau) = \frac{\langle E_s^*(0)\, E_s(\tau)\rangle}{\langle |E_s(0)|^2\rangle} \qquad g^{(2)}(\tau) = \frac{\langle I_s(0)\, I_s(\tau)\rangle}{\langle |I_s(0)|^2\rangle} \tag{2.10}$$

In an actual experiment, the functions $g^{(2)}(\tau)$ and $g^{(1)}(\tau)$ are related by the Siegert relation[10][11].

$$g^{(2)}(\tau) = 1 + \beta(g^{(1)}(\tau))^2 \tag{2.11}$$

where β is called the spatial coherence factor. When the field is scattered purely from thermal fluctuations in the sample and is spatially coherent over the detection aperture, then Eq. (2.7) gives Eq. (2.11) with $\beta = 1$. In case of spatial incoherence at the aperture, or in the presence of scattering from static inhomogeneities in the substrates containing the sample or from textural defects in the sample, the coherence factor is reduced, $0 < \beta < 1$. To optimize β – and therefore optimize the amplitude of $g^{(2)}(\tau)$ relative to its background value of 1 – one must limit the detection aperture area to approximately on "coherence area" given by[9],

$$A_{coh} \approx \frac{\lambda^2}{\Omega} \tag{2.12}$$

Here Ω is the solid angle subtended by the illuminated sample volume at the detector and λ is the illuminating wavelength. In our experiment, we optimized the light collection aperture and minimized the stray scattering to achieve typical $\beta > 0.9$.

2.4 LIGHT SCATTERING FROM DIRECTOR FLUCTUATIONS IN A UNIAXIAL NEMATIC PHASE

The spontaneous fluctuations in molecular orientation that scatter light in nematics may be described in terms of three fundamental bulk deformations of the average molecular alignment (director $\hat{n}$), called *splay*, *twist*, and *bend* (see Fig. 1.3). To discuss light scattering from fluctuation modes of the director, it is necessary to determine the combinations of splay, twist, and bend distortions that contribute to these modes.

2.4.1 ELASTIC FREE ENERGY OF A UNIAXIAL NEMATIC PHASE AND NORMAL MODES

The length of molecules in typical rod-like molecules in nematic phase are about (2-3 nm) which is much smaller than optical wavelength (~500 nm) used in light scattering experiments. So a continuum approach, which was first developed by C. Oseen [12] and H. Zocher [13] and then further advanced by F.C. Frank [14] and J.L. Erickson [15], may be used to interpret the measurements. In this approach, $\hat{n}$ is treated as a dimensionless field $\hat{n} = \hat{n}(\vec{r})$. As presented in Chapter 1, the bulk elastic free energy density of nematic

phase, associated with the distortions of the director $\hat{n}$, is given in terms of gradients in $\hat{n}$ corresponding to splay, twist, and bend by [11],

$$F_N = \int d\vec{r}\ f_N(\vec{r}) = \int d\vec{r}\,[\frac{K_{11}}{2}(\vec{\nabla}.\hat{n})^2 + \frac{K_{22}}{2}(\hat{n}.\vec{\nabla}\times \hat{n})^2 + \frac{K_{33}}{2}(\hat{n}\times\vec{\nabla}\times\hat{n})^2\,] \quad (2.13)$$

where K_{11}, K_{22} and K_{33} are splay, twist and bend elastic constants, respectively, with units of energy per length or force (Newtons, N).

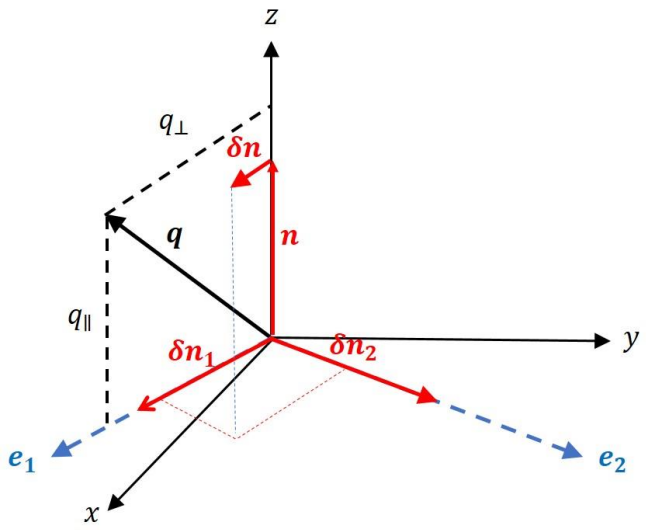

Figure 2-2: Coordinate system that illustrates the normal modes of the director for uniaxial nematic liquid crystal (Source: reproduced from T. Ostapenko PhD dissertation, 2011 [16]).

Fig. 2.2 shows schematically the geometries used to find the normal modes of the director – i.e., the linear combinations of fluctuations δn_x and δn_y that diagonalize F_N,

assuming the average director $\hat{n}_0 = \hat{z}$. We may write as the sum of a uniform part and a non-uniform, fluctuating part $\delta\hat{n}(\vec{r})$ as follows:

$$\hat{n}(\vec{r}) = \sqrt{1 - \delta n_x^2(\vec{r}) - \delta n_y^2(\vec{r})}\hat{z} + \delta n_x(\vec{r})\hat{x} + \delta n_y(\vec{r})\hat{y} \tag{2.14}$$

$$\approx \hat{z} + \delta n_x(\vec{r})\hat{x} + \ \delta n_y(\vec{r})\hat{y}$$

After applying a Fourier transformation to the fluctuating part of $\hat{n}$,

$$\delta n_j(\vec{r}) = \textstyle\sum_{\vec{q}} \delta n_j(\vec{q}) e^{iq.\vec{r}} \quad j = x, y\,, \tag{2.15}$$

the nematic free energy in Eq. (1.1) may be written in q space as:

$$F_N = \frac{V}{2}\sum_q \Big[K_{11}\left|\delta n_x(\vec{q})q_x + \delta n_y(\vec{q})q_y\right|^2 + K_{22}\left|\delta n_x(\vec{q})q_y - \delta n_y(\vec{q})q_x\right|^2 \tag{2.16}$$

$$+ K_{33}q_z^2\left(|\delta n_x(\vec{q})|^2 + \left|\delta n_y(\vec{q})\right|^2\right)\Big]$$

Eq. (2.16) can be diagonalized by the linear transformation,

$$\delta\vec{n} = \delta n_1\hat{e}_1 + \delta n_2\hat{e}_2 \tag{2.17}$$

where $\hat{e}_2 = \frac{\hat{n}_0\times\vec{q}}{|\hat{n}_0\times\vec{q}|}$ and $\hat{e}_1 = \frac{\hat{e}_2\times\hat{n}_0}{|\hat{e}_2\times\hat{n}_0|}$. Expressing δn_x, δn_y in terms of δn_1, δn_2, using $\hat{n}_0 = \hat{z}$, and substituting into Eq. (2.16), we obtain,

$$F_N = \frac{V}{2}\sum_q [(K_{11}q_\perp^2 + K_{33}\,q_z^2)|\delta n_1(\vec{q})|^2 + (K_{22}q_\perp^2 + K_{33}\,q_z^2)|\delta n_2(\vec{q})|^2] \tag{2.18}$$

where $q_\perp = \sqrt{q_x^2 + q_y^2}$ and $q_\parallel = q_z$ are components of the wavevector $\vec{q}$ perpendicular and parallel to $\hat{n}_0$.

Applying the equipartition theorem to Eq. (2.18) yields the mean square amplitude of the normal fluctuation modes of $\hat{n}$:

$$\langle|\delta n_1(\vec{q})|^2\rangle = \frac{k_\beta T}{V}\frac{1}{K_{11}q_\perp^2 + K_{33}\,q_z^2} \qquad \langle|\delta n_2(\vec{q})|^2\rangle = \frac{k_\beta T}{V}\frac{1}{K_{22}q_\perp^2 + K_{33}\,q_z^2} \tag{2.19}$$

The first mode in Eq. (2.19) is a combination of splay and bend deformations (splay-bend mode) and second mode is a combination of twist and bend (twist-bend mode).

2.4.2 DYNAMICS OF THE DIRECTOR MODES

The hydrodynamic theory of nematics was developed by Ericksen [17], Leslie [18] and Parodi [19], and later derived from more fundamental considerations by the Harvard group [20]. In the simplest formulation, the equations of nemato-hydrodynamics are a balance of elastic and viscous torques acting on $\delta n_{1,2}(\vec{q})$ [7]. The elastic torque density is,

$$h_\alpha(\vec{q}) = \frac{\partial F_N(\vec{q},t)}{\partial \delta n_\alpha(\vec{q},t)} = (K_{\alpha\alpha}q_\perp^2 + K_{33}\,q_z^2)\delta n_\alpha(\vec{q},t) \tag{2.20}$$

$$\alpha = 1{,}2$$

and the viscous torque density is given by,

$$-\eta_\alpha(\vec{q})\frac{\partial \delta n_\alpha(\vec{q},t)}{\partial t} \tag{2.21}$$

where $\eta_\alpha(\vec{q})$ are effective viscosities, in units of energy × time / (length)^3 (or kg/m-s = Pa s), that account for a frictional resistance in the nematic LC to orientational deformations of $\hat{n}$. The effective viscosities are combinations of five fundamental viscosities in a uniaxial nematic phase [21].

The equations of motion of the director modes $\delta n_{1,2}$ are obtained equating (2.20) and (2.21):

$$-\eta_\alpha(\vec{q})\frac{\partial \delta n_\alpha(\vec{q},t)}{\partial t} = (K_{\alpha\alpha}q_\perp^2 + K_{33}\, q_z^2)\delta n_\alpha(\vec{q},t) \tag{2.22}$$

The solutions to Eq. (2.22) are simple decaying exponentials,

$$\delta n_\alpha(\vec{q},t) = \delta n_\alpha(\vec{q},0)e^{-\Gamma_\alpha(\vec{q})t} \tag{2.23}$$

$$\alpha = 1{,}2$$

corresponding to overdamped motion, with relaxation rates

$$\Gamma_\alpha = \frac{K_{\alpha\alpha}q_\perp^2 + K_{33}\, q_z^2}{\eta_\alpha(\vec{q})} \tag{2.24}$$

The five independent, fundamental viscosities of a uniaxial nematic may be taken to be [7] three anisotropic fluid flow viscosities η_a, η_b, η_c, a twist viscosity, γ_1, describing the rotations of the director with respect to the background fluid, and another viscosities $\alpha_1, \alpha_2, \alpha_{3,}\alpha_4, \alpha_5$ are Leslie coefficients. In terms of these fundamental viscosities, the effective viscosities η_a are given by [7], [11]:

$$\eta_1(\vec{q}) = \gamma_1 - \frac{(q_\perp^2\alpha_3 - q_z^2\alpha_2)^2}{q_\perp^4\eta_b + q_\perp^2 q_z^2\,(\alpha_1+\alpha_3+\alpha_4+\alpha_5) + q_z^4\eta_c} \tag{2.25}$$

$$\eta_2(\vec{q}) = \gamma_1 - \frac{q_z^2\alpha_2^2}{q_\perp^2\eta_a + q_z^2\,\eta_c}$$

For different choice of wavevector $\vec{q}$, $\eta_1(\vec{q})$ and $\eta_2(\vec{q})$ reduce to simpler forms. We will describe specific choices used in our experiments later in Chapter 5.

2.4.3 OPTICAL SELECTION RULES FOR UNIAXIAL NEMATIC

The orientational state of a uniaxial nematic can be characterized mathematically by a second-rank tensor $Q_{\alpha\beta}$, which ensures invariance under inversion of $\hat{n}$,

$$Q_{\alpha\beta} = \frac{3}{2} S \left[n_\alpha n_\beta - \frac{1}{3} \delta_{\alpha\beta} \right] \tag{2.26}$$

where $\alpha, \beta = x, y, z$, $\delta_{\alpha\beta}$ is Kronecker's delta function, and S is a temperature-dependent scalar quantity called the scalar order parameter defined by:

$$S = \frac{\Delta\chi}{\Delta\chi_{sat}} \tag{2.27}$$

Here $\Delta\chi = \chi_{\parallel} - \chi_{\perp}$ is the temperature-dependent, but essentially frequency-independent, diamagnetic anisotropy of a uniaxial nematic (with subscripts parallel and perpendicular referring to the values of ε when a magnetic field is applied parallel or perpendicular to $\hat{n}_0$), and $\Delta\chi_{sat}$ is the saturated value of χ, which corresponds to the molecular long axis being perfectly aligned along $\hat{n}_0$.

Then the dielectric tensor of a uniaxial nematic can be expressed as[11]:

$$\varepsilon_{\alpha\beta} = \bar{\varepsilon}\delta_{\alpha\beta} + \tfrac{2}{3}\Delta\varepsilon_{sat}\, Q_{\alpha\beta} \tag{2.28}$$

where $\bar{\varepsilon} = (2\varepsilon_{\perp} + \varepsilon_{\parallel})/3$ is the mean dielectric constant. Using Eq. (2.26) we get,

$$\varepsilon_{\alpha\beta} = \bar{\varepsilon}\delta_{\alpha\beta} + \Delta\varepsilon_{sat}\tfrac{3}{2} S \left[n_\alpha n_\beta - \tfrac{1}{3}\delta_{\alpha\beta} \right] \tag{2.29}$$

or, using Eq. (2.27),

$$\varepsilon_{\alpha\beta} = \varepsilon_{\perp}\delta_{\alpha\beta} + (\varepsilon_{\parallel} - \varepsilon_{\perp}) n_\alpha n_\beta = \varepsilon_{\perp}\delta_{\alpha\beta} + \Delta\varepsilon\, n_\alpha n_\beta \tag{2.30}$$

To linear order in the small fluctuations δn_α about $\hat{n}_0$, fluctuations of the dielectric tensor $\delta\varepsilon_{\alpha\beta}$ are related to δn_α by:

$$\delta\varepsilon_{\alpha\beta} = \Delta\varepsilon\left(n_\alpha \delta n_\beta + n_\beta \delta n_\alpha\right) \tag{2.31}$$

If the incident light in a light scattering experiment has polarization $\hat{\imath}$ and the scattered light has polarization $\hat{f}$, from Eq. (2.31) the component of dielectric tensor fluctuations picked out will be,

$$\delta\varepsilon_{if} = \sum_{\alpha,\beta} f_\alpha \delta\varepsilon_{\alpha,\beta} i_\alpha = \Delta\varepsilon\left[(\hat{n}_0.\hat{\imath}\,)\left(\delta\vec{n}\,.\hat{f}\right) + (\hat{n}_0.\hat{f})(\delta\vec{n}.\hat{\imath}\,)\right] \tag{2.32}$$

which, using Eq. (2.17), becomes:

$$\begin{aligned}\delta\varepsilon_{if} = \Delta\varepsilon\big[&\delta n_1\{(\hat{n}_0.\hat{\imath}\,)\left(\hat{e}_1\,.\hat{f}\right) + (\hat{n}_0.\hat{f})(\hat{e}_1.\hat{\imath}\,)\} + \\ &\delta n_2\{\{(\hat{n}_0.\hat{\imath}\,)\left(\hat{e}_2\,.\hat{f}\right) + (\hat{n}_0.\hat{f})(\hat{e}_2.\hat{\imath}\,)\}\big]\end{aligned} \tag{2.33}$$

From Eq. (2.9) the intensity I_s of the scattered light is proportional to $\langle\delta\varepsilon_{if}^*(\vec{q},0)\delta\varepsilon_{if}(\vec{q},0)\rangle$, where $\vec{q}$ is the fluctuation vector selected in the light scattering experiment. Then, using Eq. (2.19) and taking $\hat{n}_0 \parallel \hat{z}$, one may calculate:

$$I_s(\vec{q}) \propto \langle\left|\delta\varepsilon_{if}(\vec{q},0)\right|^2\rangle = \frac{K_B T(\Delta\varepsilon)^2}{V}\left[\frac{G_1}{\lambda_1} + \frac{G_2}{\lambda_2}\right] \tag{2.34}$$

where

$$G_1 = \left\{(\hat{\imath})_z\left(\hat{f}\right)_1 + (\hat{f})_z(\hat{\imath})_1\right\}^2,\ G_2 = \left\{(\hat{\imath})_z\left(\hat{f}\right)_2 + (\hat{f})_z(\hat{\imath})_2\right\}^2, \tag{2.35}$$

$$\lambda_1 = K_{11}q_\perp^2 + K_{33}q_z^2 \text{ and } \lambda_2 = K_{22}q_\perp^2 + K_{33}q_z^2 \tag{2.36}$$

By choosing specific polarizer and analyzer orientations $\hat{\imath}$, $\hat{f}$, we can isolate a specific normal mode of the director fluctuations. In addition, by making q_z or $q_\perp$equal to zero, we can in principle pick out scattering from pure splay, twist or bend fluctuations.

2.4.4 RELATION OF SCATTERING VECTOR TO INCIDENT AND SCATTERING ANGLES IN THE LIGHT SCATTERING EXPERIMENT

For given $\vec{k}_i$, $\vec{k}_f$, the light scattering experiment picks out fluctuations with the wavevector $\vec{q} = \vec{k}_f$-$\vec{k}_i$. where $\vec{k}_i$, $\vec{k}_f$ are the wavevectors of the incident and scattered light. Let θ be the angle in the laboratory between $\vec{k}_i$ and $\vec{k}_f$. Thus, fluctuations with different $\vec{q}$ can be studied if, for example, the angle θ is changed for fixed $\vec{k}_i$. In this case, θ is referred to as the scattering angle.

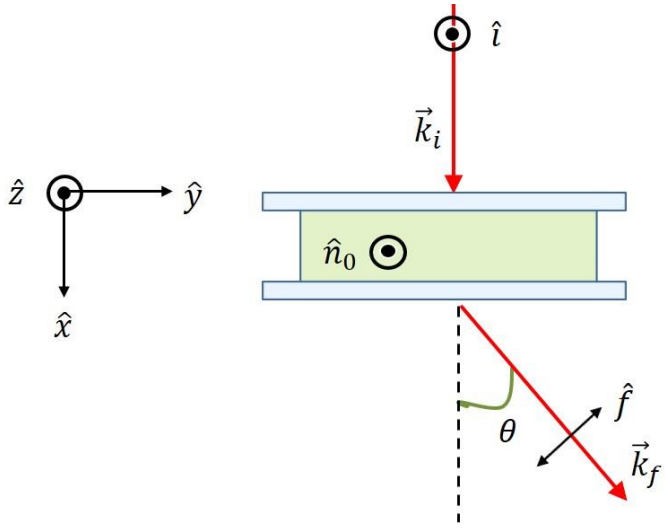

Figure 2-3: DLS set-up with planar cell alignment. $\vec{k}_i$, $\vec{k}_f$ are incident and scattering wave vector. $\hat{\imath}$, $\hat{f}$ are polarization of incident and scattering light.

For the geometry shown in Figure 2-3, we have $\vec{k}_i = k_i\hat{x} = \frac{2\pi}{\lambda}n_i\hat{x}$ and $\vec{k}_f = k_f\cos\theta'\,\hat{x} + k_f\sin\theta'\,\hat{z} = \frac{2\pi}{\lambda}(n_s\cos\theta'\,\hat{x} + n_s\sin\theta'\,\hat{z})$. Here λ is the wavelength of the incident laser light in air (we apply the quasi-elastic limit where λ does not shift in the scattering process), θ' is the scattering angle in the liquid crystal medium, and n_i, n_s are refractive indices for the incident and scattered light in the LC medium. The angles θ, θ' are related by Snell's law, $\sin\theta = n_s\sin\theta'$, where we approximated $n_{air} \approx 1$. Then the scattering vector is given by

$$\vec{q} = \frac{2\pi}{\lambda}(n_s\cos\theta' - n_i)\hat{x} + \frac{2\pi}{\lambda}n_s\sin\theta'\,\hat{z} \tag{2.37}$$

$$= \frac{2\pi}{\lambda}(\sqrt{n_s^2 - \sin^2\theta} - n_i)\hat{x} + \frac{2\pi}{\lambda}\sin\theta\,\hat{z}$$

The values of n_i, n_s depend on the incident and scattered light polarizations (i.e., polarizer and analyzer orientations) with respect to the average molecular alignment (director $\hat{n}_0$), and on the angle θ. We will describe specific choices of these parameters used in our experiments in later chapters.

2.5 EXPERIMENTAL SET UP FOR DYNAMIC LIGHT SCATTERING

Key components of our light scattering set up are displayed schematically in Figure 2-4 actual images of some of these components are provided in subsequent figures. The laser light sources, major optical components, and two circle goniometer for selecting the incident and scattering wavevectors were mounted on a vibration isolated optical table (Newport Corporation, model RS4000).

Following the schematic in Figure 2-4, the linearly polarized incident laser beam is steered by a mirror through an aperture and half wave plate that allows the polarization to be rotated. This is used in concert with a fixed polarizer downstream of the waveplate to control the intensity of the laser light incident on the sample. The axis of the polarizer is perpendicular to the optical table, resulting in vertically polarized light incident on the sample. In order to provide a clean Gaussian beam and to expand the beam diameter prior to focusing on the sample, we used a spatial filter consisting of a microscope objective, a pinhole aperture with fine positional adjustments, and a collimating lens.

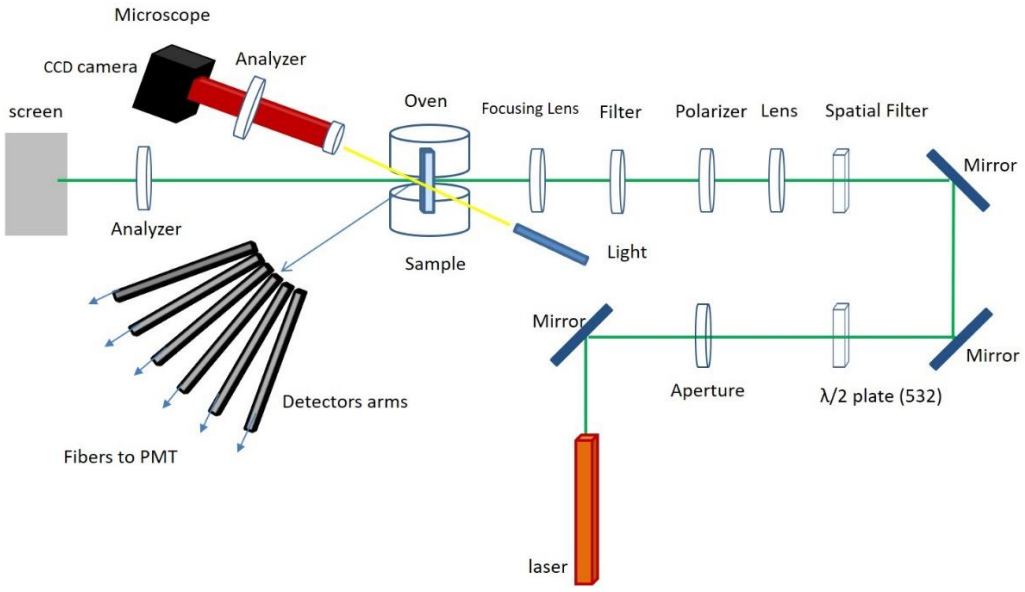

Figure 2-4: Schematic diagram of the experimental light scattering apparatus set up.

The spatial filter removes light from secondary sources, such as optical components between the laser discharge and position of the spatial filter, which contaminate the Gaussian beam profile. The collimated output of the spatial filter is passed through the fixed polarizer and then focused by a lens (150 mm focal length) down to an ~50 μm diameter at the sample.

All of samples were contained in flat optical cells – two planar glass substrates of 1 mm thickness sandwiching a thin (~10 μm) layer of liquid crystal material. Typically, the inner surfaces of the substrates were treated with thin polymer alignment layers to promote a uniform orientation of the equilibrium director. The sample cells were placed in either a custom-made oven or a commercial hot stage, with suitable optical access for the incident and scattered light.

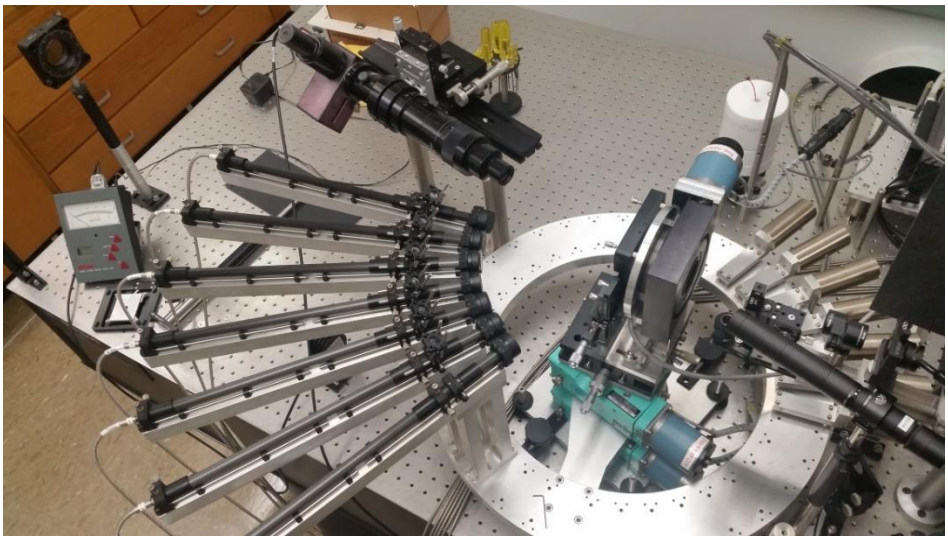

Figure 2-5: Photograph of dynamic light scattering set up in the lab.

The scattered light from the samples was collected at up to six scattering angles simultaneously, spaced by fixed 10° increments. The base value of these angles, as well as the angle of the incident light on the sample cell, could be varied continuously using the two independent rotating stages of the two-circle goniometer (Huber, model 410). The stages could be either manually rotated to set the scattering angles or by stepper motors (Superior Electric) with a resolution of 400 steps /degree, which were controlled by a computer interfaced motion controller (Advanced Control Systems, model MCU-2).

At each scattering angle, light was collected by a detection arm, shown in the Figure 2-5, on which was mounted a $500\ \mu m$ pinhole aperture, an analyzer, an imaging lens, and an optical fiber placed in the image plane and secured to an XY translation stage to allow the fiber tip to be precisely positioned in the image plane. The axis of the analyzer was set

to a horizontal orientation – i.e., perpendicular to the vertical incident light polarization. The $500\ \mu m$ pinhole was selected so that approximately a single coherence solid angle of the scattered field (as defined in Eq. (2.12) was admitted.

The imaging lens produces a real image of the scattering volume in the sample on the fiber tip and eliminates admission of light scattered from other sources that would degrade the signal to background ration in the measure intensity correlation function. Function helps to eliminate any light from sources other than the illuminated volume of the sample. The optical fibers at each of the six scattering angle positions conducted the scattered light to individual beam-splitting prisms, which directed ~50% of the light to each of two independent PMT detectors for the cross-correlation measurements.

2.5.1 OVEN AND HOT STAGE WITH OPTICAL ACCESS FOR LIGHT SCATTERING

Figure 2-6 shows the home-made oven used to house and control the temperature of the LC samples in some of our light scattering measurements. The oven has a broad but narrow annular slit that allows wide variation of the scattering angle from the sample. The oven was mounted on a XYZ translation stage attached to the inner circle of the two-circle goniometer. This translation stage allows sample oven to move independently in XYZ directions and provides sufficient movement of the sample cell to find a clean spot (defect free region) in the sample for high-quality measurements.

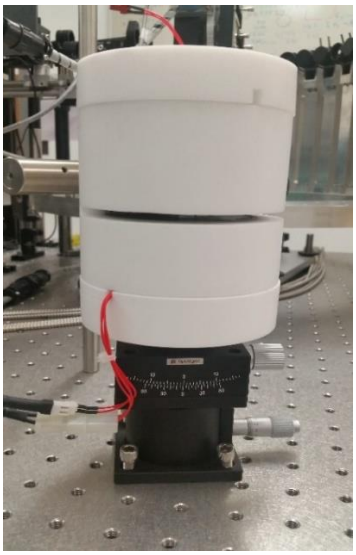

Figure 2-6: Custom made oven for sample cell

The temperature of the oven was regulated and monitored by a precision temperature controller (Stanford Research Systems, model PTC10, Figure 2-7.) An ultrastable thermistor, placed in contact with the sample cell, was used as a thermometer. Measured temperature stability was typically $\pm 0.003℃$. For experiments that required greater azimuthal access to the scattered light (i.e., continuous access as the sample is rotated around the direction of the incident light), we utilized a commercial hot stage (Instec model HCS400, shown in Figure 2-8-right).

Figure 2-7: temperature controller Model PTC10

The hot stage has dual heaters located below and above the sample chamber, which minimizes thermal gradients across the sample. Coupled with the Instec mk2000 controller, the hot stage achieves 0.01°C temperature stability. The hot stage was mounted on a motorized rotation stage, enabling it to be continuously rotated about a horizontal axis – i.e., the axis of the incident laser beam. This rotation stage (shown in Figure 2-8-left) is mounted on top of the two-circle goniometer.

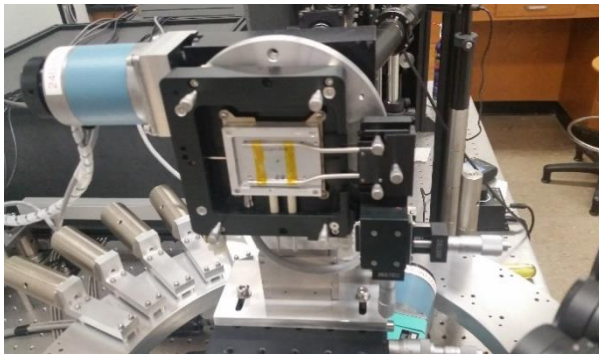

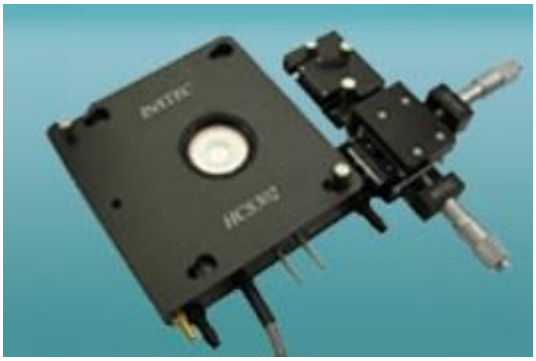

Figure 2-8: Left: Rotation stage in DLS set-up. Right: Instec hot stage model HCS400.

2.5.2 LASER LIGHT SOURCE

Two laser light sources were used in our experiments: a Helium-neon gas laser (Spectra-Physics, model 127) operating at 633 nm and 30 mW power, and an optically pumped semiconductor laser (Coherent, model Genesis MX-STM, Figure 2-9) operating at 532 nm and typical output power of 100 mW. Both lasers output optical radiation with a single transverse mode (TEM00) yielding a Gaussian intensity profile.

Figure 2-9: Genesis^{TM} MX STM/SLM laser and power supply(Image from: https://www.coherent.com/lasers/laser/genesis-mx-slm-series)

2.5.3 POWER METER

Figure 2-10: Ophir Photonics Orion laser power/energy meter

The incident laser power was independently monitored by an Ophir Photonics Orion laser power/energy meter (shown in Figure 2-10) before and after recording each intensity correlation function. The power readings were used to normalize the measured intensity of the scattered light against small drifts or variations in laser power.

2.5.4 LONG DISTANCE OPTICAL MICROSCOPE

We employed a long distance, polarizing optical microscope (Infinity Photooptical, model K2/SC, shown in Figure 2-11), which was coupled to a CCD camera (Allied Vision Technologies, Stingray F201C).The microscope was mounted on a rail to position it at the proper height and rough distance from the sample for imaging the scattering volume with white light. Fine positioning and focusing was achieved using precision translation stages to which the microscope body was mounted.

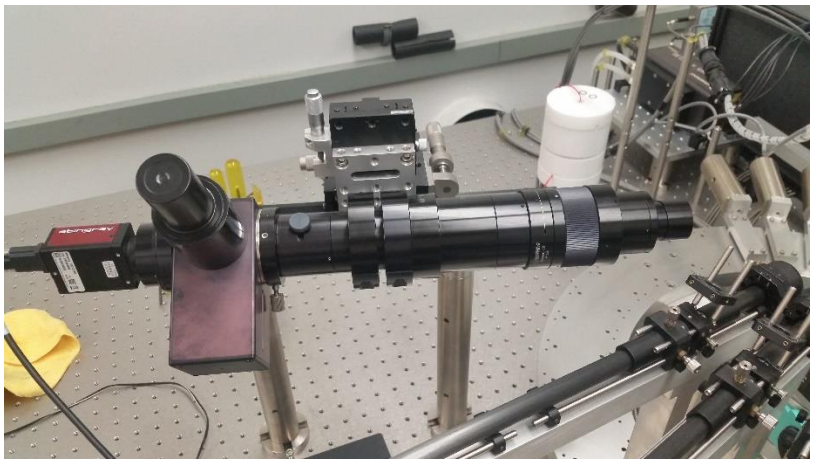

Figure 2-11: Long distance optical microscope.

The microscope was used to monitor the texture of the sample, surrounding and including the volume illuminated by the focused laser beam, in real time. This enabled us to ensure that only defect-free regions were studied in our light scattering measurements and also to precisely confirm the temperatures of phase transitions.

2.5.5 The GPX TIME–DIGITIZING CORRELATOR AND PHOTODETECTORS

The GPX time-digitizing correlator was used in our experiments to compute the time correlation function of the scattered light intensity. Dr. Alan Baldwin from Physics Department of Kent State University designed, built, tested, and commissioned the correlator hardware and software.

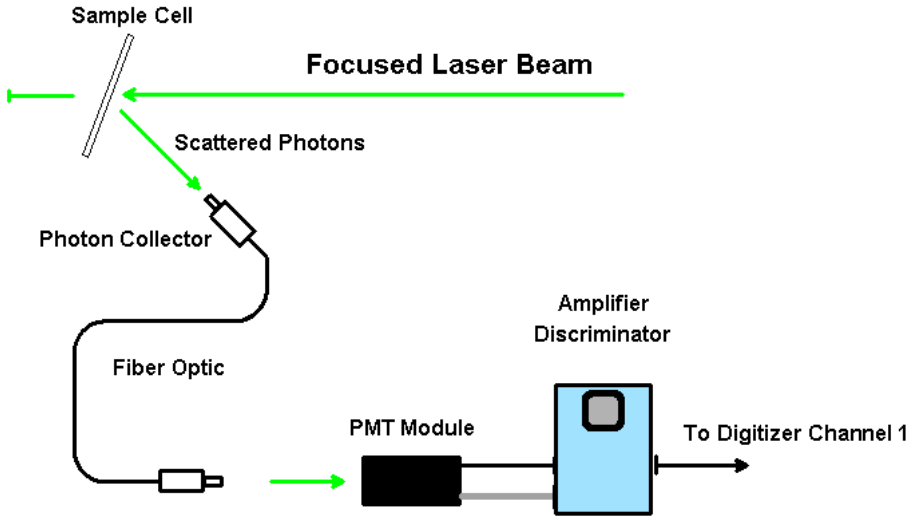

Figure 2-12: Diagram shows Auto-correlation in DLS set-up.

The GPX Time-Digitizing Correlator instrument has 12 time-digitizing channels which can process Auto and Cross Correlations (Figure 2-12 and Figure 2-13) over a time range of 100/50/33 picoseconds to 1000 seconds per correlation bin. The basic system is composed of a hardware time-digitizer which records the arrival time of voltage pulses representing detected photons in 12 data channels, and a software package which controls the acquisition, computes the various correlation functions, and displays the results in real time.

The Gpx Time-Digitizer acquisition software package has two components: (I) GAdvisor.exe: the program which provides the user interface for system configuration,

data acquisition, and visualization of the acquired data. (II) GpxCorr.dll: the acquisition and computational core of the system.

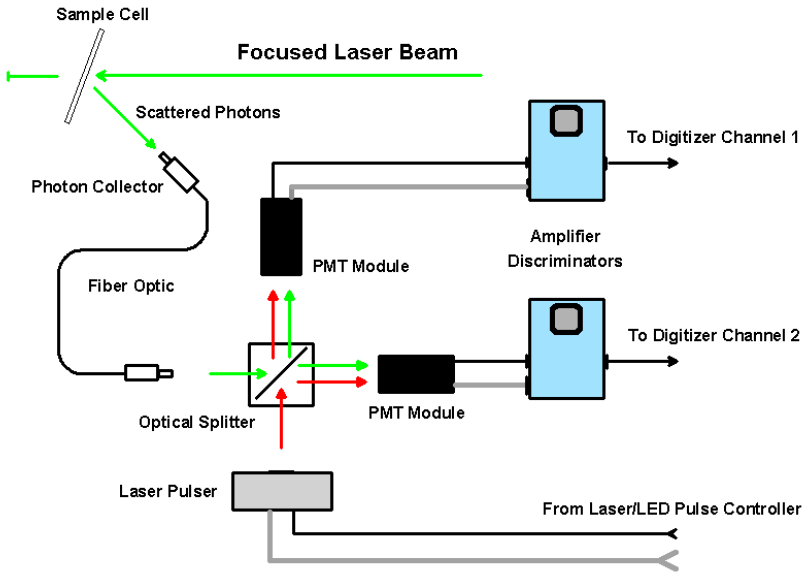

Figure 2-13: Diagram shows Cross-correlation in DLS set-up.

The Photomultiplier tube (PMT) detectors used to convert scattered photons to photoelectrons and then to current pulses (Hamamatsu model *P*30*CWAD*5*F*-56) had conversion efficiency of ~12% at the laser wavelengths employed, and a relatively low dark count rate of <100 counts/s. The current pulses from the PMTs were passed through amplifier/discriminator circuits, also designed and constructed by Dr. Baldwin, which produced a fixed amplitude voltage pulse for each photon detected. These pulses were then fed into the inputs of the Gpx correlator.

2.6 REFRENCES

[1] S. Kumar, *Liquid Crystals,Experimental Study of Physical Properties and Phase Transitions*. Cambridge: Cambridge University Press, 2011.

[2] and P. S. P. P. C. Martin, O. Parodi, "Unified Hydrodynamic Theory for Crystals, Liquid Crystals, and Normal Fluids," *Phys. Rev. A*, vol. 6, 1972.

[3] J. B. R Pecora, *Dynamic Light Scattering*. John Wiley, 1975.

[4] L. D. Landau and E. M. Lifshitz, *Electrodynamics of Continuous Media*. Addison Wesley, Reading, MA, 1960.

[5] J. D. Jackson, *Classical Electrodynamics*. New York: wiley, 1963.

[6] K. P. Neupane, "Light Scattering Studies of Orientational Order in Liquid Crystalline Tetrapodes and Lyotropic Chromonic Liquid Crystals," *PhD Diss.*, 2009.

[7] Orsay Group, "No Title," *J. Chem. Phys.*, vol. 51, 1969.

[8] P.G.De Gennes and J.Prost, *The Physics of Liquid Crystals*. Oxford: Clarendon Press, 1993.

[9] B. J. Berne and R. Pecora, *Dynamic Light Scattering: With Applications to Chemistry, Biology, and Physics*. Dover Publication, 2000.

[10] B. Chu, *Laser Light Scattering, Basic Principles and Practice*. Boston: Academic Press, 1991.

[11] L. Mandel, *Progress in Optics*. North Holland, 1963.

[12] C. W. Oseen, "The theory of liquid crystal," *Trans. Faraday Soc*, vol. 29, 1933.

[13] H. Zocher, “The effect of a magnetic field on the nematic state,” *Trans. Faraday Soc.*, vol. 29, 1933.

[14] F. C. Frank, “I. Liquid crystals. On the theory of liquid crystals,” *Faraday Soc*, vol. 25, 1958.

[15] J. L. Ericksen, “Some magnetohydrodynamic effects in liquid crystals,” *Arch. Ration. Mech. Anal.*, vol. 23, no. 4, pp. 266–275, 1966.

[16] T. Ostapenko, *Magneto-optical and imaging studies of chromonic and thermotropic liquid crystals*. Kent State University, 2011.

[17] J. L. Ericksen, “, Arch. Ration,” *Arch. Ration, Mech. Anal.*, vol. 4, 1960.

[18] F. M. Leslie, “SOME CONSTITUTIVE EQUATIONS FOR ANISOTROPIC FLUIDS,” *Q. J. Mech. Appl. Math.*, vol. 19, 1966.

[19] O. Parodi, *J. Phys. Paris*, vol. 31, 1970.

[20] D. Forster, T. C. Lubensky, P. C. Martin, and J. Swift, “Hydrodynamin of liquid crystal.”

[21] C. A. PG De Gennes, “Fluctuations d’orientation et diffusion Rayleigh dans un cristal nématique,” *Sci.*, vol. 266, no. 15, 1968.

CHAPTER 3

FLUCTUATION MODES OF A TWIST-BEND NEMATIC LIQUID CRYSTAL

3.1 INTRODUCTION

In this chapter, the theoretical background and formulation of the light scattering experiment performed in this dissertation are presented. Details of scattering from director fluctuations in nematic liquid crystal, along with relevant optical selection rules to isolate director modes, are reviewed.

The nature of collective fluctuation modes associated with the short-pitch heliconical structure of the N_{TB} phase is an important question, since the spectrum and dispersion ($\vec{q}$ dependence) of these modes are closely related to the basic structural features and to the relevant order parameter(s) of the N_{TB} phase, and because properties of the fluctuations provide an important test of theories describing its formation. Although previous light scattering measurements [1] revealed a softening of the elastic constant associated with bend distortions of the director above the N-N_{TB} transition, they did not probe fluctuation modes specifically associated with the heliconical N_{TB} structure. In this

chapter, we describe a light scattering study of fluctuations within the N_{TB} phase and their critical behavior near the transition.

Our measurements reveal a pair of strongly temperature-dependent nonhydrodynamic ($\vec{q}$ independent) modes plus a single hydrodynamic ($\vec{q}$ dependent) mode in the N_{TB} phase, and a single nonhydrodynamic mode and pair of hydrodynamic modes (the usual director modes of a uniaxial nematic) in the higher-temperature nematic phase.

We demonstrate excellent agreement between the behavior of the observed modes and theoretical predictions based on a "coarse-grained" version of a Landau-de Gennes free energy for the nematic-to-N_{TB} phase transition [2]. The coarse-graining approximation, inspired by earlier theoretical work on cholesterics [3][4] and appropriate in the limit of optical wavelength much longer than the helical pitch, treats surfaces of constant phase in the heliconical N_{TB} structure as "pseudolayers". Within this approximation, which has previously been used to explain the effect of high magnetic fields on the N_{TB} phase [5] and to account for its flow properties [6], the normal fluctuation modes involving the director may be mapped onto those of a chiral smectic-A phase, with an effective layer spacing equal to the pitch, effective director parallel to the local pitch axis, and effective elastic constants that arise from the short-pitch orientational modulation rather than from a true smectic mass density wave.

The Landau-de Gennes theoretical model, which we compare our experimental results to, is based on a linear coupling between spatial gradients in the orientation of the molecular long axis (director $\hat{n}$) and a helical polarization field $\vec{p}$ [2], which serves as the

primary order parameter of the N_{TB} phase – i.e., $\vec{p}$ vanishes in the higher temperature nematic phase and becomes non-zero in the N_{TB} phase.

In this chapter, we provide essential details about the experimental setup and procedures used to measure properties of the fluctuation modes in the N_{TB} phase, describe our key experimental results, and detail the Landau-de Gennes modeland the coarse-graining process developed to explain our results.

3.2 CHEMICAL STRUCTURES OF STUDIED MATERIALS

DLS measurements were performed on a 70/30% mixture (by weight) of the liquid crystalline dimer, 1,5-Bis(2′,3′-difluoro-4″-pentyl-[1,1′:4′,1″-terphenyl]-4-yl)nonane (abbreviated DTC5C9), and the monomer, 2′,3′-difluoro-4,4″-dipentyl-*p*-terphenyl (abbreviated MCT5). The chemical structures of these compounds are shown in Figure 3-1. The monomer and dimer were synthesized following the procedures reported in [7], and supplied to us by Prof. Georg Mehl of the Chemistry department, University of Hull, UK. The pure dimer exhibits both N and N_{TB} phases; the N_{TB} phase does not occur in the pure monomer. The 70/30 (dimer/monomer) mixture was used because the N – N_{TB} transition is lowered to a more convenient temperature for our experimental apparatus than in the pure dimer. The heliconical structure of the N_{TB} phase in the 70/30 mixture was previously confirmed by freeze fracture transmission electron microscopy (FFTEM) conducted by the Lavrentovich group at KSU [7]. They determined a typical value of the helical pitch to be $\sim 9\, nm$ and cone angle of $\sim 17^{\circ}$. (See schematic of the heliconical structure in Figure 1-6 for definitions of the pitch and cone angle).

Phase characterization of the 70/30 mixture was performed using polarizing optical microscopy (POM), while cooling a sample at a rate of 0.1°/min. The temperature was controlled with an Instec HCS402 hot stage and mK2000 temperature controller with a temperature stability of $0.01\,°\mathrm{C}$. This mixture has the phase sequence isotropic→ (uniaxial) nematic N → N_{TB} → crystal, with N–I transition temperature T_{NI} = 150.4 °C and N–N_{TB} transition temperature T_{TB} = 94.2 °C (both measured with a calibrated platinum resistance thermometer in our light-scattering oven). The N_{TB} phase in the 70/30 mixture has been characterized by a variety of techniques [7]; for our purposes, its choice afforded the possibility to obtain high-quality alignment of the average director ($\hat{n}_0$) in either homogeneous/planar or homeotropic configurations—i.e., $\hat{n}_0$ parallel or normal to the plane of the optical substrates, respectively—using thin (5 μm) cells with appropriate surface treatments.

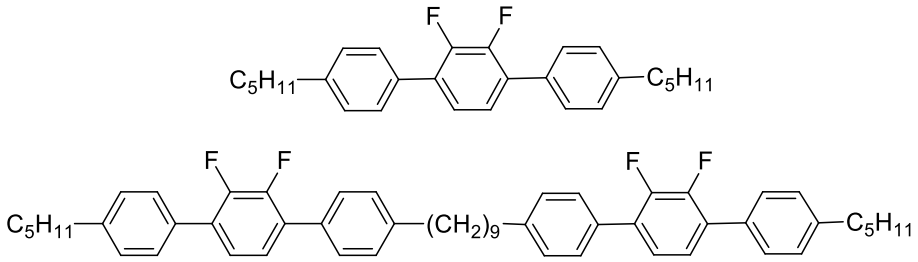

Figure 3-1: Chemical structure of the monomer (top) and dimer (bottom) compounds utilized for the present study. The 70/30 wt% mixture exhibits a N-N_{TB} phase transition at 94.2 °C.

Planar alignment was prepared by spin-coating a thin layer of polyimide (HD Microsystems, PI2555) on the optical glass substrates. By rubbing the substrate with a

velvet cloth, uniform orientation of the polyimide was achieved. The cells were assembled with anti-parallel orientation of the rubbing direction on the substrates.

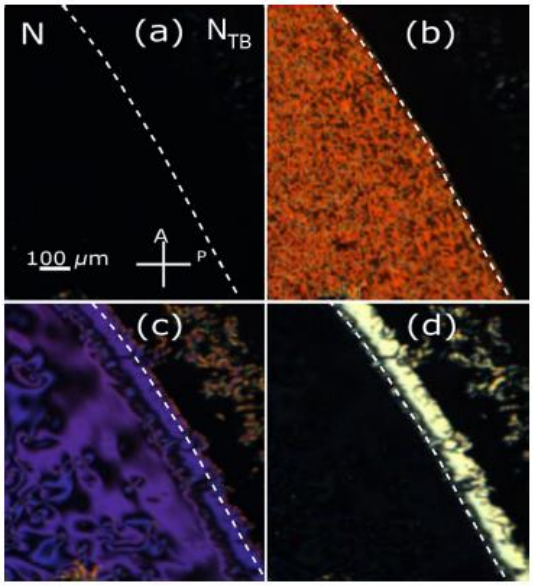

Figure 3-2 [8]: Polarizing microscope textures for a 5-μm-thick homeotropically aligned sample of the studied mixture. The optic axis is normal to the image plane, and the sample is placed between crossed polarizers. (a) Separate regions of N and N_{TB} phases observed at the transition between the two; the boundary is marked by the dashed line. Both regions are uniform and dark, indicating high-quality homeotropic alignment of the director $\hat{n}$ in the nematic and pitch axis $\hat{t}$ in the N_{TB} phase. (b) Under an applied ac voltage (5 V @ 10 KHz), a second-order Freedericsz transition (reorientation of $\hat{n}$ in the center of the sample) is observed in the nematic region, while the N_{TB} region is unchanged. (c) Under higher voltage (7 V @ 10 KHz), the N_{TB} region undergoes a first-order reorientation of $\hat{t}$ in the form of nucleating toroidal focal conic domains (FCDs) and expanding stripes of splay and saddle-splay deformations of $\hat{t}$. (d) Several seconds after the voltage has been switched off, the nematic region relaxes back to the homeotropic state, whereas the N_{TB} region relaxes considerably slower.

Homeotropic alignment was achieved by depositing an inorganic passivation layer (Nissan Chemical Industries, Ltd, NHC AT720-A) on the inner surfaces of each substrate.

In both cases, the cell gap was set using Micropearl glass spacers, which were mixed with NOA 71 UV cured glue deposited on the opposite inner edges of the substrates. The gap was measured using a Perkin Elmer UV/VIS Spectrometer Lambda 18. All the experimental cells were filled by capillary action in the isotropic phase.

Figure 3-2 shows the texture of the homeotropically-aligned sample observed in a polarizing optical microscope. The nematic phase texture observed between crossed polarizers remains uniformly dark as the sample is rotated in the plane of the polarizers, as it should be, if $\hat{n}_0$ is aligned perpendicular to the substrates and to the polarizer plane. In the N_{TB} phase, the texture remains dark, indicating the material remains optically uniaxial with average helical axis of the N_{TB} helicone perpendicular to the substrates.r

3.3 EXPERIMENTAL LIGHT SCATTERING GEOMETRIES

Our DLS measurements utilized two depolarized scattering geometries – G1 and G2 – which are depicted in Figure 3-3 and Figure 3-4 (Depolarized means that the analyzer placed in the scattered field is crossed with respect to the incident field polarization.) Time correlation functions of the depolarized scattered intensity of laser light were collected as a function of scattering vector $\vec{q}$ and temperature *T* in these geometries.

3.3.1 GEOMETRY G1

In geometry G1 (Fig. 3.3), the average liquid crystal director $\hat{n}_0$ is homogeneously aligned parallel to the substrate plane and perpendicular to the scattering plane (plane containing the incident and scattered light wavevectors, $\vec{k}_i$ and $\vec{k}_f$, respectively). The

incident light polarization $\hat{\imath}$ and wavevector $\vec{k}_i$ are, respectively, parallel and perpendicular to $\hat{n}_0$. The scattered wave vector $\vec{k}_f$ and polarization $\hat{f}$ are both perpendicular to $\hat{n}_0$. θ is the scattering angle measured in the lab. Explicit expressions obtained in sec 2.4.4 that connect these parameters are summarized below:

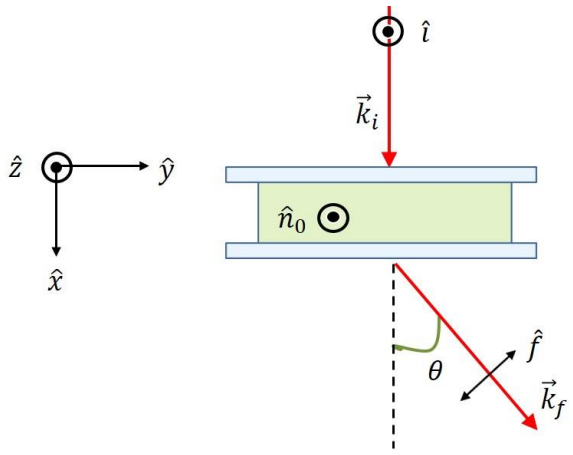

Figure 3-3: Light scattering geometry G1.

$$\hat{n}_0 \parallel \hat{z}$$

$$\hat{\imath} \parallel \hat{z}$$

$$\hat{f} = (-\sin\theta\,\hat{x} + \cos\theta\,\hat{y})$$

$$\vec{k}_i = \frac{2\pi}{\lambda} n_{\parallel} \hat{x}$$

$$\vec{k}_f = \frac{2\pi}{\lambda}\left[\sqrt{n_{\perp}^2 - \sin^2\theta}\,\hat{x} + \sin\theta\,\hat{y}\right]$$

$$q_z = 0$$

$$q_{\perp} = \frac{2\pi}{\lambda}\left[(\sqrt{n_{\perp}^2 - \sin^2\theta} - n_{\parallel})\hat{x} - \sin\theta\,\hat{y}\right]$$

Here $q_\perp = \sqrt{q_x^2 + q_y^2}$, $n_\parallel$, $n_\perp$are the refractive indices of the liquid crystal for light polarized parallel and/or perpendicular to $\hat{n}_0$, respectively, and λ is the wavelength of the incident light in air.

From Eq. (2.34), the scattered intensity in the uniaxial nematic (N) phase is,

$$I_s \propto \frac{G_1}{K_{11}q_\perp^2 + K_{33}q_z^2} + \frac{G_2}{K_{22}q_\perp^2 + K_{33}q_z^2} \tag{3.1}$$

where the optical factors G_1 and G_2 are defined in Eqs. (2.35). From Eq. (3.1), we see that since $q_z = 0$ in geometry G1, the scattering comes from pure splay and pure twist fluctuations of the director, with corresponding relaxation rates

$$\Gamma_1^n = \frac{K_{11}q_\perp^2}{\eta_{splay}}\,, \qquad \Gamma_2^n = \frac{K_{22}q_\perp^2}{\eta_{twist}} \tag{3.2}$$

where η_{splay} and η_{twist} are effective viscosities given by Eqs. (2.25), when $q_z = 0$. In Eq. (3.2), the superscript "n" indicates a director mode (fluctuation in $\hat{n}$). For large θ, $G_1 \gg G_2$, and the detected scattering arises from nearly pure splay fluctuations.

3.3.2 GEOMETRY G2

In geometry G2, the average director is perpendicular to the substrate plane (homeotropic alignment) and lies in the scattering plane. In this case, the optical factor $G_1 = 0$ and only scattering from the twist-bend director mode is detected, with relaxation rate

$$\Gamma_2^n = \frac{K_{22}q_\perp^2 + K_{33}q_z^2}{\eta_{twist-bend}} \tag{3.3}$$

where $\eta_{twist-bend} = \eta_2$ is given in Eq. (2.25). We set the incident of the light, θ_i, to either 15° or 35° off of normal incidence on the sample, and we varied the scattering angle between $\theta = -10°$ and 50°, with respect to $\hat{n}_0$, as shown in Fig. 3.4. When θ_s = 0°, the wavevector of the scattered light $\vec{k}_f$ lies along $\hat{n}_0$, and the scattering from director fluctuations is extinguished ("dark director" geometry). This choice of θ provides an opportunity to detect fluctuation modes that do not originate from $\hat{n}$ and contribute to the dielectric tensor in their own right.

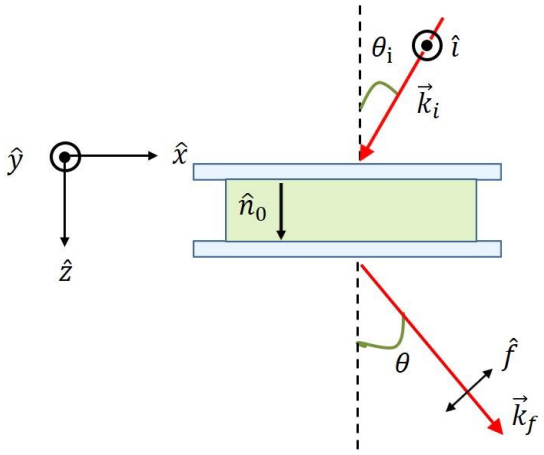

Figure 3-4: Light scattering geometry G2

We may summarize the main parameters and relations among them that apply for geometry G2 as:

$$\hat{n} \parallel \hat{z}$$

$$\hat{\imath} \parallel \hat{y}$$

$$\hat{f} = (-\cos\theta\,\hat{x} + \sin\theta\,\hat{z})$$

$$\vec{k}_i = \frac{2\pi}{\lambda}(-\sin\theta_i\,\hat{x} + \sqrt{n_\perp^2 - \sin^2\theta_i}\,\hat{z})$$

$$\vec{k}_f = \frac{2\pi}{\lambda}(\sin\theta\,\hat{x} + \sqrt{n_e^2 - \sin^2\theta}\,\hat{z})$$

$$q_z = \frac{2\pi}{\lambda}\left[\sqrt{n_e^2 - \sin^2\theta} - \sqrt{n_\perp^2 - \sin^2\theta_i}\right]$$

$$q_\perp = \frac{2\pi}{\lambda}[\sin\theta + \sin\theta_i]$$

Where $n_e^2 = n_\perp^2 + \left(1 - {n_\perp^2}/{n_\parallel^2}\right)\sin^2\theta$

3.4 DLS RESULTS FOR DIFFERENT GEOMETRIES

3.4.1 RESULTS FOR GEOMETRY G1

Figure 3-5 displays representative normalized time correlation functions of the scattered light intensity recorded in the nematic and twist-bend phases of a 4.2-μm-thick sample of the 70/30 mixture in geometry G1. For normal incidence and at large scattering angles, a single overdamped fluctuation mode is detected in both N and N_{TB} phases. As pointed out above, for large θ, the optical factor for splay is much larger than that for twist ($G_1 \gg G_2$), and so the observed mode corresponds to essentially pure splay fluctuations.

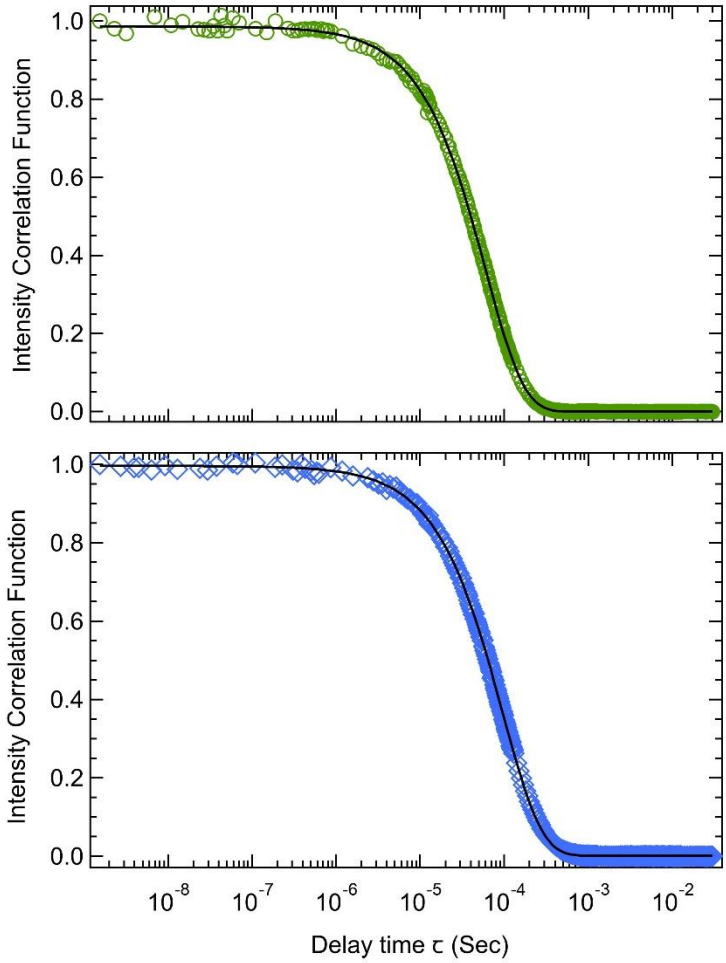

Figure 3-5: Top panel: Normalized time correlation DLS correlation functions of the scattered light intensity taken in the nematic phase of the studied 70/30 mixture for geometry G1 with $(T - T_{TB} = +6\ ℃)$ and scattering angle $\theta = 60°$. Bottom panel: Normalized correlation data taken in the N_{TB} phase for geometry G1 with $(T - T_{TB} = -1.1\ ℃)$ and $\theta = 60°$.

Fig. 3.6 shows the relaxation rate $\Gamma_1^n = \frac{K_1 q_1^2}{\eta_{splay}}$ of the splay fluctuations of the director (superscript *n* for director) plotted versus $q_\perp^2$ (the square of the scattering vector in geometry G1). The values of $q_\perp$ were obtained using the expression given above in section

3.3.1 and in the approximation $\sin^2\theta \ll n_\perp^2 \approx 2.3$, which gives $q_\perp^2 = (2\pi/\lambda)^2[(n_\perp - n_\parallel)^2 + \sin^2\theta]$. The data correspond to values of θ in 10˚ increments over the range 10˚ – 60˚. For the refractive index anisotropy $n_\parallel - n_\perp$, we used measured values from ref.[7] . The solid lines are fits to the expected hydrodynamic q dependence, $\Gamma_1^n \propto q^2$.

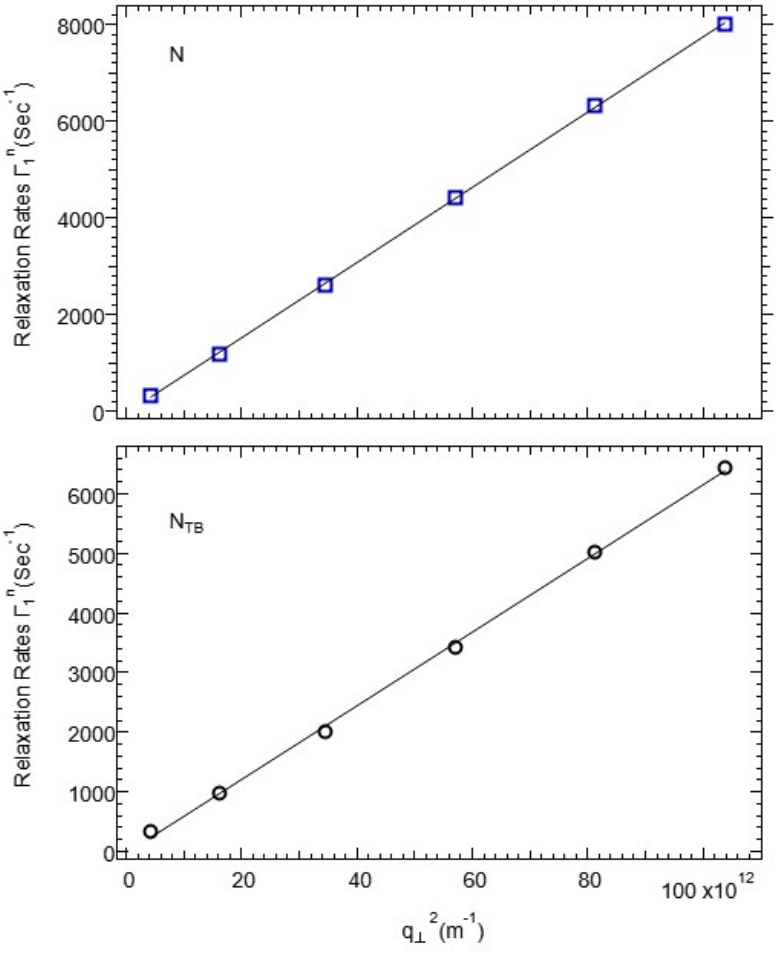

Figure 3-6**:** Dependence of the relaxation rate Γ_1^n of the director mode detected in geometry G1 on the square magnitude of the scattering vector $q_\perp^2$. Top panel: Nematic phase with $T - T_{TB} = +6$℃. Bottom panel: Twist bend nematic phase with $T - T_{TB} = -1.1$℃.

We observe that splay fluctuations of $\hat{n}$ have similar relaxation rates and q dependence on both sides of the N–N_{TB} transition, and therefore that the heliconical modulation of $\hat{n}$ in the N_{TB} phase does not significantly alter the character of the splay fluctuations. As we will discuss later, this fact is a reflection of the very short (~10 nm) pitch of the helicone, which allows one to develop a "coarse-grained" theory of the dynamics appropriate for experiments done at much longer optical (> 500 nm) length scales.

3.4.2 RESULTS FOR GEOMETRY G2

The spectrum and behavior of fluctuation modes detected in geometry G2 are more interesting. Let us first consider the nematic (N) phase. Above the N–N_{TB} transition, two overdamped modes are observed in the range of q studied: the expected twist-bend director mode with relaxation rate $\Gamma_2^n = \frac{K_{22}q_\perp^2 + K_{33}q_z^2}{\eta_{twist-bend}}$ on the order of $\sim 10^3\ s^{-1}$, and a faster mode with $\Gamma_2^p = 10^5\ s^{-1}$. (The meaning of superscript p will be clarified in the next section.) The relaxation rates Γ_2^n, Γ_2^p were extracted from fits of the measured time correlation function of the scattered intensity to the sum of two separate exponential decays of the scattered field correlation function $\langle \vec{E}_s^*(\vec{q}, 0)\, \vec{E}_s(\vec{q}, \tau)\rangle$ as a function of delay time τ. Representative examples of data and fits are shown in Fig. 3.7 (top panel).

The presence of the fast mode in the DLS correlation function is most evident in the "dark director" geometry where the scattering angle $\theta = 0°$ [see data labeled (b) in the top panel of Figure 3-7], although it contributes weakly for $\theta \neq 0°$. In the "dark" geometry where

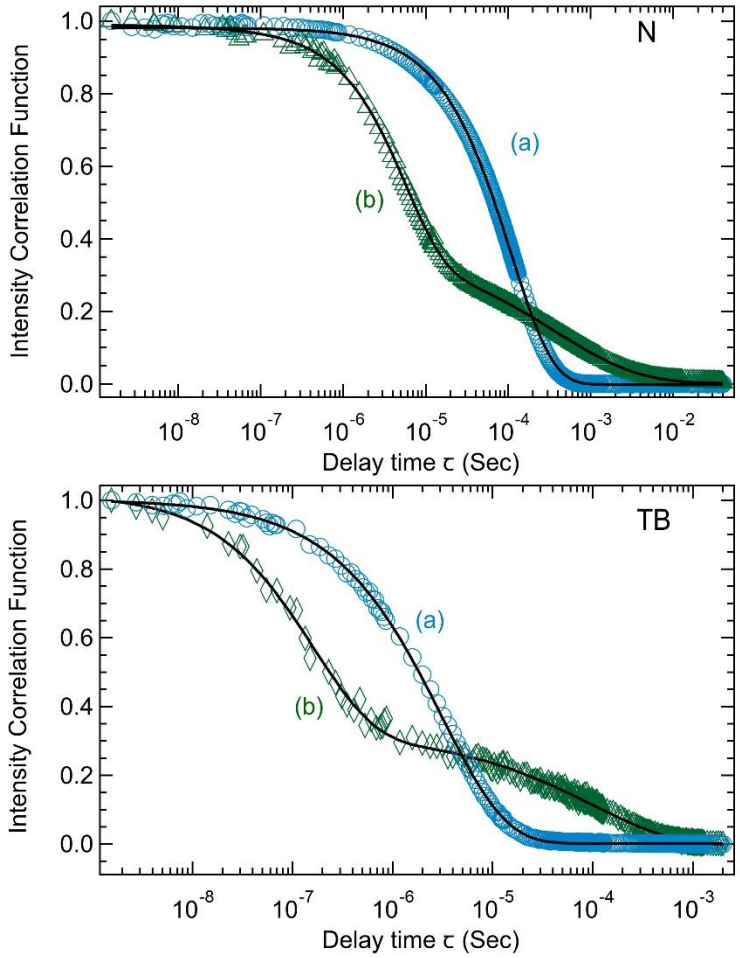

Figure 3-7: Top panel: Normalized time correlation functions of the scattered light intensity taken in the nematic phase of the 70/30 mixture for (a) geometry G2 with **(**$T - T_{TB} = 16.2℃$) and angles $\theta_i = 15^{\circ}$, $\theta = 40^{\circ}$(b) G2 with $T - T_{TB} = 16.2℃$ and $\theta_i = 15^{\circ}$, $\theta = 0^{\circ}$ ("dark" director geometry). Solid lines represent fits to double exponential decay, in (b), the slower component stretched. Bottom panel: Normalized correlation data taken in the N_{TB} phase for (a) geometry G2 with $T - T_{TB} = -0.93℃$ and $\theta_i = 15^{\circ}$, $\theta = 40^{\circ}$, (b) G2 with $T - T_{TB} = -2.5℃$ and $\theta_i = 35^{\circ}$, $\theta = 0^{\circ}$ (dark director geometry). Solid lines are single exponential fits, for (a) and double exponential in (b).

fluctuations in $\hat{n}$ are not expected to contribute to the light scattering, we still observe the decay of the slow director mode with a significant spread in its relaxation rate. (The fit in

this case used a stretched exponential, with one additional fitting parameter.) A slight variation (or "mosaicity") in the alignment of the director would both broaden the wavenumber q of the fluctuations detected (causing a spread in Γ) and also account for the "leakage" of the slow director mode. Since the scattering intensity of the slower mode is intrinsically much greater than the faster mode, even a small mosaicity can produce significant contribution from the director mode in the "dark" geometry.

Figure 3-8 plots the observed relaxation rates Γ_2^n, Γ_2^p as a function of scattering wavenumber $q_\perp$. Since $q_\perp^2 \gg q_z^2$ in geometry G2, and since the bend elastic constant K_{33} in nematics that form the N_{TB} phase is typically several times smaller than the twist constant K_{22}, we expect $\Gamma_2^n = \frac{K_{22}q_\perp^2 + K_{33}q_z^2}{\eta_{twist-bend}} \approx \frac{K_{22}q_\perp^2}{\eta_{twist-bend}} \propto q_\perp^2$, which is consistent with the hydrodynamic nature $\Gamma \propto q^2$ of a director mode and with what we observe in Figure 3-8 in the nematic phase. On the other hand, relaxation rate Γ_2^p of the faster mode is independent of $q_\perp$ over the limited range it could be accurately measured; this is the signature of a non-hydrodynamic mode.

Next we turn to the N_{TB} phase, where the relaxation rates and q dependence of the modes observed in geometry G2 change significantly. The relaxation rate of the twist-bend director mode, which dominates the scattering for $\theta \neq 0°$, increases markedly below the transition to values in the $10^5 - 10^6\ s^{-1}$ range, and, as evidenced in Figure 3-8, becomes q-independent. Thus, below T_{TB}, the twist-bend mode crosses over from a hydrodynamic

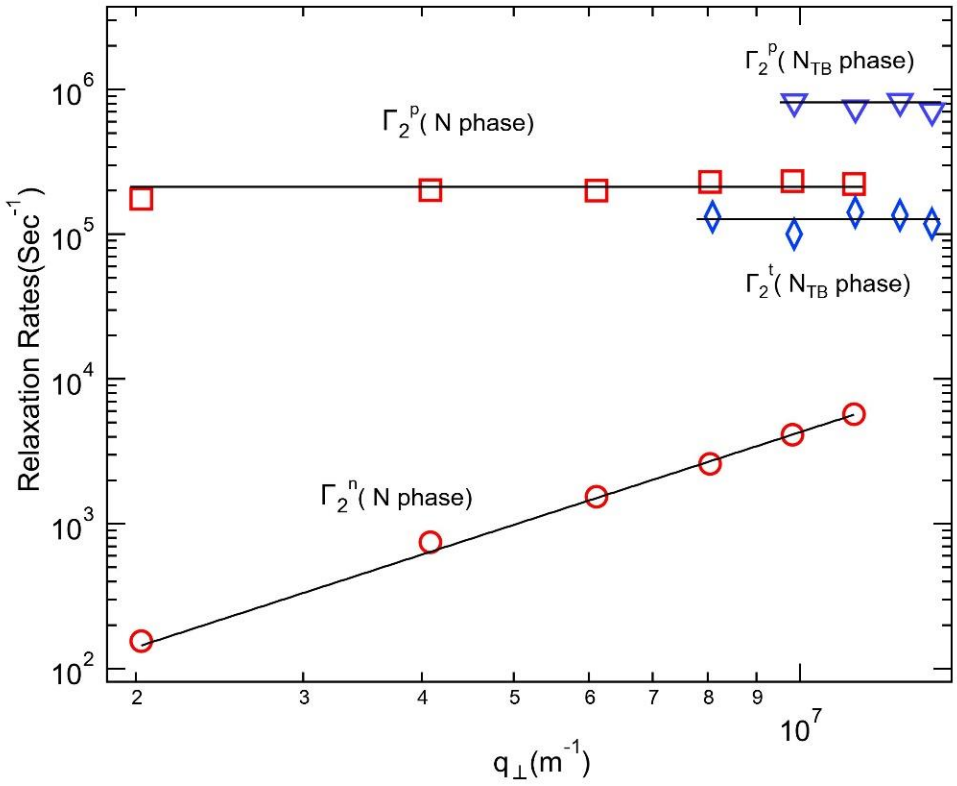

Figure 3-8: Dependence of the relaxation rates of the fluctuation modes detected in geometry G2 on scattering wavenumber $q_\perp$. Circles and squares correspond to relaxation rates $\Gamma_2^n$and Γ_2^p of the hydrodynamic director and nonhydrodynamic polarization modes detected in scattering geometry G2 in the middle of the nematic phase $T - T_{TB} = 25$℃. The scattering angle θ ranges from −5° to 45° for fixed incident angle $\theta_i = 15^\circ$. The slope of the line through the data on the log-log plot for Γ_2^n is 2, indicating $\Gamma_2^n \propto q^2$. Diamonds and triangles correspond to relaxation rate Γ_2^t of the nonhydrodynamic pitch axis fluctuations at temperatures ($T - T_{TB} = -0.85$℃ and -8℃) respectively, in the N_{TB} phase. These data are limited to higher q (or θ in the range 25° or 35° to 65°) due to a large component of background scattering at lower q, whose effect is exacerbated because of the low scattering intensity from fluctuations in the N_{TB} phase in the G2 geometry.

to a nonhydrodynamic mode. The effective director in the N_{TB} phase, which is the average of the heliconically-modulated director over one helical pitch, corresponds to the pitch axis,

which we shall designate by a unit vector $\hat{t}$. For clarity, we then label the relaxation rate of the twist-bend director mode below the transition to the N_{TB} phase as Γ_2^t (replacing Γ_2^n when $T < T_{TB}$).

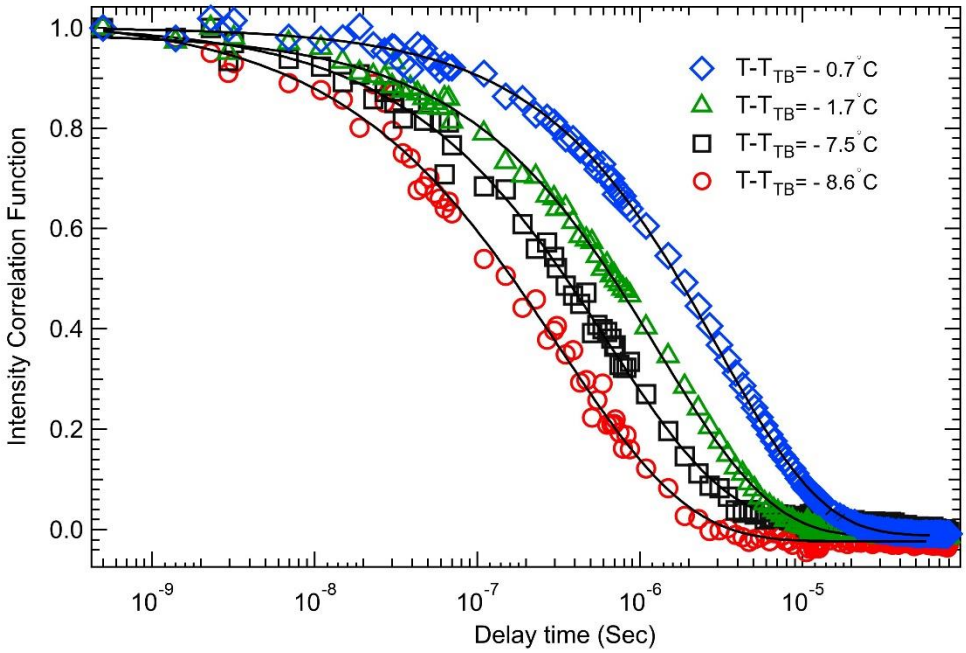

Figure 3-9 : Temperature dependency of correlation function of the scattered light intensity ($\boldsymbol{\Gamma_2^t}$) taken in the twist-bend phase of the 70/30 mixture for geometry G2 with $\boldsymbol{\theta_i = 15^\circ}$, $\boldsymbol{\theta = 40^\circ}$.

Correlation data taken in the "dark" director geometry in the N_{TB} phase reveal a second, even faster nonhydrodynamic mode with a relaxation rate of $10^6 - 10^7 s^{-1}$ (see data labeled (b) in the bottom panel of Figure 3-7). This is about 10 times higher than the values of Γ_2^p for the fast mode in the nematic phase detected in the same geometry. In addition, a much slower process, with relaxation rate much smaller than either Γ_2^p or Γ_2^t and comparable to that of a hydrodynamic director mode in the nematic phase, also contributes

to the correlation function in the "dark" geometry below the transition. This slow component is evidenced in the data labeled (b) in the bottom panel of Figure 3-7.

At fixed incident and scattering angles, we also recorded correlation data in the G2 geometry as a function of temperature, and fit these data to decaying exponentials in the delay time τ in order to extract the temperature dependence of the relaxation rates of the

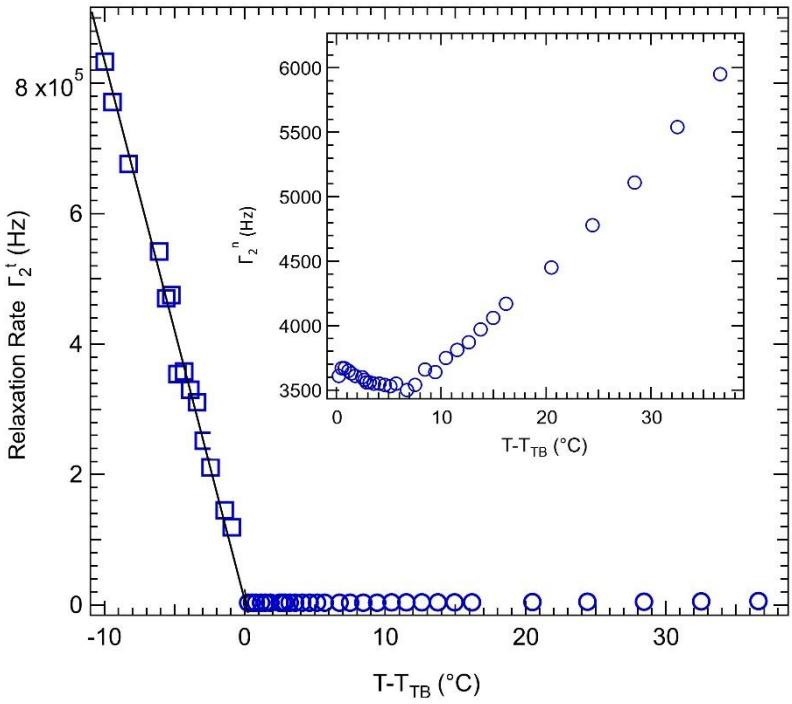

Figure 3-10 Temperature dependence of relaxation rates associated with director fluctuations detected in scattering geometry G2 in the uniaxial nematic phase (Γ_2^n for $T > T_{TB}$, circles in main figure and inset) and twist-bend phase (Γ_2^t for $T < T_{TB}$, squares in main figure) with fixed $\theta_i = 15^\circ$ and $\theta = 40^\circ$. The solid line is a fit of Γ_2^t to the linear temperature dependence predicted by the theoretical model discussed in sec. 3.5.4.

fluctuation modes. A sampling of this procedure is shown in Figure 3-9 for the fluctuations in the pitch axis $\hat{t}$ in the N_{TB} phase; the shift in the correlation data along the time axis indicates that the relaxation rate Γ_2^t is strongly temperature-dependent.

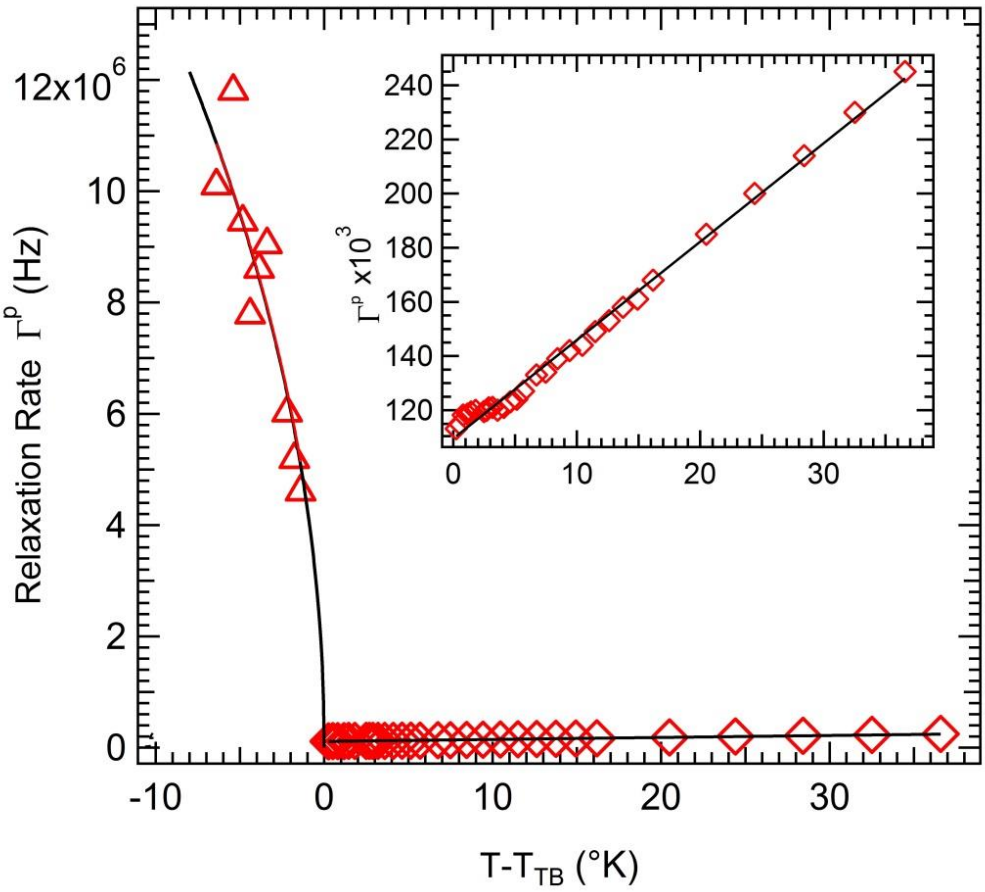

Figure 3-11: Temperature dependence of the relaxation rate of polarization fluctuations in the nematic (diamonds in main figure and inset for $\theta_i = 15^\circ$ and $\theta = 40^\circ$) and N_{TB} (triangles in main figure for $\theta_i = 35^\circ$, $\theta = 0^\circ$) phases. The solid lines in both panels are fits of Γ_2^p to calculated results from the theoretical model presented in sec.3.5.4.

Figure 3-10 presents the temperature dependence of the relaxation rates of the hydrodynamic director mode (Γ_2^n) in nematic phase and its nonhydrodynamic counterpart (Γ_2^t) in the N_{TB} phase.

In Figure 3-11 we display results for the temperature dependence of the relaxation rates of the fast nonhydrodynamic mode, Γ_2^p, in the N and N_{TB} phases. The nonhydrodynamic modes clearly slow down significantly as the temperature approaches T_{TB} from both sides of the transition, although on the low temperature side, our data are rather sparse and limited to temperatures more than 0.9 °C below the transition.

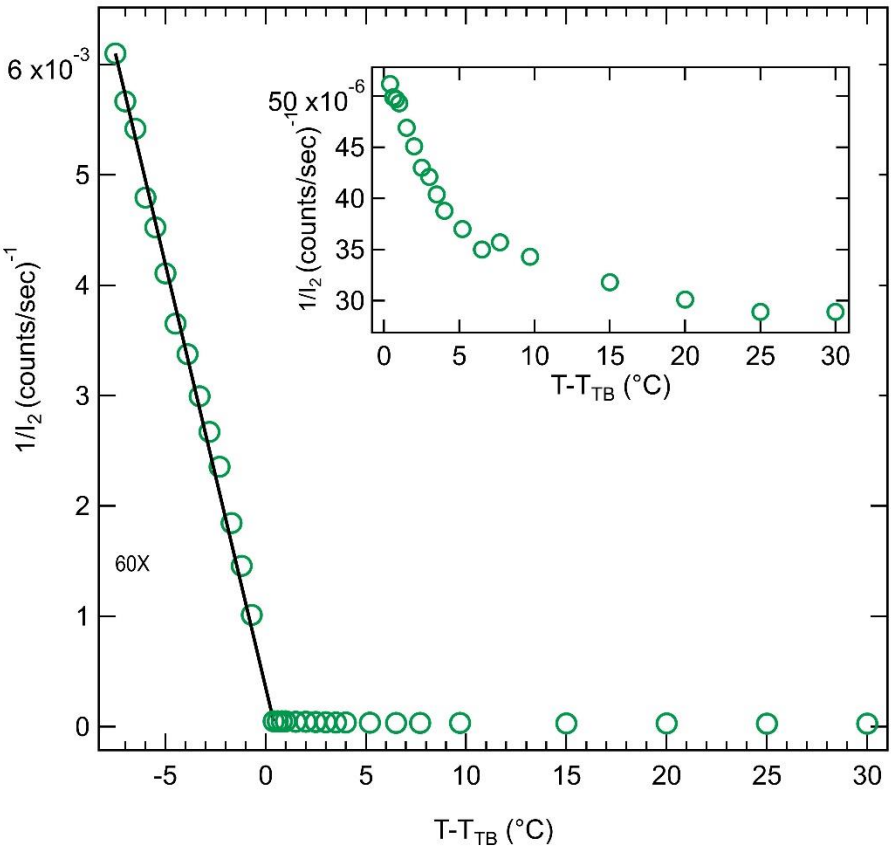

Figure 3-12: Temperature dependence of the inverse of the total scattering intensity ($\mathbf{I_2^{-1}}$)recorded in geometry G2 for $\boldsymbol{\theta_i = 15^\circ}$ and $\boldsymbol{\theta = 40^\circ}$. The solid line is a linear fit of the data for T < T_{TB} discussed further in sec. 3.5.4. The inset is a blow up of data in the nematic phase.

The reason for the sparsity of the data in the N_{TB} phase is twofold: First, the scattered intensity from the fluctuation modes is generally much lower in the N_{TB}, so obtaining high-quality correlation functions with good statistics was not always possible. Second, data for the faster nonhydrodynamic mode (Γ_2^p) were recorded in the "dark" director geometry, where the scattered intensity was generally even lower.

We also measured the intensity scattered from pitch axis ($\hat{t}$) fluctuations in the N_{TB} phase and the counterpart (twist-bend fluctuations of $\hat{n}$) in the N phase. Our results are reported in Figure 3-12. These data were taken at fixed $\theta_i = 15^{\circ}$, $\theta = 40^{\circ}$, well outside the "dark" geometry, where the dominant signal comes from director fluctuations. As $T \rightarrow T_{TB}$ from below, the decrease in the inverse scattered intensity from $\hat{t}$ fluctuations mirrors the decrease in their relaxation rate, Γ_2^t (Figure 3-10).

3.5 THEORETICAL MODEL AND COMPARISON TO EXPERIMENTAL RESULTS

Without developing a detailed theory, one could simply deduce the basic nature and number of modes we observe in the N_{TB} phase by exploiting the description of the N_{TB} phase as a "pseudo-layered" structure with the symmetry of a smectic-A phase. This picture, which is useful when the length scale probed experimentally is much greater than the heliconical pitch, predicts the following: one hydrodynamic mode that combines pseudo-layer bending and compression, one nonhydrodynamic mode that involves tilt of the average director relative to the pseudo-layer, and an additional nonhydrodynamic mode due to fluctuations in a polarization field (parallel to the pseudo-layers), which is coupled to director tilt. The polarization mode is based on two experimental results – the observation of an electroclinic effect (tilt induced polarization) in the N_{TB} phase [9] and optical evidence of left- and right-handed chiral domains of the heliconical structure [10].

We now proceed to analyze the fluctuation modes starting from a Landau-de Gennes expansion of the free-energy density in terms of the heliconical N_{TB} director and a helical polarization field. This approach was described in Shamid et al [2] and Parsouzi et al[8]. We let $\vec{P}$ represent a polarization field (vector order parameter of the N_{TB} phase) that originates, e.g., from the transverse dipole moment associated with the bent conformation of the dimer molecules, which promotes the formation of the N_{TB} phase. It is convenient to use a dimensionless form for this order parameter, $\vec{p} = \vec{P}/P_{sat}$, where P_{sat} corresponds to the saturated polarization at low temperatures. The free-energy density may be expanded in terms of the fields $\hat{n}$ and $\vec{p}$ as follows [2]:

$$F_{NTB} = \frac{K_{11}}{2}(\vec{\nabla}.\hat{n})^2 + \frac{K_{22}}{2}(\hat{n}.\vec{\nabla}\times\hat{n})^2 + \frac{K_{33}}{2}(\hat{n}\times\vec{\nabla}\times\hat{n})^2 + \frac{\mu}{2}|p|^2 \qquad (3.4)$$
$$+\frac{\nu}{4}|p|^4 + \frac{\kappa}{2}\left(\vec{\nabla}p\right)^2 - \Lambda[\left(\hat{n}\times\vec{\nabla}\times\hat{n}\right)^2].p + \eta(\hat{n}.p)^2$$

Here K_{11}, K_{22}, and K_{33} are the Frank elastic constants for splay, twist, and bend distortions of the director $\hat{n}$. The coefficient $\mu = \mu_0(T - T_0)$ is the temperature-dependent Landau coefficient for the polarization $\vec{p}$ (μ_0 being a constant), while $\upsilon > 0$ is a higher-order, temperature independent Landau coefficient. The elastic constant κ penalizes spatial distortions in $\vec{p}$, and the coefficient Λ couples $\vec{p}$ with bend distortions of $\hat{n}$. The last term, with $\eta > 0$, favors polarization perpendicular to the nematic director, which is consistent with the induced polarization reported in ref. [9]. Because $\vec{p}$ is defined to be dimensionless,

the Landau coefficients μ and ν carry the same units, and κ has the same units as the Frank constants.

In the N_{TB} phase, the director field has the heliconical modulation

$$\hat{n} = \hat{z}\cos\beta + \hat{x}\sin\beta\cos(q_0 z) + \hat{y}\sin\beta\sin(q_0 z) \tag{3.5}$$

with q_0 being the wavenumber of the modulation (assumed in the *z* direction), and β is the cone angle. (Note that $\sin\beta$ was called a in Ref. [2]) We assume the polarization field has the helical modulation

$$\vec{p} = \hat{x}p_0\sin(q_0 z) - \hat{y}p_0\cos(q_0 z) \tag{3.6}$$

with magnitude p_0, perpendicular to $\hat{n}$ and $\hat{z}$ [9], as shown in Figure 3-13 (left side). In the nematic phase, β and p_0 are both zero, while q_0 is undefined; in the N_{TB} phase, these quantities all become nonzero, and the pitch (spatial period) of the helicone is given by $t_0 = {}^{2\pi}/_{q_0}$. (We use t_0 for the pitch to avoid confusion with p_0, the magnitude of the polarization field $\vec{p}$.)

We proceed by inserting Eqs. (3.5) and (3.6) into Eq. (3.4) for F_{NTB}, and then minimizing with respect to q_0, β, and p_0 in order to obtain relations among these parameters in the ground state. For this calculation, we follow Ref. [2] and generalize it to the case of the weak polar elastic constant κ, which will turn out to be physically relevant.

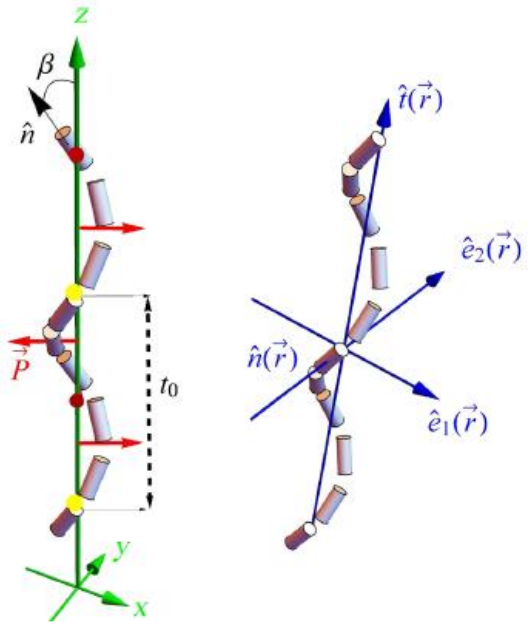

Figure 3-13: Left diagram: Schematic representation of the N_{TB} phase structure, showing heliconical director $\hat{n}$ (with cone angle β and helical pitch t_0) and helical polarization field $\vec{P}$. Right diagram: Frame of reference used to describe spatial variations of the average director or pitch axis, $\hat{t}$, on length scales much longer than the pitch. The orthogonal unit vectors $\hat{e}_1$and $\hat{e}_1$ form a right-handed system with $\hat{t}$. The xyz axes are fixed in the laboratory frame.

First, minimization with respect to q_0 gives

$$q_0 = \frac{\Lambda p_0 \sin\beta \cos\beta}{\kappa p_0^2 + K_{33} \sin^2\beta \cos^2\beta + K_{22} \sin^4\beta} \tag{3.7}$$

and minimization with respect to β gives

$$\sin^2\beta = -\frac{\kappa p_0^2}{K_{22}} + \sqrt{\frac{\kappa p_0^2}{K_{22}}\left(1 + \frac{\kappa p_0^2}{K_{22}}\right)} \tag{3.8}$$

Substituting Eqs. (3.7) and (3.8) into the free-energy density and expanding for small p_0 and κ gives

$$F_{NTB} = \frac{1}{2}\left[\mu_0(T - T_0) - \frac{\Lambda^2}{K_{33}}\right] p_0^2 + \frac{\Lambda^2 \kappa^{1/2} K_{22}^{1/2}}{K_{33}^2} |p_0|^3 + \frac{1}{4} \upsilon p_0^4 \tag{3.9}$$

From this form of the effective free-energy density, we can see that there is a second-order transition from the nematic to the N_{TB} phase at the temperature

$$T_{TB} = T_0 + \frac{\Lambda^2}{K_{33}\mu_0} \tag{3.10}$$

By minimizing the effective free energy (Eq. (3.9)), we find that p_0 depends on temperature as

$$p_0(T) = -\frac{3\Lambda^2 \kappa^{1/2} K_{22}^{1/2}}{2\upsilon K_{33}^2} + \sqrt{\frac{9\Lambda^4 \kappa K_{22}}{4\upsilon^2 K_{33}^4} + \frac{\mu_0(T_{TB} - T)}{\upsilon}} \tag{3.11}$$

As an aside, this theory can easily be modified to describe a first-order transition between the nematic and N_{TB} phases, by changing the fourth-order coefficient ν to a negative value and adding a sixth-order term to F_{NTB} in Eq. (3.4). We have not done so here because the DLS data give no indication of a first-order transition. However, such a modification might be useful for analyzing the nematic- N_{TB} transition in other systems. Now that we have determined the ground state, we consider fluctuations about the ground state in the nematic and N_{TB} phases.

3.5.1 FLUCTUATION MODES IN THE NEMATIC PHASE

In the nematic phase, we consider fluctuations in the director field about the ground state $\hat{n} = \hat{z}$ and fluctuations in the polarization about the ground state $\vec{p} = 0$. At lowest

order, these fluctuations can be described by $\delta\vec{n}(\vec{r}) = (n_x, n_y, 0)$ and $\delta\vec{p}(\vec{r}) = (p_x, p_y, p_z)$. We insert these expressions into the free energy F_{NTB} [Eq. (3.4)] and expand to quadratic order in the fluctuating components. We then Fourier transform from position $\vec{r}$ to wave vector $\vec{q}$, and express the free energy as a quadratic form in $n_x(\vec{q})$, $n_y(\vec{q})$, $p_x(\vec{q})$, $p_y(\vec{q})$ and $p_z(\vec{q})$. By diagonalizing this quadratic form, we obtain five normal modes:

(1) Two hydrodynamic modes are primarily associated with the splay-bend and twist-bend director modes (described in Chapter 2). Their relaxation rates are

$$\Gamma_1^n = \frac{K_{11}q_\perp^2 + K_{33}^{eff}q_z^2}{\eta_1} \tag{3.12}$$

$$\Gamma_2^n = \frac{K_{22}q_\perp^2 + K_{33}^{eff}q_z^2}{\eta_2} \tag{3.13}$$

where η_1, η_2 are the viscosities given in Eqs. (2.25)

$$K_{33}^{eff} = K_{33} - \frac{\Lambda^2}{\mu} = K_{33} - \frac{\Lambda^2}{\mu_0(T - T_0)} \tag{3.14}$$

is the renormalized bend elastic constant [2], which shows the effect of coupling the director to the polarization. This effect accounts for the softening of bend fluctuations observed in earlier light scattering studies of the director modes when $T \rightarrow T_{TB}$ from the nematic side [1]. Specifically, Eqs. (3.10) and (3.14) imply $K_{33}^{eff} = 0$ at $T = T_{TB}$.

(2) Two nonhydrodynamic modes are associated mainly with polarization fluctuations, p_x and p_y. In the limit $q \rightarrow 0$, these modes have the same relaxation rate:

$$\Gamma_2^p = \frac{\mu}{\eta_p} = \frac{\mu_0(T - T_0)}{\eta_p} \tag{3.15}$$

Here we use the subscript "2" to emphasize that this mode was only studied in scattering geometry G2 (see Figs. 3.7 and 3.8).

(3) Another nonhydrodynamic mode is polarization p_z by itself. In the limit of $q \to 0$, it has relaxation rate

$$\Gamma^{p'} = \frac{2\eta + \mu}{\eta_{p'}} = \frac{2\eta + \mu_0(T - T_0)}{\eta_{p'}} \tag{3.16}$$

In the above expressions, η_p and $\eta_{p'}$ are effective viscosities for the polarization modes.

3.5.2 COMPARISON OF THEORY TO EXPERIMENTAL RESULTS FOR THE NEMATIC PHASE

The fluctuating part of the dielectric tensor can be expressed in terms of the normal modes using the relation

$$\epsilon_{ij}(r) = \Delta\epsilon^n n_i n_j + \Delta\epsilon_{sat}^p p_i p_j \tag{3.17}$$

where$(i, j) = (x, y, z)$, $\Delta\epsilon^n$ is the dielectric anisotropy associated with the orientational ordering of $\hat{n}$, and $\Delta\epsilon_{sat}^p$ is the saturated value of the dielectric anisotropy associated with the $\vec{p}$ ordering.

In geometry G1, with incident and scattered light polarizations given by $\hat{\imath} = \hat{z}$ and $\hat{f} \perp \hat{z}$ and with $q_z = 0$, it can be shown that the fluctuations in $\hat{n}$ and $\vec{p}$ decouple. The former yield the usual pair of hydrodynamic director modes, while the latter produce a

doubly degenerate nonhydrodynamic mode associated with fluctuations in p_x and p_y plus an independent nonhydrodynamic mode associated with p_z. Assuming large coefficient η in Eq. (3.4), we can neglect p_z. Since the incident polarization in geometry G1 is along $\hat{z}$, the relevant elements of ϵ_{ij} for depolarized scattering are ϵ_{zx} and ϵ_{zy}. Assuming negligible p_z, these elements are dominated by the director modes, and specifically, in our experiment for large θ, by splay fluctuations. Therefore, in agreement with our experimental results for geometry G1, the model with large η predicts that the light scattering correlation function is described by a single exponential decay, with relaxation rate $\Gamma_1^n = K_{11}q_\perp^2/\eta_{splay}$, and that the contribution from nonhydrodynamic polarization fluctuations is not observable.

The situation is different in geometry G2, where $\vec{q} = q_x\hat{x} + q_z\hat{z}$ for scattering in the $x-z$ plane. In depolarized DLS, with the incident light polarized along $\hat{y}$, we probe fluctuations ϵ_{zy} and ϵ_{xy}. According to the theoretical model, the latter (ϵ_{xy}) couples to nonhydrodynamic polarization fluctuations transverse to the nematic ordering axis, which contribute maximally to the light scattering signal in the "dark director" limit of G2, where $\epsilon_{zy} \to 0$ and ϵ_{xy} dominates. Well outside the dark director geometry, ϵ_{zy} dominates, and this component picks out scattering from the hydrodynamic twist-bend director mode. Thus, for scattering angles $\theta \approx 0$ (close to the "dark director" geometry), both modes contribute, and the model predicts that the light scattering correlation function should be a double exponential decay, as observed in our experimental data in Figure 3-7 (b) in top

panel. The predicted behavior of the relaxation rates with q – namely, Γ_2^P independent of q for the nonhydrodynamic $\vec{p}$ fluctuations and $\Gamma_2^n \sim q^2$ for the hydrodynamic twist-bend director mode – is also confirmed by our experimental data for the q dependences of these modes in Figure 3-8.

Finally, we may compare our experimental results for the temperature dependence of the relaxation rate Γ_2^P in the nematic phase (Figure 3-11) to the theoretical prediction in Eq. (3.15). Combining this expression with Eq. (3.10), we get

$$\Gamma_2^p(T > T_{TB}) = \frac{\Lambda^2}{K_{33}\eta_p} + \frac{\mu_0}{\eta_p}(T - T_{TB}) \tag{3.18}$$

The fit of this expression to the data in Figure 3-11, shown as a solid line, yields $\frac{\mu_0}{\eta_p} = 3600\ s^{-1}K^{-1}$ and $\frac{\Lambda^2}{K_3\eta_p} = 1.1 \times 10^5 s^{-1}$, and thus $\frac{\Lambda^2}{K_3\mu_0} = 30\ K$. The fit describes the data well, indicating that the viscosity for polarization fluctuations, η_p, is (at most) weakly temperature dependent.

3.5.3 FLUCTUATION MODES IN THE TWIST-BEND NEMATIC PHASE

In the N_{TB} phase, the analysis of normal modes is complicated because of the nonuniform, modulated director structure. However, we can simplify this calculation through a "coarse-graining" approximation, which averages over the director modulation to find the larger-scale properties of the phase. Such coarse-graining has previously been done for the cholesteric phase [3][4], and it shows that the cholesteric has the same

macroscopic elastic properties as a smectic phase. In this section, we generalize the coarse-graining procedure to the more complex case of the N_{TB} phase.

The basic concept of the coarse-graining procedure is illustrated in Figure 3-13. We suppose that the director field has a rapid heliconical modulation with respect to a local orthonormal reference frame ($\hat{e}_1(\vec{r})$, $\hat{e}_2(\vec{r})$, $\hat{t}(\vec{r})$) and that this orthonormal frame varies slowly in space. Furthermore, the heliconical modulation might be displaced upward or downward by a phase $\varphi(\vec{r})$, which also varies slowly in space. Hence, the director field can be written as

$$\hat{n} = \hat{t}(\vec{r})\ \cos\beta + \hat{e}_1(\vec{r})\sin\beta\cos(q_0 z + \varphi(\vec{r})) + \hat{e}_2(\vec{r})\sin\beta\sin(q_0 z + \varphi(\vec{r})) \tag{3.19}$$

In this expression, $\hat{t}(\vec{r})$ is the "coarse-grained" director, which would be measured in any experiment that averages over the nanoscale heliconical modulation. By analogy with the director field, the polarization field has a rapid helical modulation with respect to the same local orthonormal reference frame, which can be written as

$$\vec{p} = \hat{e}_1(\vec{r})p_0\sin(q_0 z + \varphi(\vec{r})) - \hat{e}_2(\vec{r})p_0\cos(q_0 z + \varphi(\vec{r})) + \delta\vec{p}(\vec{r}) \tag{3.20}$$

Here $\delta\vec{p}(\vec{r}) = \delta p_x\hat{x} + \delta p_y\hat{y} + \delta p_z\hat{z}$ is an additional fluctuating contribution to the polarization, which varies slowly in space. It is allowed because $\vec{p}$ is not restricted to be a unit vector. The contribution $\delta\vec{p}(\vec{r})$ is the coarse-grained polarization, which would be measured in any experiment that averages over the nanoscale helical modulation.

We now consider the case of a well-aligned sample, as in a light-scattering experiment. In this case, the coarse-grained director $\hat{t}(\vec{r})$ has small fluctuations about $\hat{z}$,

while the phase $\varphi(\vec{r})$ and coarse-grained polarization $\delta\vec{p}(\vec{r})$ have small fluctuations around 0. The orthonormal basis can then be written as

$$\hat{e}_1(\vec{r}) = \left(1 - \tfrac{1}{2}t_x^2\right)\hat{x} - \tfrac{1}{2}t_x t_y \hat{y} - t_x \hat{z}\,, \tag{3.21}$$

$$\hat{e}_2(\vec{r}) = -\tfrac{1}{2}t_x t_y \hat{x} + \left(1 - \tfrac{1}{2}t_y^2\right)\hat{y} - t_y \hat{z}$$

$$\hat{t}(\vec{r}) = t_x \hat{x} + t_y \hat{y} + \left(1 - \frac{1}{2}t_x^2 - \frac{1}{2}t_y^2\right)\hat{z}$$

to quadratic order in t_x, t_y.

We insert Eqs.(3.19) and (3.20) for the director and polarization fields, together with Eq. (3.21) for the orthonormal basis, into Eq. (3.4) for the free energy of the N_{TB} phase. We then make the coarse-graining approximation: We integrate over the rapid variations of $\cos q_0 z$ and $\sin q_0 z$, assuming that the slowly varying fields are constant over the length scale of the pitch. We thus obtain an effective free energy in terms of the six coarse-grained variables $\varphi(\vec{r})$, $t_x(\vec{r})$, $t_y(\vec{r})$, $\delta p_x(\vec{r})$, $\delta p_y(\vec{r})$, and $\delta p_z(\vec{r})$.

$$F = \frac{1}{2}\sum_q \begin{pmatrix} \varphi_q \\ t_{xq} \\ \delta p_{yq} \\ t_{yq} \\ \delta p_{xq} \\ \delta p_{zq} \end{pmatrix}^{\dagger} M(q) \begin{pmatrix} \varphi_q \\ t_{xq} \\ \delta p_{yq} \\ t_{yq} \\ \delta p_{xq} \\ \delta p_{zq} \end{pmatrix}$$

Here, $M(q)$ is a matrix of wave-vector-dependent coefficients, which must be diagonalized to find the normal modes. It is most convenient to understand the mode structure in the limit of $q \to 0$. In this limit, the matrix simplifies to the block-diagonal form

$$M(q=0)=\begin{pmatrix} 0 & 0 & 0 & 0 & 0 & 0 \\ 0 & m_{22} & m_{23} & 0 & 0 & 0 \\ 0 & m_{32} & m_{33} & 0 & 0 & 0 \\ 0 & 0 & 0 & m_{44} & m_{45} & 0 \\ 0 & 0 & 0 & m_{54} & m_{55} & 0 \\ 0 & 0 & 0 & 0 & 0 & m_{66} \end{pmatrix}$$

$$m_{22}=m_{44}=p_0 q_0 \Lambda \sin\beta+\frac{1}{2}(K_{11}+K_{22}-2K_{33})q_0^2 \sin^2\beta$$

$$m_{33}=m_{55}=\mu+2\upsilon p_0^2+\eta \sin^2\beta$$

$$m_{23}=m_{32}=-m_{45}=-m_{54}=-\frac{1}{2}q_0\Lambda \sin\beta$$

$$m_{66}=\mu+2\eta+\upsilon p_0^2-2\eta \sin^2\beta$$

We can now extract the following six normal modes:

(1) The phase φ is itself a normal mode. This mode is hydrodynamic, with zero energy (and zero relaxation rate) in the limit of $q \rightarrow 0$. It describes pseudo-layer displacements in the N_{TB} phase that are analogous to the layer displacement of a smectic-A phase, which costs no energy for uniform displacement, with the pitch axis (coarse-grained director $\hat{t}$) locked to the pseudo-layer normal. It is visualized in terms of motion of the pseudo-layers in Figure 3-14 (b), (d) and (e).

(2) Tilt of the coarse-grained director in the *x* direction, t_x, and polarization fluctuation in the *y* direction, δp_y, are coupled by the helicity of the N_{TB} phase. Together, they form a pair of normal modes, both of which are nonhydrodynamic, with nonzero energy (and nonzero relaxation rate) in the limit of $q \rightarrow 0$. In the limit of weak coupling, which is given by the criterion $m_{22}m_{33} \gg m_{23}^2$, their relaxation rates are

$$\Gamma_2^t = \frac{p_0 q_0 \Lambda \sin\beta + \frac{1}{2}(K_{11} + K_{22} - 2K_{33}) q_0^2 \sin^2\beta}{\eta_t} = \frac{p_0^2 \Lambda^2 (K_{11} + K_{22})}{2\eta_t K_{33}^2} \tag{3.22}$$

$$\Gamma_2^p = \frac{\mu + 2\upsilon p_0^2 + \eta \sin^2\beta}{\eta_p} \tag{3.23}$$

These two modes of the pseudo-layered N_{TB} phase are analogous to director tilt and polarization fluctuations in a chiral smectic-A phase. The tilt mode (Γ_2^t) is visualized in Figure 3-14 (c). We have used the subscript "2" to emphasize that the non-hydrodynamic modes were studied in the scattering geometry G2 (see Figs. 3.7 – 3.9).

(3) The coarse-grained director tilt t_y and polarization δp_x form another pair of nonhydrodynamic normal modes, which is degenerate with the previous pair and has the same relaxation rates.

(4) The polarization component δp_z is itself a nonhydrodynamic normal mode. Its relaxation rate is

$$\Gamma^{p'} = \frac{\mu + 2\eta + \upsilon p_0^2 - 2\eta \sin^2\beta}{\eta_{p'}} \tag{3.24}$$

where $\eta_{p'}$ is the viscosity associated with this mode.

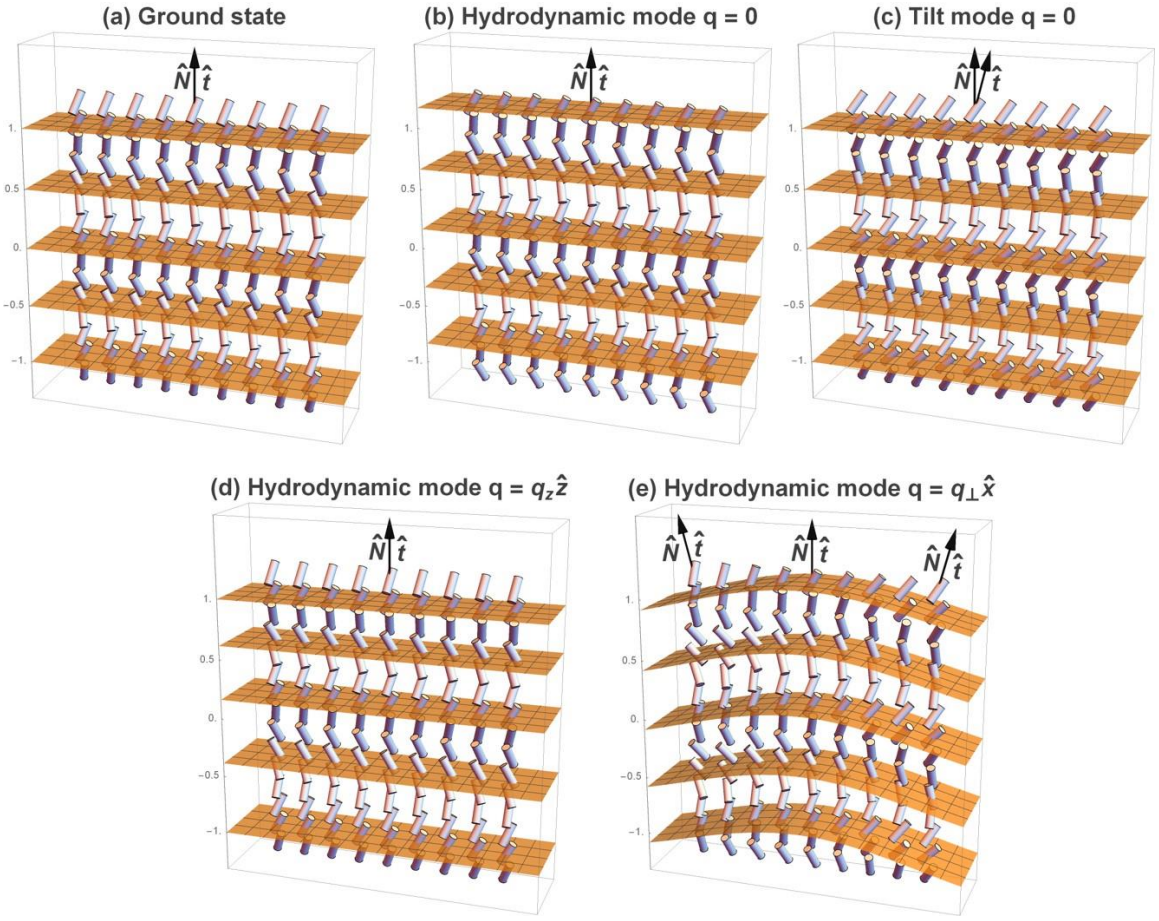

Figure 3-14: Visualization of certain fluctuation modes in the N_{TB} phase. Small cylinders represent the heliconical director field $\hat{n}(\vec{r})$, and surfaces represent the pseudolayers with layer normal $\hat{N}$. (a) Ground state. (b) Hydrodynamic mode with wave vector $\vec{q} = 0$, with uniform rotation of $\hat{n}(\vec{r})$ and hence uniform displacement of pseudo-layers; this mode has no energy cost with respect to the ground state. (c) Nonhydrodynamic tilt mode, with the coarse-grained director $\hat{t}$ [average of $\hat{n}(\vec{r})$] tilted with respect to pseudolayer normal. (d) Hydrodynamic mode with $\vec{q} = q\hat{z}$, with z-dependent rotation of $\hat{n}(\vec{r})$ and z-dependent displacement of pseudo-layers (leading to compression and dilation). (e) Hydrodynamic mode with $\vec{q} = q\hat{x}$, with x-dependent rotation of $\hat{n}(\vec{r})$ and x-dependent displacement of pseudo-layers (leading to curvature), accompanied by tilt so that $\hat{t}$ remains normal to pseudo-layers.(with permission from Prof. J. V. Selinger)

3.5.4 COMPARISON OF THEORY TO EXPERIMENTAL RESULTS FOR THE TWIST-BEND PHASE

In the N_{TB} phase, fluctuations of the dielectric tensor are described by Eq. (3.17), with the contribution of ordinary nematic director fluctuations, $\Delta\epsilon^n n_i n_j$, replaced by the contribution $\Delta\epsilon^t t_i t_j$ containing the components of the "coarse-grained" director (i.e., pitch axis) $\hat{t}$. In geometry G1, the hydrodynamic mode is the extension into the N_{TB} phase of the splay fluctuations detected in the N phase. When $q_z = 0$, this mode corresponds to a pure splay of $\hat{t}$ and a concomitant undulation of the planes of constant phase of the helicone; it has an elastic restoring torque is proportional to $K_{11}q_\perp^2$. We therefore expect essentially the same scattered intensity and relaxation rate for this mode as for simple splay fluctuations in the N phase, as our experimental results in Figure 3-5, Figure 3-6 (bottom panels) indeed confirm. The next Chapter will focus further on the behavior of this mode in the N_{TB} phase.

The "slower" non-hydrodynamic mode of the N_{TB} phase involves primarily fluctuations of $\hat{t}$ off the direction normal to the planes of equal phase, and has a relaxation rate Γ_2^t given by Eq. (3.22). This mode is the extension of twist-bend director mode of the N phase observed in geometry G2. It acquires a large "energy gap" –due to the large energy cost of tilting the director away from layer normal – when the heliconical structure forms below T_{TB}. Experimentally, we observed strong scattering from this mode in geometry G2 for scattering angles θ off the "dark director" condition ($\theta = 0$), which is exactly what is expected from the theoretical model when the "coarse-grained" director $\hat{t}$ replaces the usual nematic director $\hat{n}$.

The "faster" nonhydrodynamic mode observed in the N_{TB} phase is only detected in the "dark director" limit of geometry G2 [see correlation data labeled (b) in the bottom panel of Figure 3-7], where scattering from fluctuations in $\hat{t}$ is minimized. As it has the same conditions for observability, we may associate this mode with the expected extension of the non-hydrodynamic fluctuations ($\delta p_x, \delta p_y$) in the polarization field that we detected in the N phase (and labeled with relaxation rate Γ_2^p). Over the limited range in q where we could accurately record it (Figure 3-8), we can confirm that the polarization mode in the N_{TB} phase has the non-hydrodynamic character predicted by the theoretical model.

Another interesting feature of our experimental data, which is also explained by the model, is the appearance of a slow relaxation process that mixes with the fast polarization fluctuations in the "dark director" geometry in the N_{TB} phase, and has a relaxation rate comparable to ordinary nematic director fluctuations. This mixing is evident in the data in Figure 3-7 (bottom panel). When both q_z and $q_\perp$ are nonzero, as is generally the case in the G2 geometry, the theory predicts that δp_x and δp_y mix with the slow hydrodynamic variable φ (the phase of the heliconical structure) and with $\hat{t}$, in a combination that corresponds to a simple splay of $\hat{t}$ and undulation of the planes of constant φ. This combination should have a relaxation rate similar to the hydrodynamic splay fluctuations observed in geometry G1 (and mentioned above), as is indeed the case experimentally.

The final nonhydrodynamic mode predicted by the theory, related to fluctuations in polarization along the pitch axis (δp_z), is not detected in our experiment. This implies that the δp_z mode has significantly higher relaxation rate than the ($\delta p_x, \delta p_y$) fluctuations

(and thus much weaker scattered intensity). Comparing Eqs. and (3.16) and (3.24), this suggests that the coefficient η in the model free energy of Eq. (3.4) is large relative to the coefficient μ_0.

Next, we compare the temperature dependence of the measured relaxation rates Γ_2^t, Γ_2^p (Figure 3-10 andFigure 3-11), and the inverse scattered intensity I_2^{-1} (Figure 3-12), to the theoretical predictions in the N_{TB} phase. Specifically, we combine Eqs. (3.22) for Γ_2^t and (3.11) for p_0 to obtain

$$\Gamma_2^t(T < T_{TB}) = \frac{\Lambda^2(K_{11}+K_{22})}{2K_{33}^2\eta_t}\left[A^2\left(2-2\sqrt{1+\frac{\mu_0}{\nu A^2}(T_{TB}-T)}\right) + \frac{\mu_0}{\nu}(T_{TB}-T)\right] \tag{3.25}$$

where $\mathbf{A} = \frac{\mathbf{3\Lambda^2\sqrt{\kappa K_{22}}}}{\mathbf{2\nu K_{33}^2}}$. Fitting our data Fig. 3.10 for $\mathbf{T < T_{TB}}$ to Eq. (3.25), we find that that the second term, which is linear in $\mathbf{T_{TB} - T}$, accurately describes the data; the solid line shown in the figure has slope $\mathbf{8.4 \times 10^4 s^{-1} K^{-1}}$ with the transition temperature T_{TB} fixed to 367.4 K. (T_{TB} was identified by an abrupt drop in the intensity scattered from nematic director mode 2.) Including the non-linear temperature dependence in the first term does not significantly improve the fit quality. This suggests that $\frac{\mu_0}{\nu}(\mathbf{T_{TB} - T}) \gg \mathbf{A^2}$ over the range of $\mathbf{T_{TB} - T} < \sim\mathbf{1}$°C where we acquired data. In the opposite limit, $\frac{\mu_0}{\nu}(\mathbf{T_{TB} - T}) \ll \mathbf{A^2}$, Eq. (3.25) gives $\mathbf{\Gamma_2^t \sim (T_{TB} - T)^2}$ to leading order, which clearly does not match the data. On a more qualitative level, the observed temperature dependence of $\mathbf{\Gamma_2^t}$ as $\mathbf{T \to T_{TB}}$

from below confirms the slowing down or "softening" of the non-hydrodynamic fluctuations in pitch axis expected from the theory.

To obtain a theoretical expression for the temperature dependence of $\boldsymbol{\Gamma_2^p}$, we combine Eqs. (3.23) for $\boldsymbol{\Gamma_2^p}$ and (3.8) for $\boldsymbol{\sin^2\beta}$, expand to linear order in $\mathbf{p_0}$, and then use Eq. (3.11) for $\mathbf{p_0}$ in the limit $\frac{\boldsymbol{\mu_0}}{\boldsymbol{\nu}}(\mathbf{T_{TB}}-\mathbf{T}) \gg \mathbf{A^2}$. This gives:

$$\Gamma_2^p(T<T_{TB}) = \frac{\Lambda^2}{K_{33}\eta_p} + \frac{\eta}{\eta_p}\sqrt{\frac{\kappa\mu_0(T_{TB}-T)}{K_{22}\nu}} + \frac{\mu_0}{\eta_p}(T_{TB}-T) \tag{3.26}$$

In fitting our data for Γ_2^p in the N_{TB} phase to Eq. (3.26), we fixed the ratios $\frac{\Lambda^2}{K_3\eta_p}$ and $\frac{\mu_0}{\eta_p}$ to the values $1.1\times10^5\ S^{-1}$ and $3600\ S^{-1}K^{-1}$ determined from the analysis of Γ_2^p in the nematic phase (section 3.5.2 above). The resulting one parameter fit produces the solid curve shown in Fig. 3.11, which indicates that the middle term in Eq. (3.26) – proportional to $\sqrt{T_{TB}-T}$ – dominates over the term linear in $T_{TB}-T$. This in turn implies a large ratio $\frac{\eta}{\mu_0}$, and therefore is consistent with the relaxation rate $\Gamma^{p'}$of longitudinal polarization fluctuations δp_z in Eqs. (3.16) and (3.24) being much larger than Γ_2^p for the transverse polarization fluctuations. Since the scattered intensity is inversely proportional to the relaxation rate), this result explains why fluctuations δp_z are not observed in our experiment. Although our data for Γ_2^p in Fig. 3.11 are sparse and rather noisy, the fitted curve gives a reasonable representation of their temperature dependence.

Lastly, let us consider our data for the inverse scattering intensity I_2^{-1} in Figure 3-12. These data were recorded in geometry G2 for $\theta_i = 15^\circ$, $\theta = 40^\circ$, where the scattering is dominated by fluctuations $\hat{n}$ or $\hat{t}$. The scattered light intensity is proportional to the amplitude of these fluctuations and inversely proportional to the restoring torque. The relaxation rate is proportional to the restoring torque. Thus, we expect $(I_2^t)^{-1} \propto \Gamma_2^t$ – i.e., the inverse intensity from fluctuations in $\hat{t}$ should exhibit the same linear dependence on temperature that the relaxation rate does. This is confirmed by the solid line through the data for the inverse scattered intensity in Figure 3-12.

3.6 SUMMARY

Our light scattering study of a twist-bend nematic liquid crystal demonstrates the presence of a pair of temperature dependent, nonhydrodynamic fluctuation modes connected to the N_{TB} structure. One of these modes is associated with twist-bend director fluctuations in the presence of a short pitch heliconical modulation of $\hat{n}$, while the other is accounted for by fluctuations in a vector order parameter that corresponds to a helical polarization field coupled to the director modulation. The behavior of both modes, as well as the presence of a single hydrodynamic mode in the N_{TB} phase (associated with splay fluctuations of the helical pitch axis), is comprehensively explained by a theoretical model based on two components: (1) a Landau-de Gennes free energy density, which is expanded in the director and polarization fields, and (2) a coarse-graining of this free energy –

averaging over one pitch of the heliconical N_{TB} structure – that is appropriate for light scattering experiments probing length scales much greater than the pitch.

In the next Chapter, we will focus more closely on the analogy that coarse-graining facilitates between the "pseudo-layered" N_{TB} phase and an ordinary layered smectic-A phase.

3.7 REFERENCES

[1] K. Adlem *et al.*, "Chemically induced twist-bend nematic liquid crystals , liquid crystal dimers , and negative elastic constants," vol. 022503, pp. 1–8, 2013.

[2] S. M. Shamid, S. Dhakal, and J. V Selinger, "Statistical mechanics of bend flexoelectricity and the twist-bend phase in bent-core liquid crystals," *Phys. Rev. E - Stat. Nonlinear, Soft Matter Phys.*, vol. 052503, no. May, pp. 1–11, 2013.

[3] T. C. Lubensky, "Hydrodynamics of cholesteric liquid crystals," *Phys. Rev. A*, vol. 6, no. 1, pp. 452–470, 1972.

[4] L. Radzihovsky and T. C. Lubensky, "Nonlinear smectic elasticity of helical state in cholesteric liquid crystals and helimagnets," *Phys. Rev. E - Stat. Nonlinear, Soft Matter Phys.*, vol. 83, no. 5, pp. 1–3, 2011.

[5] P. K. Challa *et al.*, "Twist-bend nematic liquid crystals in high magnetic fields," *Phys. Rev. E - Stat. Nonlinear, Soft Matter Phys.*, vol. 89, no. 6, pp. 1–5, 2014.

[6] S. M. Salili, C. Kim, S. Sprunt, J. T. Gleeson, O. Parri, and A. Jákli, "RSC Advances," *RSC Adv.*, vol. 4, no. November, pp. 57419–57423, 2014.

[7] V. Borshch *et al.*, "Nematic twist-bend phase with nanoscale modulation of

molecular orientation," *Nat. Commun.*, vol. 4, pp. 1–8, 2013.

[8] Z. Parsouzi *et al.*, "Fluctuation Modes of a Twist-Bend Nematic Liquid Crystal," vol. 021041, pp. 1–16, 2016.

[9] C. Meyer, G. R. Luckhurst, and I. Dozov, "Flexoelectrically Driven Electroclinic Effect in the Twist-Bend Nematic Phase of Achiral Molecules with Bent Shapes," *Phys. Rev. Lett.*, vol. 067801, no. August, pp. 1–5, 2013.

[10] D. Chen, J. H. Porada, J. B. Hooper, A. Klittnick, Y. Shen, and M. R. Tuchband, "Chiral heliconical ground state of nanoscale pitch in a nematic liquid crystal of achiral molecular dimers," *PNAS*, vol. 110, no. 40, 2013.

CHAPTER 4

LIGHT SCATTERING STUDY OF THE "PSEUDO- LAYER" COMPRESSION ELASTIC CONSTANT IN A TWIST-BEND LIQUID CRYSTAL

In this chapter, we report a dynamic light scattering study of the hydrodynamic fluctuation mode that combines "pseudo-layer" bending and compression in the twist-bend nematic phase of the 70/30 mixture of liquid crystalline dimer DTC5C9 and its monomeric building block MCT5. (See sec. 3.2 and Fig. 3.1 of the previous chapter for the chemical structure and phase sequence of this mixture.)

The "pseudo-layer" bending/compression mode is the extension of the nematic splay-bend director mode into the N_{TB} phase. We determine the value of the effective "pseudo-layer" compression modulus, B_{eff}, and compare it to the typical value in an ordinary smectic-A phase, where the layer structure is defined by a definite mass density wave. The wavevector dependence of the hydrodynamic mode and the temperature dependence of B_{eff} provide important tests of the "coarse-grained" approach to understanding the long wavelength fluctuation modes of the N_{TB} phase and of the underlying free-energy models on which the coarse-graining is based.

4.1 INTRODUCTION

As mentioned in Chapters 1 and 3, different "microscopic" theories have been put forth to explain the formation of the heliconical N_{TB} structure from a higher-temperature, uniform nematic state. We use the term "microscopic" liberally – i.e., to refer the modeling of a nanoscale heliconical structure and not to imply that microscopic interactions between individual molecules are being treated. One such theory is the "negative elasticity" model in which the nematic bend elastic constant becomes negative below the transition temperature[1-3], inducing a spontaneous bend that is stabilized by twist and by a positive higher-order elastic term. An alternative theory – the "polarization wave" model used to explain our results in Chapter 3 – introduces a vector order parameter[4-6] (polarization field) that becomes non-zero in the N_{TB} phase, and winds helically with the same nanoscale pitch as the molecular orientation to which it is coupled.

An alternative way to view the N_{TB} phase, which would be valid on length scales long compared to the pitch, is as a phase whose optical, electrical, and mechanical properties are qualitatively similar to those of a smectic-A LC or, perhaps more appropriately given the handedness of the heliconical domains, a chiral smectic-A [7]. In this picture, slabs of the N_{TB} phase with thickness equal to one pitch are treated as smectic "pseudo-layers" – one such slab is shown schematically in Fig. 4.1. One can then imagine a fluctuation of the pseudo-layers in which the layers bend in an undulatory fashion, and the unit normal to the pseudo-layers – or pitch axis $\hat{t}$ of the underlying heliconical configuration of the molecules – splays, as depicted in Fig. 4.2.

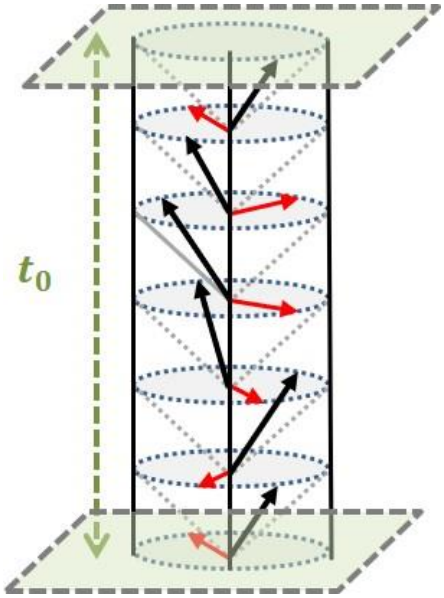

Figure 4-1: Schematic views of the heliconical molecular organization in the nematic twist bend (N_{TB}) phase. The dark arrows represent the orientation of the local molecular long axis (or heliconical director $\hat{n}$), which is nonpolar. Red arrows indicate a helically modulated polar vector ($\vec{p}$), which represents a shape or electric polarization arising from the bent conformation of a dimer that contains an odd-numbered CH_2 linkage between the two aromatic core groups. The indicated planes, separated by one pitch length (t_0), define a slab-like ‘‘pseudo-layer’’ that are associated with the heliconical structure.

The energy penalty for this fluctuation is controlled by two elastic constants: An effective layer bending, or splay in $\hat{t}$, constant, K_{eff}, which we may expect to be comparable to the splay constant K_{11} of the higher temperature N phase, and a layer compression modulus, B_{eff}, which is analogous to the compression constant of an ordinary smectic liquid crystal, but possibly of quite different magnitude. Coarse-graining analyses[7,8] of the ‘‘microscopic’’ Landau-deGennes models map them onto free energy densities with the same form as for a smectic-A phase, and give explicit expressions for

B_{eff} as a function of $T_{TB} - T$ in the N_{TB} phase that we shall discuss in later sections of this chapter.

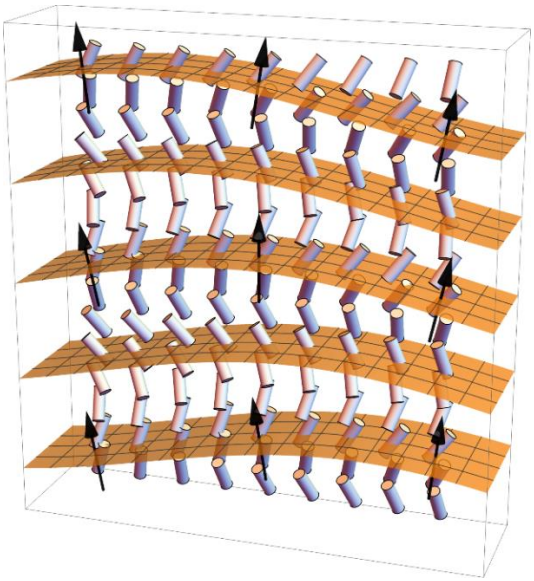

Figure 4-2: Simulation of the pseudo-layer bending/compression mode in the N_{TB} phase, when $q_\perp$ and q_z are both nonzero. The dark arrows represent the pseudo-layer normal (and average director $\hat{t}$) with permission from Prof. J.V. Selinger, Kent State University.

4.2 LIGHT SCATTERING GEOMETRY

In a smectic-A liquid crystal, the light scattered from hydrodynamic fluctuations involving bending/compression of the smectic layers has an intensity given by $I_1^n \propto \frac{(\Delta\varepsilon^n)^2 k_\beta T G_1}{K q_\perp^2 + B q_z^2/q_\perp^2}$, and these fluctuations relax at a rate $\Gamma_1^n = \frac{K q_\perp^2 + B q_z^2/q_\perp^2}{\eta}$ [9]. Here $\hat{z}$ is the average layer normal, B and K are elastic constants for layer compression and bending, respectively, η is a phenomenological viscosity for layer sliding, and the subscript 1 and scattering factor G_1 refer to nematic director mode 1 (splay-

bend), which evolves into the layer bending/compression mode below the nematic-smectic-A transition. Recall from Eqs. (2.24),(2,34) that the splay-bend mode in the nematic phase produces scattered intensity $I_1^n \propto \frac{(\Delta\varepsilon^n)^2 k_\beta T G_1}{K_{11}q_\perp^2 + K_{33}q_z^2}$ and has relaxation rate $\Gamma_1^{\mathrm{n}} = \frac{K_{11}q_\perp^2 + K_{33}\,q_z^2}{\eta_1}$, where η_1 is the viscosity given by Eq. (2.25). The superscript *n* indicates that the scattering comes from the director rotations.

By the analogy to a smectic-A described in sec. 4.1, we expect a pseudo-layer bending/compression mode with scattered intensity and relaxation rate given by,

$$I_1^t \propto \frac{(\Delta\varepsilon^t)^2 k_\beta T G_1}{K_{eff}q_\perp^2 + B_{eff}\,q_z^2/q_\perp^2} \qquad \Gamma_1^t = \frac{K_{eff}q_\perp^2 + B_{eff}\,q_z^2/q_\perp^2}{\eta_{eff}} \tag{4.1}$$

Here η_{eff} is a phenomenological viscosity associated with pseudo-layer sliding. Here the superscript *t* refers to the effective director $\hat{t}$ of the N_{TB} phase, which is the pitch axis of the heliconical structure. The relaxation rate Γ_1^t for hydrodynamic fluctuations in $\hat{t}$ that dominate the scattering in geometry G1 should not be confused with the rate Γ_2^t discussed in the previous chapter for scattering from geometry G2. The former applies to rotations of $\hat{t}$ that are locked to rotations of the planes of constant heliconical phase (i.e., to rotations of the pseudo-layers, Fig. 4.2), while the latter corresponds to rotations of $\hat{t}$ relative to the pseudo-layer planes.

To study the compression constant B_{eff} experimentally in the N_{TB} phase, we began by setting up the geometry G1 described in sec. 3.3.1, with average director ($\hat{z}$) perpendicular to the scattering plane, incident (scattered) light polarization normal

(parallel) to the scattering plane, and fixed incident angle $\theta_i = 0^\circ$ (normal incidence). Pure splay and pure twist contribute to the light scattering for arbitrary scattering angle θ. One can then choose a value of the scattering angle $\theta = \theta_m = sin^{-1}(n_o\sqrt{1 - n_o^2/n_e^2})$, where θ_m is the magic angle such that the scattering amplitude of director mode 2 vanishes (i.e., G_2= 0 in Eq. (3.1)) [10]. Since $q_z = 0$ in geometry G1, this choice of θ isolates pure splay fluctuations in the N phase and pure bending of the pseudo-layers in the N_{TB} phase. For the present work, we used available optical birefringence data [11] to estimate $\theta_m = 40^\circ$ at the N – N_{TB} transition. Rocking the average director by an angle χ off the normal to the scattering plane, as shown schematically in Fig. 4.3, then allows one to vary $q_z/q_\perp$ away from zero ($q_z = 0$ when $\chi = 0^\circ$), and thus to mix a component of pseudo-layer compression ($B_{eff}\, q_z^2/q_\perp^2$) into the scattering from pseudo-layer bending fluctuations ($K_{eff}q_\perp^2$), as described by Eq. (4.1).

From Fig. 4.3, we may obtain the following expressions for $q_\perp$ and q_z,

$$q_\perp = \frac{2\pi}{\lambda_0}[\left(n_e(\chi) - \sqrt{n_f^2 - \sin^2\theta}\right)^2 + \sin^2\theta\cos^2\chi]^{1/2} \tag{4.2}$$

$$q_z = \frac{2\pi}{\lambda_0}\sin\theta\sin\chi \tag{4.3}$$

where $\lambda_0 n_e(\chi) = n_\perp n_\parallel / \sqrt{n_\perp^2\cos^2\chi + n_\parallel^2\sin^2\chi}$ in Fig. 4.3, and n_f is the refractive index for the scattered wave given approximately by $n_f \approx n_\perp$ for small χ.

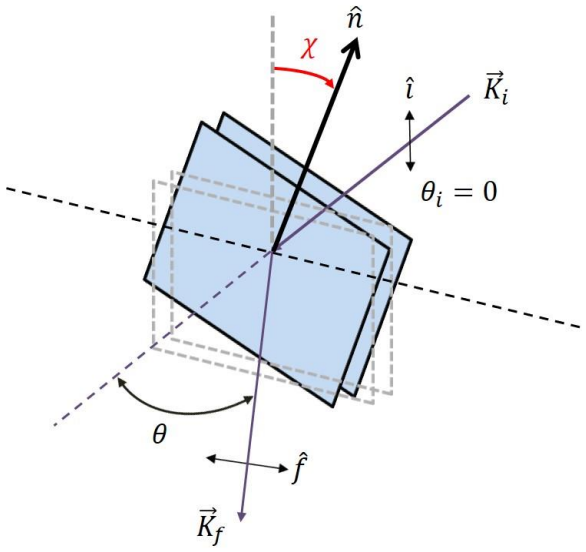

Figure 4-3: Light scattering geometry for the study of the pseudo-layer bending/compression mode in the N_{TB} phase, with the ‘‘rocking’’ angle χ indicated. The normally incident laser light (wavevector $\vec{k}_i$, incident angle θ_i) is polarized vertical to the scattering plane (and parallel to the average director $\hat{t}_0$ when $\chi = 0^\circ$). Horizontally-polarized scattered light (wavevector $\vec{k}_s$ is collected at angle θ). The fluctuation wavevector probed is $\vec{q} = \vec{k}_s - \vec{k}_i$.

Homogeneous planar-aligned nematic samples of the 70/30 mixture were prepared using commercial cells (EHC, Japan) with $4\,\mu m$ nominal spacing between flat optical substrates treated with rubbed polyimide alignment layers on their inner surfaces. The sample cells were placed in a microscope hot stage, temperature-regulated to $0.002\,℃$ precision and slightly modified for light scattering studies. The hot stage was mounted on a third circle on top of the two-circle scattering goniometer. The third circle, mounted vertically and with its rotation axis oriented horizontally, enabled the nematic director (or equilibrium pitch axis in the N_{TB} phase) to be continuously rotated (through angle χ)

between parallel and perpendicular orientations with respect to the scattering plane (Fig. 4.3). Separate x-y micro-positioning stages allowed the rotation axis of the third circle to be positioned precisely in coincidence with the normally-incident laser beam and to vary the position of the illuminated volume in the sample. A long-distance polarizing microscope was situated in the scattering plane and used to monitor both the sample texture and the precise position of the beam on the sample during the light scattering measurements.

4.3 RESULTS AND DISCUSSION

4.3.1 LIGHT SCATTERING CORRELATION FUNCTION

The intensity–intensity time correlation function was measured for various θ and χ using the correlator hardware described in sec. 2.5.5. Figure 4-4 displays representative, normalized light scattering correlation functions, taken at two values of angle χ (0° and 30°) for scattering angle $\theta_s = \theta_m = 40^\circ$ in the N_{TB} phase ($T - T_{TB} = -2.6℃$) of the70/30 mixture. The solid lines through the correlation data represent fits to a single exponential decay corresponding to the pseudo-layer bending/compression mode in the limit of a small compression component (i.e., for small q_z). In this limit, pseudo-layer bending and splay of the average director (pitch axis) predominate, and we expect and observe a relaxation rate ~10^3 s^{-1} similar to that for splay fluctuations in the nematic phase.

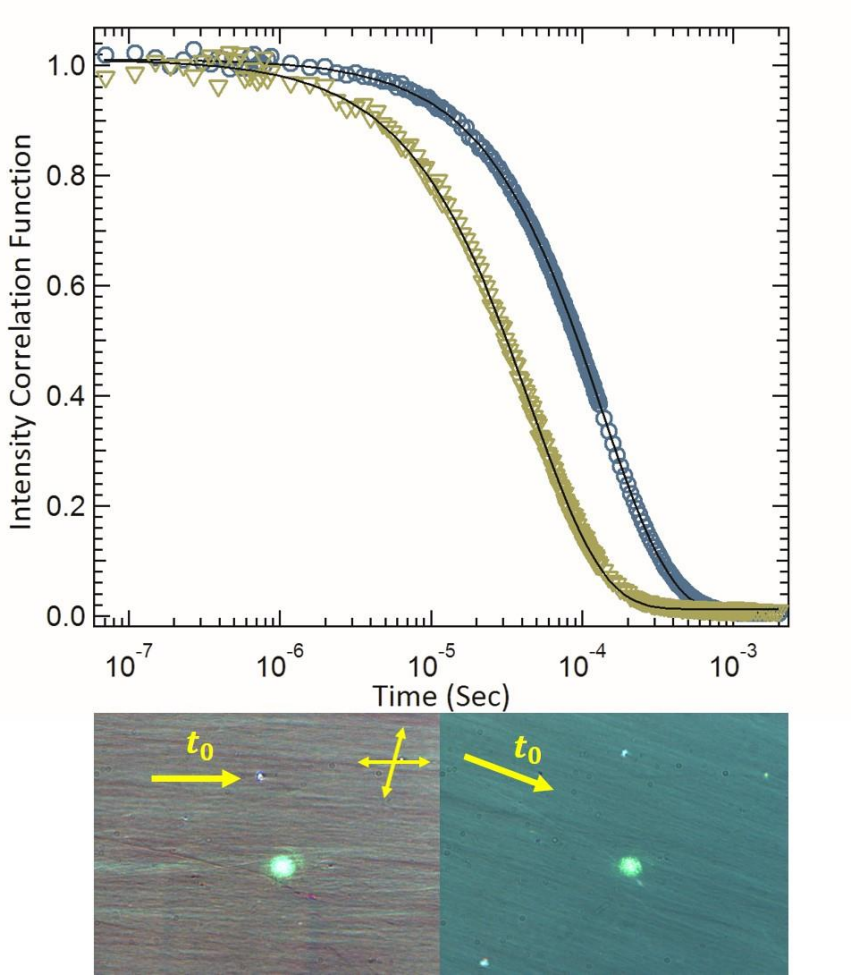

Figure 4-4: Top: Typical light scattering correlation functions obtained in the N_{TB} phase at $\mathbf{T - T_{TB} = -2.6}$℃ and for normal incidence, scattering angle $\boldsymbol{\theta = 40^{\circ}}$, and rocking angles $\boldsymbol{\chi = 0^{\circ}}$ (right plot) or $\mathbf{30^{\circ}}$ (left plot). Solid lines are fits to a slightly stretched single exponential decay. Bottom: Textures of the N_{TB} phase recorded by polarizing microscopy at $\mathbf{T - T_{TB} = -0.6}$℃ and for angle $\boldsymbol{\chi = 0^{\circ}}$ (left) and $\mathbf{16^{\circ}}$ (right). The position of the scattering volume is also recorded, allowing us to confirm no translation of the illuminated volume when the sample is rocked. The weak stripe texture visible for $\boldsymbol{\chi = 0^{\circ}}$ is probably due to pseudo-layer shrinkage at the cell surfaces; it caused no significant static scattering. (Yellow double arrows indicate the orientattions of polarizer and analyzer placed in the optical path on either side of the sample.)

Fig. 4.4 also displays examples of the sample texture and position of the illuminated volume in the sample for χ = 0° and 16°. A weak stripe texture is evident in the image for $\chi = 0^{\circ}$; this is most likely due to a slight pseudo-layer distortion or ‘‘buckling’’ near the cell surfaces. We carefully positioned the illuminated volume to minimize static light scattering from the stripes and to maintain the signal/background ratio of the correlation functions above 90%.

4.3.2 RELAXATION RATES VERSUS ROCKING ANGLE χ

Fig. 4.5 presents data for the relaxation rate Γ_1^n in the nematic phase, at temperature $T - T_{TB} = +1.9℃$ and scattering angle $\theta = \theta_m = 40^{\circ}$, as a function of rocking angle χ. Recalling that $K_{11} \gg K_{33}$ close to T_{TB} [11], we expect $\Gamma_1^n \approx K_{11} q_\perp^2 / \eta_1 \propto \cos^2 \chi / \eta_1$. The numerator in this expression predicts a decrease in Γ_1^n of ~25% with increasing χ over the range studied; however, our data show that Γ_1^n remains relatively flat. The reason for this discrepancy could be the $q_\perp$ dependence of the orientational viscosity η_1 (see Eq. (2.25)): As χ increases from zero, the orientational viscosity $\eta_1(\vec{q})$ begins to cross over from $\eta_{splay} = \gamma_1 - {\alpha_3^2}/{\eta_b}$ (when $q = q_\perp$) to $\eta_{bend} = \gamma_1 - {\alpha_2^2}/{\eta_c}$ (when $q_\perp = 0$). Since in typical nematics $\eta_{splay} \approx (4-5)\,\eta_{bend}$ [12] a decrease in the denominator of the expression for Γ_1^n with χ could cancel the decrease in the numerator, resulting in an essentially constant value as we observe in Figure 4-5.

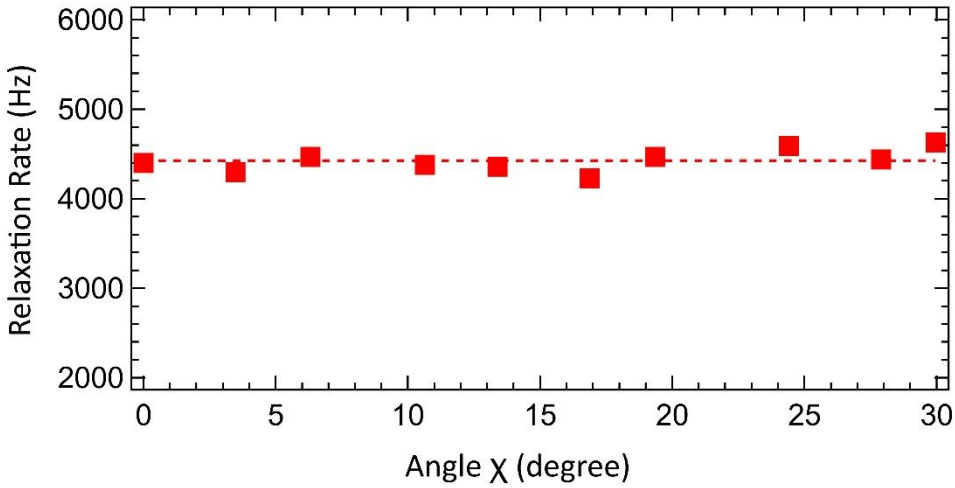

Figure 4-5: Dependence of the relaxation rate in the nematic phase on the rocking angle χ for a temperature $T - T_{TB} = 1.9$ ℃. The dashed line represents the average value.

Figure 4-6 presents the relaxation rate of the pseudo-layer bending/compression mode as a function of rocking angle χ for scattering angle $\theta = \theta_m = 40^{\circ}$, at two temperatures $T - T_{TB} = -1.4$ ℃ and -2.6 ℃ in the N_{TB} phase. The data clearly exhibit the behavior expected from Eq. (4.1); the relaxation rate increases with q_z, which depends on χ according to Eq.(4.3). The solid curves are fits of the data to the combination of Eq. (4.1) for Γ_1^t and Eqs. (4.2) and (4.3) for $q_\perp$ and q_z. The fit is constrained because the refractive index anisotropy for the 70/30 mixture has been determined as a function of temperature [11]. If we then take $n_\perp \approx 1.5$ (higher precision does not significantly affect the results of our analysis), and $\theta = 40^{\circ}$, there are just two adjustable parameters in our fit, namely B_{eff}/η_{eff} and K_{eff}/η_{eff}, whose ratio gives B_{eff}/K_{eff}.

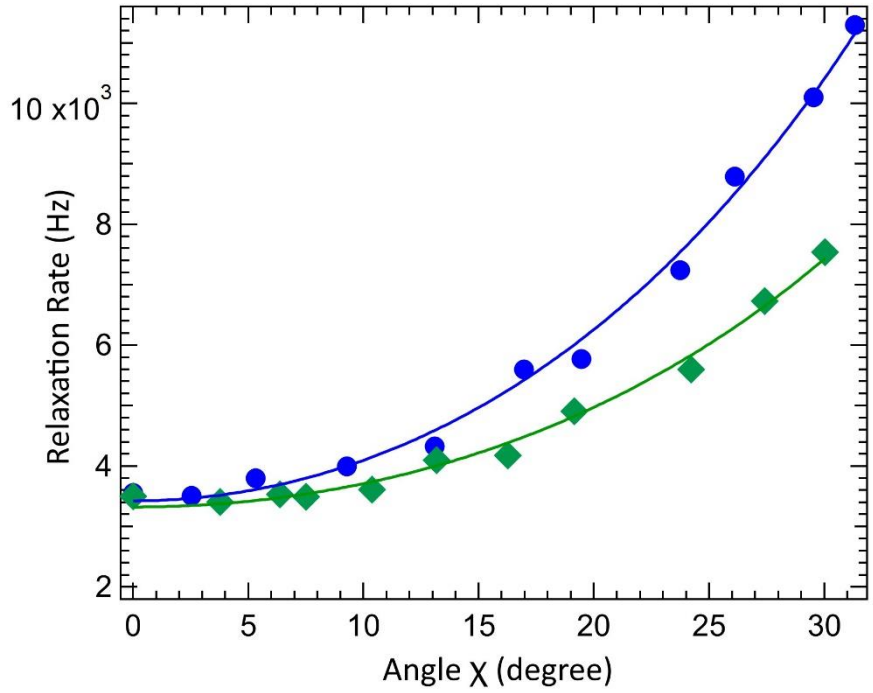

Figure 4-6: Dependence of the relaxation rate Γ_1^t of the pseudo-layer undulation mode on the rocking angle χ for two temperatures, $T - T_{TB} = -1.4$ ℃ (green diamonds) and -2.6 ℃ (blue circles), in the N_{TB} phase of studying sample, and for scattering angle $\theta = \theta_m = 40^{\circ}$. For χ between 0 and 30°, q_z spans from 0 to 3.9×10^6 m^{-1}, while $q_\perp$ ranges from. 7.6×10^6 to 6.5×10^6 m^{-1}. The solid lines are fits described in the text.

The fit yields $B_{eff}/K_{eff} = 3.9 \times 10^{14} m^{-2}$ and $B_{eff}/K_{eff} = 6.1 \times 10^{14} m^{-2}$ for $T - T_{TB} = -1.4$ ℃ and -2.6 ℃, respectively. Then we can obtain B_{eff} from an estimate of K_{eff}. In both a conventional smectic-A and by analogy in a "pseudo- layered" N_{TB} phase with small cone angle β, K_{eff} is comparable to the splay elastic constant K_{11} in the nematic phase. Taking the average K_{11}measured in the nematic phase[11], $K_{11} = 1.5 \times 10^{-11} N$, we find $B_{eff} = 5.9 \times 10^3\ Pa$ and $9.2 \times 10^3\ Pa$ at the two temperatures $T - T_{TB} =$

-1.4 ℃ and -2.6 ℃, These values would increase by a factor of $\simeq 2$, if we used the value of K_{11} just above the N–N_{TB} transition.

We can compare our experimentally deduced values for B_{eff} with the predictions of the coarse-grained "negative elasticity" and "polarization wave" theories of the N_{TB} phase discussed in refs. [7] and [8]. Both predict $B_{eff} \approx K_{33} q_0^2 \beta^2$, where the "microscopic" parameters are the cone angle and wavenumber of the heliconical N_{TB} structure. Then taking the previously measured value [11] $K_{33} = 2 \times 10^{-12} N$ (in the middle of the nematic phase of the 70/30 mixture), $\beta = 5.5^{\circ}$ (for $T - T_{TB} = -2$ ℃), and $q_0 = 2\pi/(9.3\, nm)$ for the 70/30 mixture in the N_{TB} phase[11], we get $B_{eff} \approx 8.4 \times 10^3\ Pa$, which falls in the same range as our experimental values.

The value of B_{eff} in the pseudo-layered N_{TB} phase is two to three orders of magnitude lower than typical values of the layer compression modulus, $B \approx 10^6 - 10^7\ Pa$, in a smectic-A phase. Thus, the "pseudo-layers" are much softer with respect to compression than are the smectic layers defined by a periodic variation in mass density.

4.3.3 RELAXATION RATE VERSUS SCATTERING ANGLE θ

Let us next turn to the dependence of relaxation rates Γ_1^n (nematic phase) and Γ_1^t (N_{TB} phase) on the scattering angle θ for fixed $\chi = 30^{\circ}$. Typical data in the nematic phase (at $T - T_{TB} = 4.5$ ℃) are displayed in Fig.4.7. Since $\Gamma_1^{\mathrm{n}} = \frac{K_{11} q_1^2 + K_{33}\, q_z^2}{\eta_1}$, we expect from Eqs. (4.2) and (4.3) that Γ_1^{n} should be linear $\sin^2\theta$, and the fit in Fig. 4.7 confirms this.

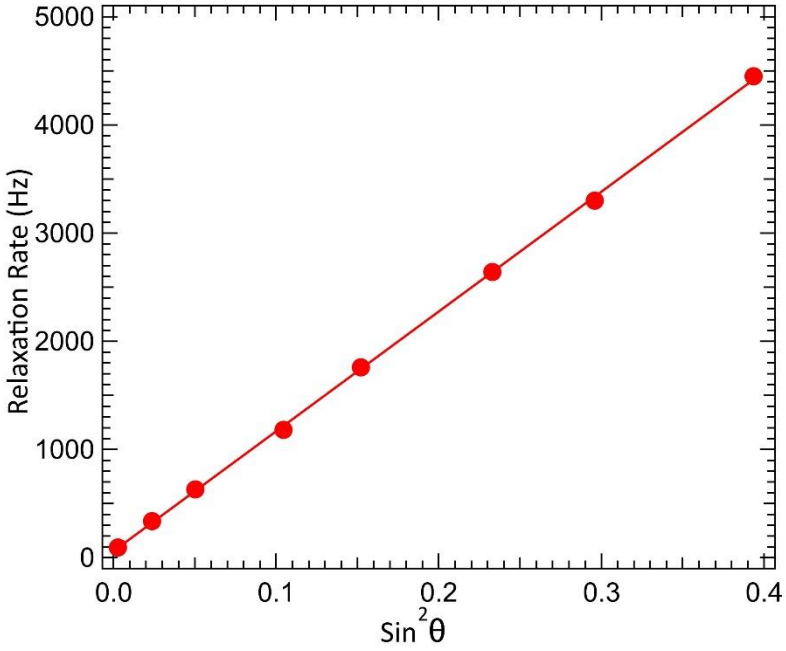

Figure 4-7: Relaxation rate Γ_1^n versus $\sin^2\theta$ for rocking angle $\chi = 30^\circ$ in the N phase ($T - T_{TB} = 4.5$ ℃). Over the range of the data points, q_z varies from 0.48×10^6 to 3.6×10^6 m^{-1} and $q_\perp$ from 1.2×10^6 to 6.3×10^6 m^{-1}.The solid line is a linear fit as described in the text.

In the N_{TB} phase, the dependence of Γ_1^t on $\sin^2\theta$ is expected to be nonlinear due to the $q_z^2/q_\perp^2$ term in Eq. (4.1). For small θ, Eqs. (4.2) and (4.3) give $q_z^2/q_\perp^2 \sim \sin^2\theta$, while at large θ, the ratio saturates at a value of $\tan^2\chi$. The behavior of the data for Γ_1^t presented in Figure 4-8 for $T - T_{TB} = -2.5$ ℃ are qualitatively consistent with this prediction. Quantitatively, we can fit the data to an expression for Γ_1^t obtained from the combination of Eqs. (4.1), (4.2)and (4.3).

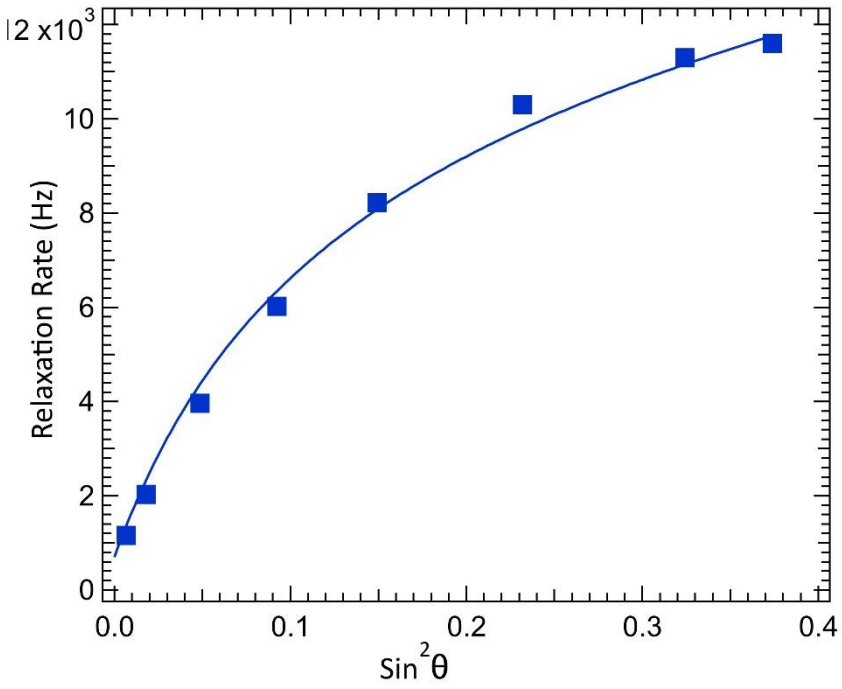

Figure 4-8: Relaxation rate Γ_1^t versus $\sin^2\theta$ for rocking angle $\chi = 30^\circ$ in the N_{TB} phase ($T - T_{TB} = -2.5$ ℃). Over the range of the data points, q_z varies from 0.48×10^6 to $3.6 \times 10^6\ m^{-1}$ and $q_\perp$ from 1.2×10^6 to $6.3 \times 10^6\ m^{-1}$.The solid line is a fit to Eq. (4.4)

We assume that the pseudo-layers are rigidly anchored at the substrate surfaces so that the minimum $q_\perp$ is cut off by the finite sample thickness, $q_{\perp,min} = \pi/d$ (d = sample thickness). We then replace the first term in square brackets in Eq.(4.2) with $q_{\perp,min}/(2\pi/\lambda_0) = \lambda_0^2/4d^2$, which imposes the cut-off. Then Eq.(4.1) for Γ_1^t becomes

$$\Gamma_1^{TB} = \frac{K_{eff} q_0^2}{\eta_{eff}} \left(\frac{B_{eff}}{K_{eff}} \frac{\sin^2\theta}{\lambda_0^2/4d^2 + 3/4\sin^2\theta]} + \frac{\lambda_0^2}{4d^2} + \frac{3}{4}\sin^2\theta \right) \tag{4.4}$$

where $q_0 = {}^{2\pi}/_{\lambda_0}$.

With B_{eff}/K_{eff} fixed to the value determined from the χ scan at $T - T_{TB} = -2.6℃$ – i.e., $B_{eff}/K_{eff} = 6.1 \times 10^{14} m^{-2}$ – the fit of the data for Γ_1^t in Fig. 4.8 to Eq. (4.4) becomes a one parameter fit. The result, shown as the solid blue line, represents the data well and strongly supports the ‘‘pseudo-layer’’ model of the N_{TB} phase, which leads directly to the θ dependence for Γ_1^t in Eq. (4.4).

4.3.4 TEMPERATURE DEPENDENCE OF THE PSEUDO-LAYER COMPRESSION MODULUS B_{eff}

Finally, we consider the temperature dependence of B_{eff}. In a coarse-graining analysis, the “polarization wave” model of the N–N_{TB} transition, which emphasizes the role of a helical polar order parameter [4], makes the following prediction [8]:

$$B_{eff} = \Lambda p_0 q_0 \sin\beta \cos\beta \approx \frac{\Lambda^2}{K_{33}} p_0^2 \tag{4.5}$$

Here Λ is the coupling between bend distortion of the director and the polar order parameter $\vec{p}$ (see Eq. (3.4)), K_{33} is the ‘‘bare’’ nematic bend elastic constant, β is the cone angle (assumed to be small), and the temperature dependence of $|\vec{p}| = p_0$ is given by Eq. (3.11),

$$p_0(T) = -\frac{3\Lambda^2 \kappa^{1/2} K_2^{1/2}}{2\upsilon K_3^2} + \sqrt{\frac{9\Lambda^4 \kappa K_2}{4\upsilon^2 K_3^4} + \frac{\mu_0 (T_{TB} - T)}{\upsilon}} \tag{4.6}$$

where μ_0 and υ are temperature-independent coefficients in the free energy density, Eq. (3.4). Eq.(4.5) assumes that β and p_0 do not change under small variations in pseudo-layer spacing (i.e., small variations in heliconical pitch). If they are allowed to vary in order to

further reduce the free energy, On the other hand, if β and p_0 are allowed to vary by small amounts in response to small variations in pseudo-layer spacing, the scaling of B_{eff} with p_0 changes to

$$B_{eff} \approx \frac{3\Lambda^2\sqrt{\kappa K_2}}{K_3^2} p_0^3 \tag{4.7}$$

which replaces Eq.(4.5).

To compare our experimental data to the two predictions for $B_{eff}(T)$, given by either Eq.(4.5) or (4.7) combined with (4.6), we consider the scattered light intensity from pseudo-layer bending/compression fluctuations. According to Eq.(4.1), the inverse scattered intensity from these fluctuations is,

$$(I_1^t)^{-1} \propto B_{eff}\, q_z^2/q_\perp^2 + K_{eff} q_\perp^2 \tag{4.8}$$

If we assume K_{eff} is (at most) only weakly temperature-dependent near T_{TB} – in fact, the theoretical models give $K_{eff} \simeq K_{11}$ (the "bare" director splay elastic constant in the N phase) [4], then the temperature-dependence of $(I_1^t)^{-1}$ is determined predominantly by B_{eff}.

The solid line in the bottom panel of Fig. 4.9 is a fit of our data for $(I_1^t)^{-1}$ to the prediction of the "polarization wave" model when the "microscopic" parameters β and p_0 are assumed to remain constant under pseudo-layer fluctuations. Specifically, we combine Eq.(4.8) with Eqs.(4.5) and (4.6) to produce a three parameter fit function for $(I_1^t)^{-1}$ vs *T*. The solid line in the top panel is a fit of the same data to the model when β and p_0 are allowed to relax under pseudo-layer fluctuations in order to reduce the free energy. In this

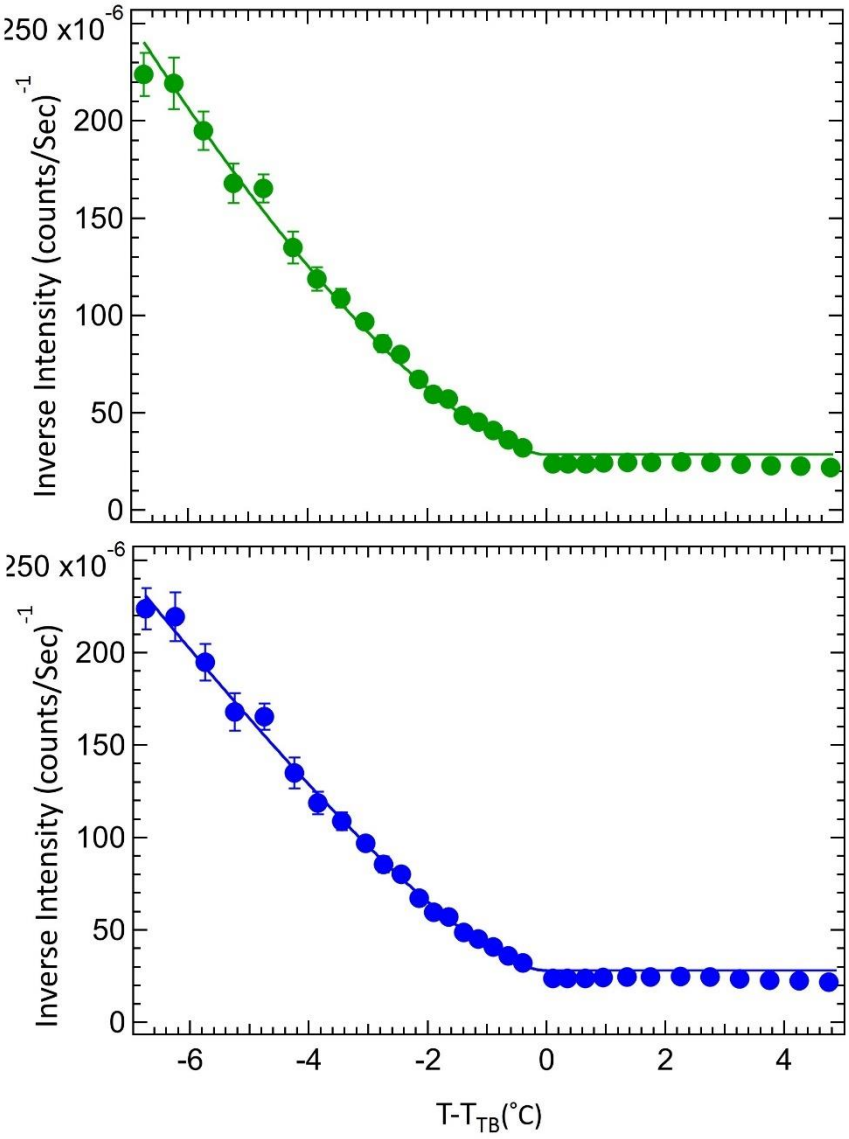

Figure 4-9: Temperature dependence of the inverse scattered intensity $(\mathbf{I_1^t})^{-1}$ from the 70/30 mixture for scattering angle $\boldsymbol{\theta = \theta_m = 40^\circ}$ and rocking angle $\boldsymbol{\chi = 30^\circ}$. The solid line in the top panel is a fit of the data to the *T* dependence predicted by Eq.(4.8) combined with Eqs.(4.6) and (4.7). In the bottom panel, the solid line is a fit of the data to the combination of Eqs.(4.8), (4.5)and (4.6).

case, the fit function for $(I_1^t)^{-1}$ vs T is based on the combination of Eq.(4.8) with Eqs. (4.6) and (4.7), and it again contains three variable parameters.

The quality of the fits in Fig. 4.9 to the two different predictions of the scaling of B_{eff} with p_0 is fairly good, and quite comparable, over the N_{TB} range studied. On the nematic side (B_{eff} = 0), the model assumes the inverse intensity is essentially constant and comes from director mode 1 (i.e., predominantly splay fluctuations of the director). We note that the fit lines are somewhat higher than the inverse intensity data points in the N phase. This can be explained by an additional contribution to the measured intensity coming from director mode 2 (i.e., from the twist-bend director mode), which is only expected to vanish when both $\theta_s = \theta_m$ and $\chi = 0^{\circ}$, whereas our data were taken for $\chi = 30^{\circ}$.

We may also analyze our data for $(I_1^t)^{-1}$ in the N_{TB} phase in a manner that avoids fitting to a function with variable parameters altogether. To present this alternative, let us first summarize the theoretical predictions for the scaling of B_{eff} with $T_{TB} - T$. It is convenient to define a temperature difference ΔT_0 in terms of the coefficients in the free energy for the "polarization wave" model as follows: $\Delta T_0 = 9\Lambda^4 \kappa K_{22}/4\mu_0 \nu K_{33}^4$. Then, when $T_{TB} - T \ll \Delta T_0 -$ i.e., sufficiently close to the transition– Eq.(4.6) gives $p_0 \propto (T_{TB} - T)$, while in the opposite limit, $T_{TB} - T \gg \Delta T_0$, it yields $p_0 \propto (T_{TB} - T)^{1/2}$. Thus for the two scenarios of the "polarization wave" model we get:

Using Eq.(4.5), and

$$B_{eff} \propto p_0^2 \propto \begin{cases} (T_{TB} - T)^2 & (T_{TB} - T) \ll \Delta T_0 \\ (T_{TB} - T) & (T_{TB} - T) \gg \Delta T_0 \end{cases} \tag{4.9}$$

Using Eq.(4.7), and

$$B_{eff} \propto p_0^3 \propto \begin{cases} (T_{TB} - T)^3, & (T_{TB} - T) \ll \Delta T_0 \\ (T_{TB} - T)^{3/2} & (T_{TB} - T) \gg \Delta T_0 \end{cases} \tag{4.10}$$

On the other hand, the coarse-grained "negative bend elasticity" theory of the N–N_{TB} transition predicts a cubic scaling of B_{eff} with $T_{TB} - T$ as $T \longrightarrow T_{TB}$ from below, assuming that the cone angle β is allowed to relax under pseudo-layer compression/dilation [7]. Specifically, this theory gives

$$B_{eff}(T) \propto q_0^2 \sin^2 \beta \propto (T_{TB} - T)^3$$

Next, from Eq.(4.1) for $(I_1^t)^{-1}$, we deduce $[I_1^t(T)^{-1} - I_1^t(T_{TB})^{-1}] \propto B_{eff}(T)$, so that

$$[I_1^t(T)^{-1} - I_1^t(T_{TB})^{-1}]^x \propto T - T_{TB} \tag{4.11}$$

where, depending on the specific expression for B_{eff} in Eqs.(4.9) – (4.11), the exponent *x* is expected to be $\frac{1}{3}, \frac{1}{2}, \frac{2}{3}$, or 1.

Figure 4-10 shows our data for $[I_1^t(T)^{-1} - I_1^t(T_{TB})^{-1}]^x$ vs $T - T_{TB}$ for the three predicted values of *x*. The data are expected to fall on a line, and clearly the plot for $x = \frac{2}{3}$ most accurately does this.

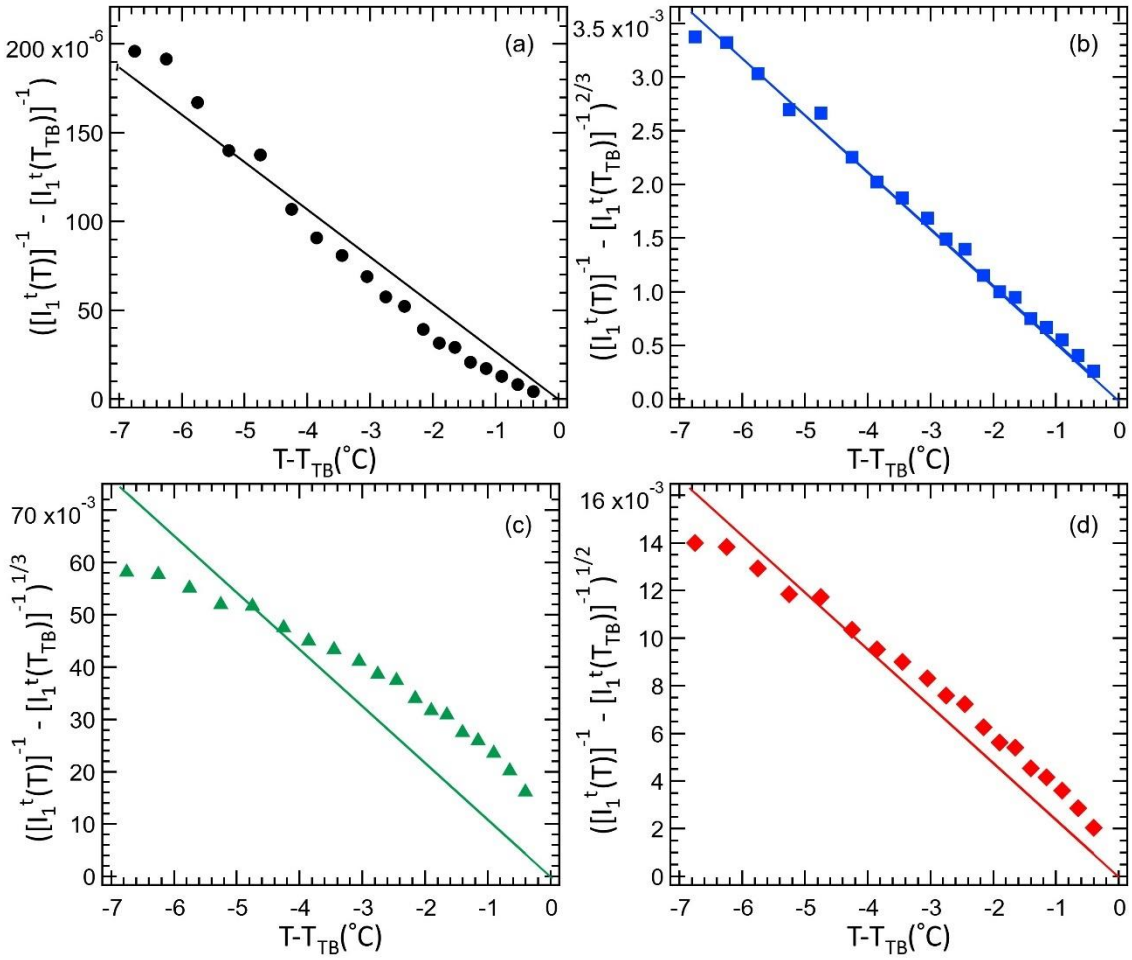

Figure 4-10: The quantity $[I_1^t(T)^{-1} - I_1^t(T_{TB})^{-1}]^x$ calculated from the data in the N_{TB} phase, as a function of $T - T_{TB}$ and a fit to a straight line.(a) $x = 1$ (b) $x = {}^2/_3$ (c) $x = {}^1/_3$ (d) $x = {}^1/_2$.

4.4 SUMMARY

In this Chapter, we presented light scattering measurements of "pseudo-layer" bending/compression fluctuations in the twist-bend nematic phase. We obtained estimates of the pseudo-layer compression modulus B_{eff} in the range $\sim 10^3 - 10^4\ Pa$ (100 – 1000

times smaller than B in a typical smectic-A liquid crystal), confirmed the smectic-A-like q dependence of these fluctuations, and demonstrated agreement between the measured temperature dependence of B_{eff} and predictions of a coarse-grained Landau-deGennes theory of the nematic to N_{TB} phase transition, which features a vector polarization field as the primary order parameter and invokes a linear coupling between this field and bend distortions of the director.

In the next chapter, we will concentrate on the behavior of the orientational elastic constants K_{11}, K_{22}, and K_{33} on the nematic side of the transition in the pure dimer DTC5C9 used in our 70/30 mixture, and in a trimer and tetramer based on the same monomeric building block.

4.5 REFERENCES

[1] C. Meyer, G. R. Luckhurst, and I. Dozov, "The temperature dependence of the heliconical tilt angle in the twist-bend nematic phase of the odd dimer CB7CB," *J. Mater. Chem. C*, vol. 3, no. 2, pp. 318–328, 2015.

[2] I. Dozov, "On the spontaneous symmetry breaking in the mesophases of achiral banana-shaped molecules", *Eur. Lett.*, vol. 56, no. 2, pp. 247–253, 2001.

[3] I. Lelidis and G. Barbero, "Nematic phases with spontaneous splay–bend deformation: standard elastic description," *Liq. Cryst.*, vol. 43, no. 2, pp. 208–215, 2016.

[4] S. M. Shamid, S. Dhakal, and J. V. Selinger, "Statistical mechanics of bend flexoelectricity and the twist-bend phase in bent-core liquid crystals," *Phys. Rev. E*

- *Stat. Nonlinear, Soft Matter Phys.*, vol. 87, no. 5, pp. 1–11, 2013.

[5] E. I. Kats and V. V. Lebedev, “Landau theory for helical nematic phases,” *JETP Lett.*, vol. 100, no. 2, pp. 110–113, 2014.

[6] R. B. Meyer, “Structural problems in liquid crystal physics,” *Les Houches Summer Sch. Theor. Phys.*, 1973.

[7] C. Meyer and I. Dozov, “Local distortion energy and coarse-grained elasticity of the twist-bend nematic phase,” *Soft Matter*, vol. 12, no. 2, pp. 574–580, 2015.

[8] Z. Parsouzi, S. M. Shamid, V. Borshch, P. K. Challa, A. R. Baldwin, M. G. Tamba, C. Welch, G. H. Mehl, J. T. Gleeson, A. Jakli, O. D. Lavrentovich, D. W. Allender, J. V. Selinger, and S. Sprunt, “Fluctuation modes of a twist-bend nematic liquid crystal,” *Phys. Rev. X*, vol. 6, no. 2, pp. 1–16, 2016.

[9] P.G.De Gennes and J.Prost, *The Physics of Liquid Crystals*. Oxford: Clarendon Press, 1993.

[10] R. Schaetzing, PhD dissertation, Massachusetts Institute of Technology, 1980, unpublished.

[11] V. Borshch, Y. K. Kim, J. Xiang, M. Gao, A. Jákli, V. P. Panov, J. K. Vij, C. T. Imrie, M. G. Tamba, G. H. Mehl, and O. D. Lavrentovich, “Nematic twist-bend phase with nanoscale modulation of molecular orientation,” *Nat. Commun.*, vol. 4, pp. 1–8, 2013.

[12] G. P. Chen, H. Takezoe and A. Fukuda, Liq. Cryst., 1989, 5, 341

CHAPTER 5

PRETRANSITIONAL BEHAVIOR OF VISCOELASTIC PARAMETERS AT THE NEMATIC TO TWIST-BEND NEMATIC TRANSITION IN FLEXIBLE N-MERS

5.1 INTRODUCTION

In this chapter, we turn our attention to the nematic side of the $\mathrm{N}-\mathrm{N_{TB}}$ transition. We present a comparative study of the orientational elastic constants K_{11}, K_{22}, K_{33} and associated orientational viscosities in the uniaxial N phase of a homologous dimer, trimer, and tetramer that contain identical, odd parity linkages between the mesogenic units and exhibit a $\mathrm{N}-\mathrm{N_{TB}}$ transition. In addition to measuring these parameters as a function of temperature, we report differences in the pretransitional behavior of a certain subset of them.

The most notable difference occurs in the bend elastic constant K_{33}. After softening on cooling through most of the uniaxial N phase, K_{33} abruptly starts increasing in the dimer and tetramer close to the transition; on the other hand, there is no indication of an increase in K_{33} in the trimer. This observation suggests an odd-even effect of a new type in flexible n-mers.

The associated bend viscosity η_{bend} exhibits a pretransitional enhancement in each of the n-mers, as does the twist elastic constant K_{22}. On the other hand, the splay constant K_{11}, and the corresponding viscosity η_{splay}, show no enhancement. We discuss these results in terms of a coarse-grained theory of the $N - N_{TB}$ transition, which treats the N_{TB} phase as a "pseudo-layered" structure with symmetry equivalent to a smectic-A^* phase, and which maps the coefficients in the associated coarse-grained Landau-deGennes free energy onto those appearing in "local" models – specifically, the "negative elasticity" and "polarization wave" models – that explicitly account for the local heliconical structure.

The measurements on n-mers reported in this chapter differ in an important way from those described for the N phase of the 70/30 dimer/monomer mixture in Chapter 3. In the latter case, the scattering geometries were selected to separate director fluctuations from other fluctuation modes in the N and N_{TB} phases or to separate director fluctuations in the N_{TB} phase that follow "pseudo-layer" motion from those that do not. We did not particularly focus on the isolation of pure splay, twist, or bend fluctuations of the director in the N phase. This will be a priority for the experiments described in the present chapter.

5.2 EXPERIMENTAL DETAILS

5.2.1 STUDIED MATERIALS

The chemical structures and phase sequences of the studied oligomers – dimer 1,5-Bis(2′,3′-difluoro-4″-pentyl-[1,1′:4′,1″-terphenyl]-4-yl)nonane (DTC5C9), its associated trimer (DTC5-C9-DTC-C9-DTC5), and tetramer (DTC5-C9-DTC-C9-DTC-C9-DTC5), as

well as the monomer 2′, 3′-difluoro-4,4″-dipentyl-p-terphenyl (MCT5) – are shown in Figure 5-1. These materials were synthesized and purified by Prof. Georg Mehl's group at the Department of Chemistry, University of Hull, UK, and then supplied to us.

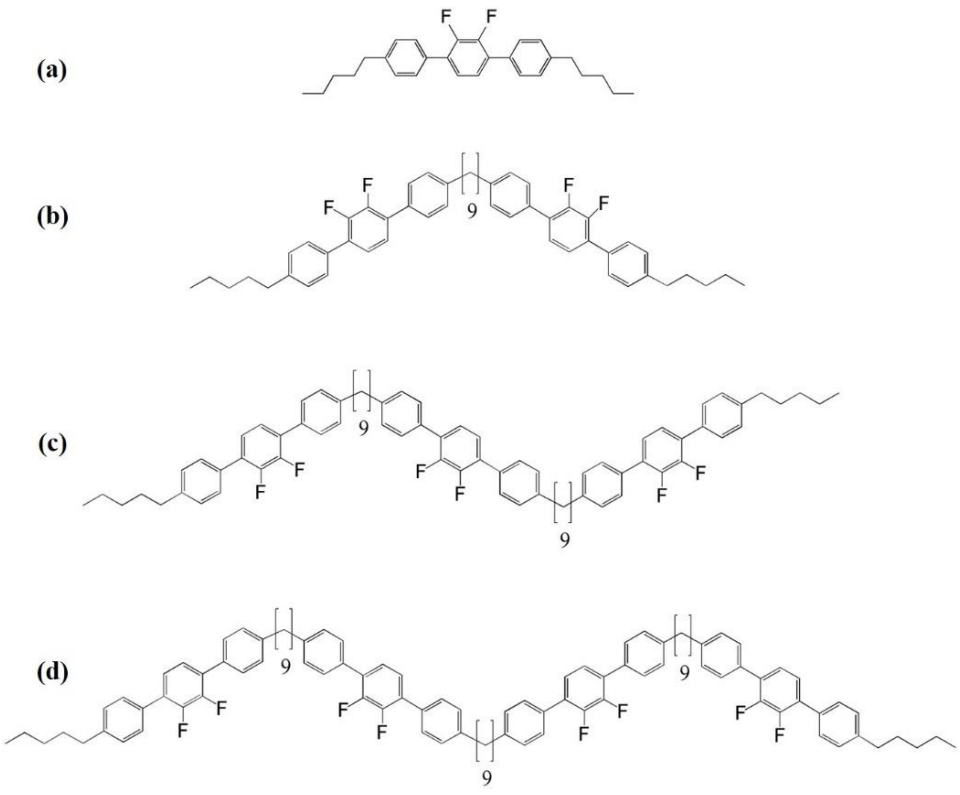

Figure 5-1: Molecular structures of (a) MCT5 monomer, **I** 116.5℃ **N** 34℃ **Cr**, (b) DTC5C9 dimer, **I** 162℃ **N** 124℃ $\mathbf{N_{TB}}$ 85℃ **(SmX)** 77℃ **Cr**, (c) DTC5-C9-DTC-C9-DTC5 trimer, **I** 192℃ **N** 145℃ $\mathbf{N_{TB}}$, (d) DTC5-C9-DTC-C9-DTC-C9-DTC5 tetramer, **I** 205℃ **N** 168℃ $\mathbf{N_{TB}}$.

We conducted polarizing optical microscopy (POM) and dynamic light scattering (DLS) studies on samples of these n-mers contained in optical cells, which were treated for homogeneous planar alignment of the nematic director. Prior to filling each cell, we

determined the gap between the substrates to an accuracy of $\pm 0.1\,\mu m$, using a UV/VIS Spectrometer (PerkinElmer, Lambda18). The sample thicknesses ranged from 4.8 to $17.7\mu m$. For temperature-dependent measurements, the sample cells were placed in an Instec HCS402 hot stage (regulated to a precision of 0.01℃).

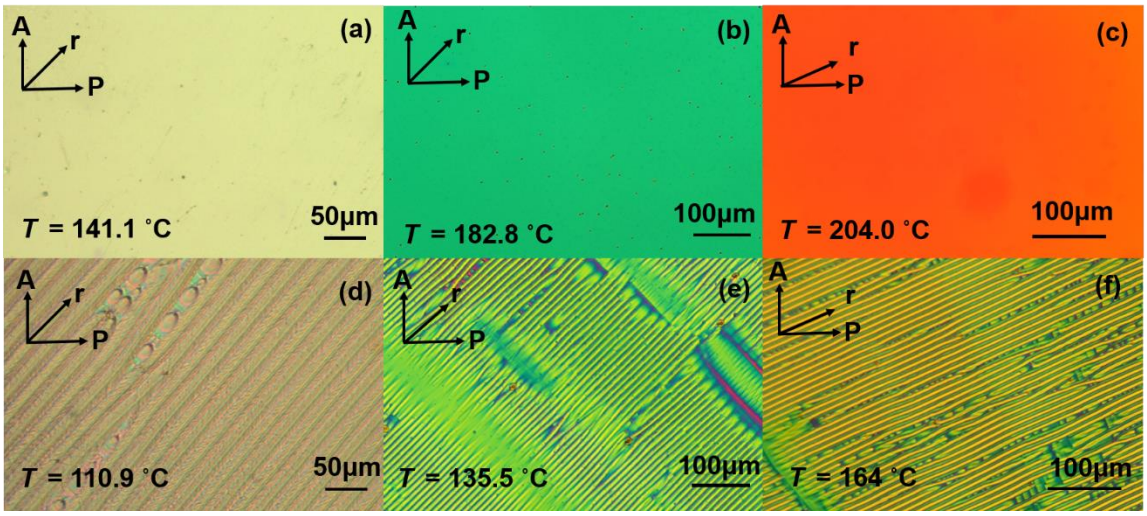

Figure 5-2: POM Polarizing optical microscopy textures of Nematic and N_{TB} phase respectively, the (a,d) dimer, (b,e) trimer and (c,f) tetramer under cross polarizers. The stripes in panels (d,e,f) are characteristic of the twist-bend nematic phase.

The I–N and N–N_{TB} transitions, determined by POM (Figure 5-2), in cooling, were, respectively, 162℃ and 124℃ (dimer), 192℃ and 145℃ (trimer), and 205℃ and 168℃ (tetramer).

5.2.2 LIGHT SCATTERING PROCEDURE AND GEOMETRIES

Because absolute measurements of the scattered light intensity are difficult, DLS is more often used to determine ratios of the elastic constants than to measure absolute values. To enable our study of the magnitudes of the K_{ii}, we prepared a reference sample of the thermotropic nematic 4-noctyloxy-4'-cyanobiphenyl (8OCB), for which accurate, published values of the individual K_{ii} are available [1-3]. A cell containing 8OCB was situated in the same plane in the hot stage as the cells filled with the test n-mers. Both the reference and test cells were assembled from identical sets of substrates treated with identical alignment layers. The reference cell was illuminated by the same incident laser beam ($\sim 4\, mW$ power focused to a waist diameter of $\sim 50\, \mu m$) as the test cells, and scattering was collected and processed with the same combination of pinhole, imaging optics, photomultiplier detectors, and photon counting electronics. The optical textures of both test and reference samples were monitored at all times to ensure that only well-aligned, defect-free volumes were illuminated.

As described in ref [4], measurements of the scattered intensity from pure bend fluctuations were made on the reference and test samples for several temperatures, $T_{NI}-T$, relative to nematic isotropic transition at T_{NI}. Together with accurate determination of the sample thicknesses, measured or published values of the dielectric anisotropy at the various $T_{NI}-T$ and fixed incident light wavelength, and using the calculated expression for the scattered intensity (see sec. 2.4.3 and ref. [4]), we calibrated K_{33} for the test samples against

the literature values for 8OCB. The calibrated K_{33} were then combined with light scattering measurements of the ratios K_{11}/K_{33} and K_{22}/K_{33} to obtain values of K_{11} and K_{22}.

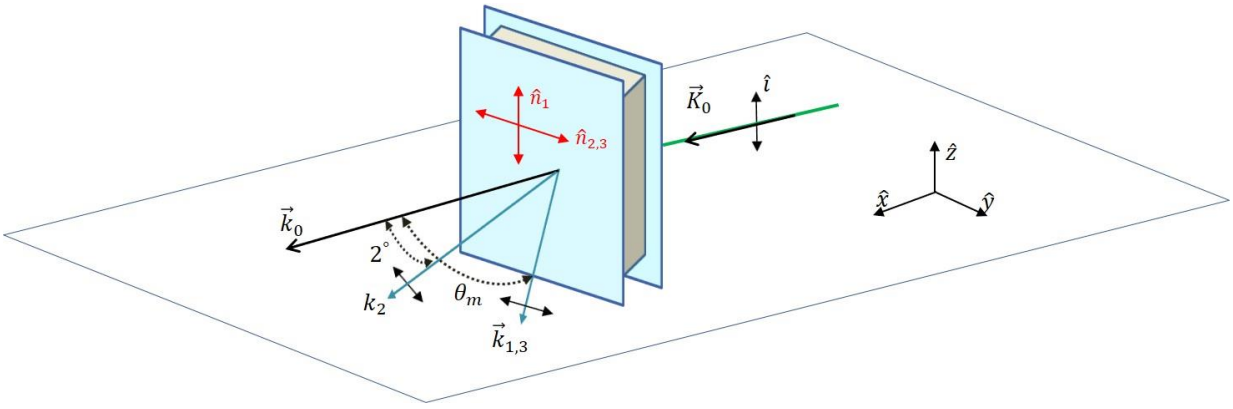

Figure 5-3: Light scattering geometries utilized. Subscripts 1 (3) denote conditions for collection of pure splay (bend) scattering, where the equilibrium director is oriented perpendicular (parallel) to the scattering plane, and scattering angle set to the "magic" angle (see text) for normal incidence. Almost pure twist scattering (subscript 2) is selected when the equilibrium director lies in the scattering plane and the laboratory scattering angle is set to the smallest feasible value (2˚ in our case). In all three cases, the incident and scattered light polarizations (displayed by double-ended arrows) are normal and parallel to the scattering plane, respectively.

For our light scattering measurements, we employed three scattering geometries, shown schematically in Figure 5-3). In each case, the incident light propagated along the cell normal and was polarized perpendicular to the scattering plane, while the scattered light was collected at specific angles off the cell normal and polarized parallel to the plane. These geometries were used to separate out scattering from pure splay, pure bend, and

nearly pure twist fluctuations of the nematic director. The ratios K_{11}/K_{33} and K_{22}/K_{33} can then be determined from the corresponding ratios of the scattered intensities.

In Geometry "1", as we discussed in Sec 3.3.1, the average director is oriented perpendicular to the scattering plane. Pure splay and pure twist contribute to the light scattering for arbitrary scattering angle θ. Choosing θ to be the "magic angle" $\theta_m = \sin^{-1}(n_\perp\sqrt{1-n_\perp^2/n_\parallel^2})$, the scattering factor for the twist fluctuations G_2 in Eq. (3.1) will be zero, and only splay scattering contributes. To calculate θ_m for different temperatures in the N phase of the dimer and trimer, we measured the refractive indices n_e and n_o separately as functions of *T* by the wedge cell technique [5]. For the tetramer, we used the measured Δn and took $n_o = 1.5$, which is extrapolated from the average values of n_o in the nematic phase of the dimer and trimer (1.44 and 1.47, respectively). The calculated values of θ_m vary from $30° - 40°$ over the N range. $\Delta\varepsilon^u$ is optical dielectric anisotropy, T is the absolute temperature, and d is the sample thickness. $G_1(\theta)$ and $G_2(\theta)$ are geometrical scattering factors as defined in Eqs. (2.35). dependent on n_o, n_e and θ.

In Geometries "2" and "3", where the average director lies in scattering plane, the scattering comes from the twist-bend normal mode of director fluctuations [4,6]. The intensity scattered from this mode is $I_s \propto \frac{k_B T}{K_{22}q_\perp^2 + K_{33}q_z^2}$.

Setting the scattering angle to a low value $\theta = 2^\circ$ (Geometry "2"), the ratio $\frac{q_\perp^2}{q_z^2}$ is ≈ 15. Since we also know that $K_{22} \gg K_{33}$ for dimer molecules with odd-membered methylene spacers [7-9], we conclude that $K_{22}q_\perp^2(\theta) \gg K_{33}q_z^2(\theta)$ for $\theta = 2^\circ$, so that, to

an excellent approximation, the scattered intensity can be considered to arise from twist fluctuations alone.

Setting $\theta = \theta_m$ (Geometry "3"), one may show that $q_\perp^2(\theta_m) = 0$ [10], so that only bend fluctuations are probed. Comparing intensities in this case for any of the studied n-mers and the calibration sample of 8OCB gives

$$\frac{[I]_{n-mer}}{[I]_{8OCB}} = \frac{[(\Delta\varepsilon^n)\ d\ T]_{n-mer}}{[(\Delta\varepsilon^n)\ d\ T]_{8OCB}} \frac{\left[\frac{G_2(\theta_m)}{K_{33}q_z^2}\right]_{n-mer}}{\left[\frac{G_2(\theta_m)}{K_{33}q_z^2}\right]_{8OCB}} \tag{5.1}$$

where

$$G_2(\theta) = \frac{n_\perp^2 - \sin^2\theta}{n_\perp^2 + (n_\perp^2/n_\parallel^2 - 1)\sin^2\theta} \tag{5.2}$$

In Eq. (5.1), $\Delta\varepsilon^n = n_\parallel^2 - n_\perp^2$ is the optical dielectric anisotropy, d is the sample thickness, T is the absolute temperature, $n_\perp$ and $n_\parallel$ are the principal refractive indices of a uniaxial nematic, and the quantities $n_\perp$, $n_\parallel$, and K_{33} are evaluated at $T_{NI} - T$– i.e., at the same temperature relative to the N–I transition. Eqs. (5.1) and (5.2) allow us to determine K_{33} for the n-mer from literature values of $n_\perp$, $n_\parallel$, and K_{33} for 8OCB, and measured values of $n_\perp$ and $n_\parallel$ for the n-mer.

To measure orientational viscosities associated with director fluctuations in the N phase, we recorded the time correlation function of the scattered light intensity in each scattering geometry. Fitting these data to an exponential decay in time yields the relaxation rates Γ for the director fluctuations probed (see Eq. (2.24)). The orientational viscosities, which are combinations of the Leslie and Miesowicz viscosities of a uniaxial nematic, are

given by Eq. (2.25). For scattering geometries "1" and "3" described above, our measured values of the elastic moduli and the fitted relaxation rates enable us to calculate the orientational viscosities for pure bend and splay fluctuations as [4,11]:

$$\eta_{splay} = \frac{K_{11} q_\perp^2}{\Gamma_1} = \eta_1(q_z = 0) = \gamma_1 - \frac{\alpha_3^2}{\eta_b} \tag{5.3}$$

$$\eta_{bend} = \frac{K_{33} q_z^2}{\Gamma_3} = \eta_2(q_\perp = 0) = \gamma_1 - \frac{\alpha_2^2}{\eta_c} \tag{5.4}$$

where Γ_1 and Γ_3 are the relaxation rates measured in geometries "1" and "3", and $\gamma_1, \alpha_2, \alpha_3, \eta_b, \eta_c$ are fundamental viscosities of the nematic fluid discussed in standard texts [4,6].

In geometry "2" for small scattering angle $\theta = 2^\circ$ and $\frac{q_\perp^2}{q_z^2} \approx 15$, the orientational viscosity becomes [4,6],

$$\eta_{twist-bend} = \frac{K_{22} q_\perp^2}{\Gamma_2} = \eta_2(q_\perp^2 \approx 15 q_z^2) \approx \gamma_1 - \frac{\alpha_2^2}{\eta_a}\frac{q_z^2}{q_\perp^2} \approx \gamma_1 - \frac{\alpha_2^2}{15\eta_a} \tag{5.5}$$

In contrast to the situation with the elastic constants, the orientational viscosity $\eta_{twist-bend}$ cannot be reasonably approximated by the pure twist contribution ($\eta_{twist} = \gamma_1$), since the value of $\frac{\alpha_2^2}{\eta_a}$ is typically rather large. For example, using reported values of α_2 and η_a for the standard monomeric calamitic 5CB [12], we have $\frac{\alpha_2^2}{\eta_a} = 0.22$ Pa.s at a temperature 10℃ below isotropic-nematic transition, which means that in 5CB $\frac{\alpha_2^2}{15\eta_a}$ is 16% of the reported

value of $\gamma_1 = 0.08$ Pa-s. Thus, in the following section we report the orientational viscosity given in Eq. (5.5), and do not claim that this well approximates $\eta_{twist} = \gamma_1$.

5.3 RESULTS

As Figure 5-2 shows, the aligned uniaxial N phase of each n-mer exhibits a uniform optical texture. At lower temperatures, optical stripes, parallel to the average director, nucleate and grow. These stripes are associated with buckling of the N_{TB} "pseudo-layers" resulting from the strain produced as the heliconical pitch ("pseudo-layer" spacing) rapidly contracts with decreasing temperature [13-15]. The N to N_{TB} transition is signaled by a well-defined propagating front observed in cooling by POM at a temperature slightly above the point where the stripe pattern develops; such a clearly delineated front is consistent with a first-order phase transition[16].

While direct measurements of the nanoscale structure are not yet available for the pure n-mers, previous FFTEM results[13] on mixtures of the DTC5C9 dimer with its monomeric building block (MCT5) clearly reveal a nanoscale periodic orientational modulation, as well as periodic textural arches (asymmetric Bouligand arches), that confirm the twist-bend nature of the modulation. Additionally, resonant X-ray scattering (RXS), which is capable of detecting molecular scale orientational modulations in the absence of a mass density wave, has confirmed a periodic structure consistent with the N_{TB} phase in the DTC5C9 dimer with Se atoms substituted on opposing ends of the monomeric cores [17].

Figure 5-4 presents our DLS measurements for the temperature dependence of the orientational elasticities K_{11}, K_{22} and K_{33} in the nematic phase of the homologous dimer, trimer and tetramer studied. In order to display the temperature dependence over a uniform range that is convenient for comparison among the n-mers, we plot the results against the reduced temperature $(T - T_{TB})/(T_{NI} - T_{TB})$. As T decreases, the splay constant K_{11} increases through the full nematic range for all three n-mers, and does not exhibit anomalous pretransitional behavior in the vicinity of the N—N_{TB} transition. For decreasing T, the twist constant K_{22} also increases, but additionally shows a significant pretransitional enhancement near T_{TB}.

The temperature dependence of the bend constant K_{33} reveals an interesting difference among the n-mers. With decreasing T below the N−I transition, K_{33} first decreases monotonically in all the n-mers. In the dimer and tetramer, K_{33} reaches a minimum above the N−N_{TB} transition and then begins to increase up to the transition to the N_{TB} phase. By contrast, K_{33} for the trimer levels off at a minimum value close to T_{TB} and shows no pretransitional increase.

The temperature-dependence of the ratio K_{11}/K_{22} is presented in Figure 5-4 (d). For the trimer and tetramer, this ratio exceeds 2 over the full nematic range, as is expected theoretically for n-mers that exhibit the N_{TB} phase [18]. The ratio skews slightly downward close to the both the N−N_{TB} and N−I transitions. The dimer shows similar behavior, although the ratio drops below 2 close to the transitions. The reason for the downward trend

as $T \rightarrow T_{TB}$ is the pretransitional increase of K_{22} relative to K_{11} (Figure 5-4 (b) vs Figure 5-4(a)).

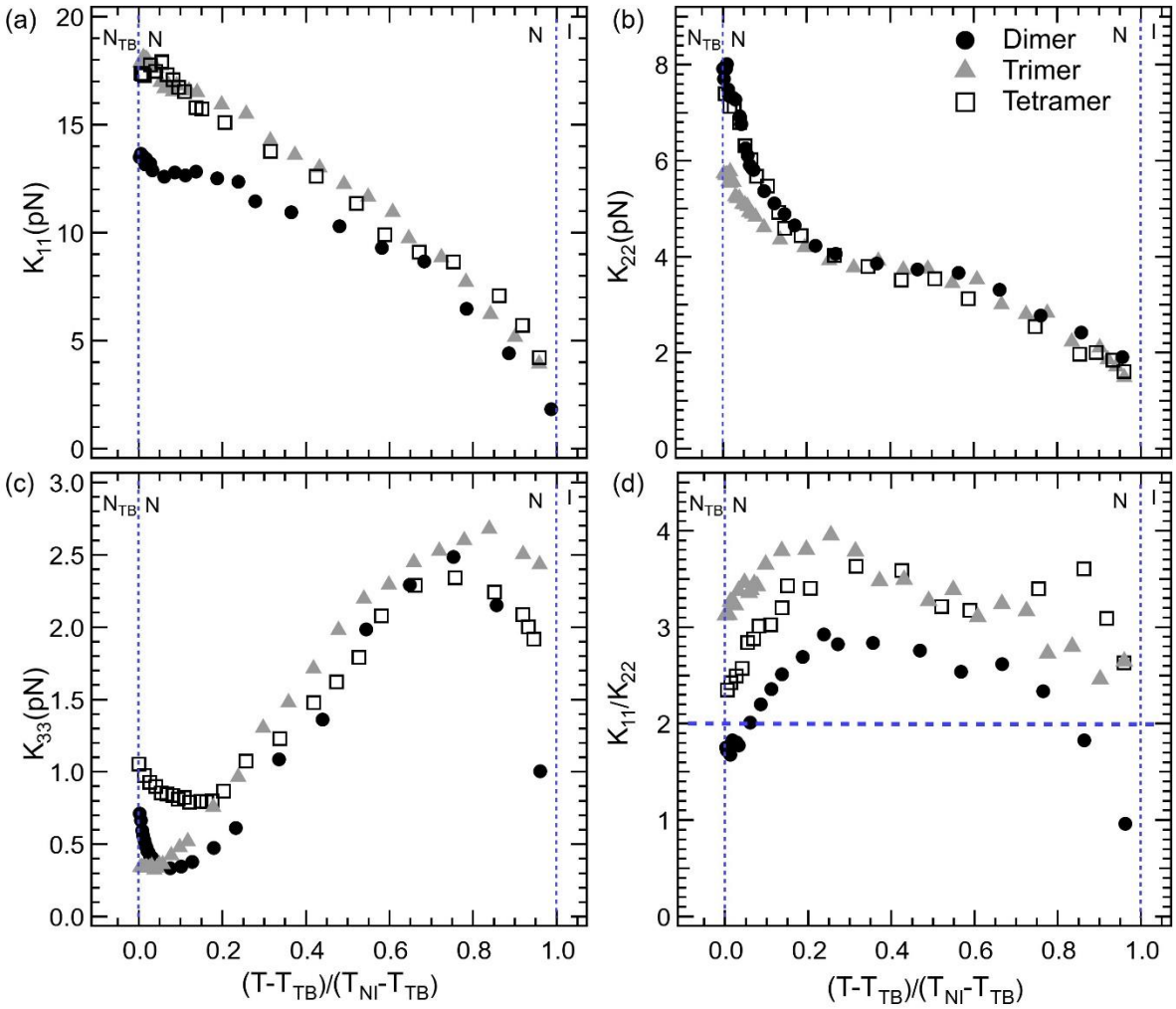

Figure 5-4: Reduced temperature dependences of the nematic elastic constants. (a) – (c): Splay (K_{11}), twist (K_{22}), and bend (K_{33}) constants for the dimer, trimer, and tetramer; (d): The ratio K_{11}/K_{22} with the theoretical threshold value for a N_{TB} phase indicated by a horizontal dashed line.

As we will discuss in the next section, this increase results from renormalization of the "bare" K_{22} due to fluctuating pseudolayer domains. Approaching T_{NI}, differences in the

detailed dependences of K_{11} and K_{22} on nematic order parameter S may produce a downward shift in their ratio as $T \rightarrow T_{NI}$. The criterion $K_{11}/K_{22} > 2$ for a twist-bend modulation is based on "bare" values of K_{11} and K_{22}— i.e., values corresponding to well-developed nematic order but no significant impact of pretransitional N_{TB} fluctuations. In this domain of Figure 5-4 (d), the measured K_{11}/K_{22} clearly exceeds 2 for all three n-mers.

Figure 5-5 displays the temperature dependence of the orientational viscosities η_{splay}, $\eta_{twist-bend}$, and η_{bend} (given in Eqs. (5.3) – (5.5)) in the N phase. With decreaing *T*, the viscosities grow monotonically, with η_{bend} showing the most pronounced pretransitional increase as $T \rightarrow T_{TB}$. This increase is more marked in the dimer and tetramer than in the trimer. We observe that η_{bend} is much smaller than the other two viscosities, as is normally found in rod-shaped monomeric nematics.

According to standard nematohydrodynamics [6], we expect the pure twist viscosity $\eta_{twist} = \gamma_1$ to exceed η_{splay} (although they usually have comparable magnitudes in rod-like nematics). Our measurement of $\eta_{twist-bend}$ is systematically lower than η_{splay} (Figure 5-5 (d)). However, $\eta_{twist-bend}$ contains a q −dependent mixture of the twist viscosity γ_1 and other fundamental viscosities, including the Miesowicz viscosities that are associated with the coupling of shear flow to the director motion. If the Miesowicz viscosities are sufficiently anisotropic, a small contribution of bend to the scattering from the twist-bend mode (small component of q_z in the scattering vector) could significantly depress $\eta_{twist-bend}$ toward the much lower value of η_{bend}. Thus, our experimental result

$\eta_{twist-bend} < \eta_{splay}$ in Figure 5-5 (d) is not unexpected and does not indicate a definite departure from the normal behavior in uniaxial nematics.

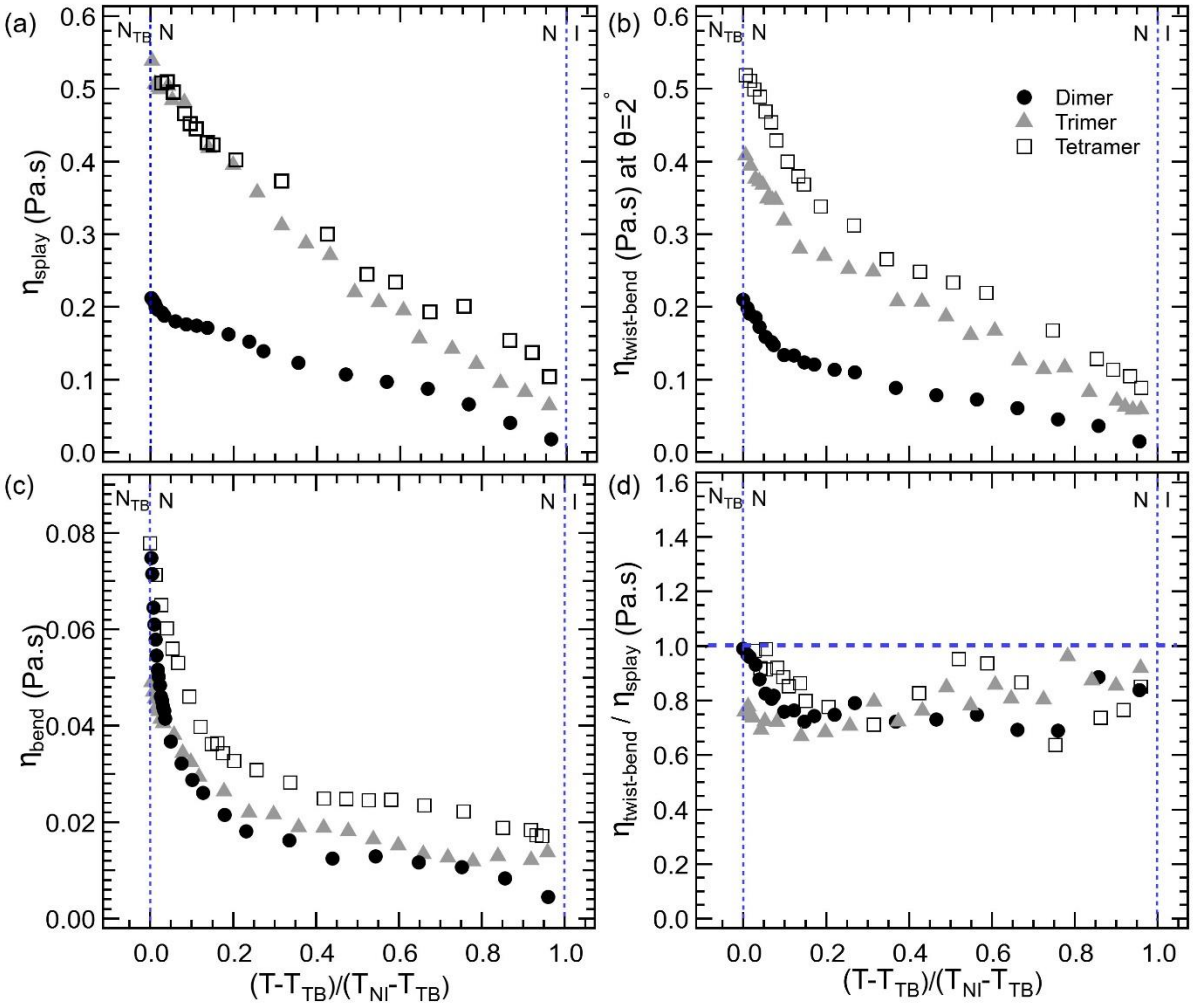

Figure 5-5: Reduced temperature dependences of the nematic orientational viscosities in the studied n-mers. (a) – (c): η_{splay}, $\eta_{twist-bend}$, η_{bend}; (d): The ratio $\eta_{twist-bend}/\eta_{splay}$.

For completeness, we present in Figure 5-6 DLS data for the viscoelastic parameters in the N phase of the monomer MCT5 Figure 5-1(a), plotted versus reduced temperature $(T - T_{NCr})/(T_{NI} - T_{NCr})$ where T_{NCr} is the temperature of the nematic to crystal transition that occurs in this material (Recall the monomer does not exhibit the N_{TB} phase). Both the elastic constants and viscosities data exhibit conventional behavior in the N phase, with $K_{33} \geq K_{11} > K_{22}$ and $\eta_{twist-bend} \geq \eta_{splay} \gg \eta_{bend}$ (where again $\eta_{twist-bend}$ is dominated by twist). Each of the elasticities and viscosities increase systematically with decreasing temperature, as expected.

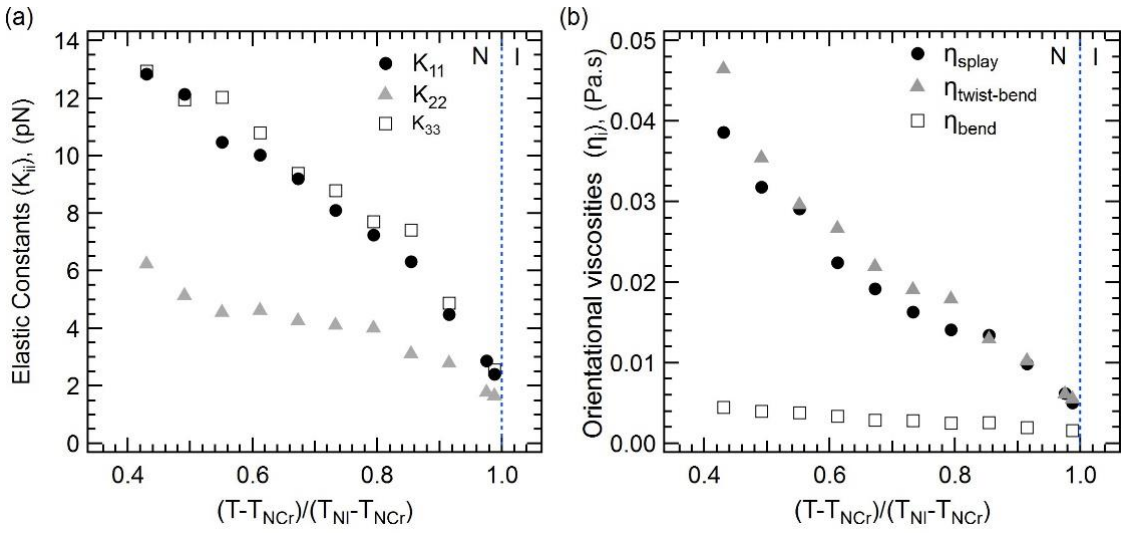

Figure 5-6: Elastic constants (a) and viscosities (b) as a function of reduced temperature in the N phase of the monomer MCT5. T_{NCr} is the temperature of the nematic to crystal transition.

Combining our data for the monomer and higher n-mers allows us to compare the magnitudes of the nematic elastic constants over the $n = 1 - 4$ homologous series and, in

particular, to compare the measured values to certain predictions for the scaling of these parameters with the length of the n-mer. For flexible elongated ("rodlike") oligomers, and accounting only for entropic effects (which is probably more appropriate for lyotropic than for thermotropic systems), the splay constant K_{11} is expected to scale as $\bar{L}/D$ [19], where $\bar{L}$ is the average extended length of the oligomer, and D is its diameter. On the other hand, for flexible rods, the twist constant K_{22} is expected to scale with the persistence length λ_p – or characteristic length over which unit vectors tangent to the rod lose their correlation – as $K_{22} \sim (\lambda_p/D)^{\frac{1}{3}}$ [20]. If $\lambda_p \lesssim \bar{L}$, K_{22} should be basically insensitive to increases in length. Finally, the bend constant should increase with $\bar{L}$ until $\bar{L} \simeq \lambda_p$, where it should saturate. However, we cannot apply this prediction to our system, since for $n > 1$, K_{33} is profoundly affected over the full nematic range by developing N_{TB} -type correlations. These play the dominant role in the behavior of K_{33}, and are outside the scope of the arguments used to make the scaling predictions.

Fig. 5.7 plots K_{11} and K_{22} versus $T - T_{NI}$ for the n-mers $n = 1 - 4$, down to temperatures just above regime where K_{22} starts increasing due to the developing N_{TB} correlations. The plots provide a direct comparison for different *n* at the same temperature relative to the N–I transition, as opposed to the plots against the reduced temperature $(T - T_{NTB})/(T_{NI} - T_{NTB})$ in Fig. 5.4. (The latter is more useful for contrasting the N–N_{TB} pretransitional behavior of the K_{ii} for different n, but is not appropriate for comparing magnitudes at similar $T - T_{NI}$.).

We observe that away from the N–I transition, when the nematic order is well established, the values of K_{22} do not vary systematically with *n*. This result is consistent with the flexible rod model, provided λ_p in our flexible n-mers is comparable to the length of a single rigid core unit.

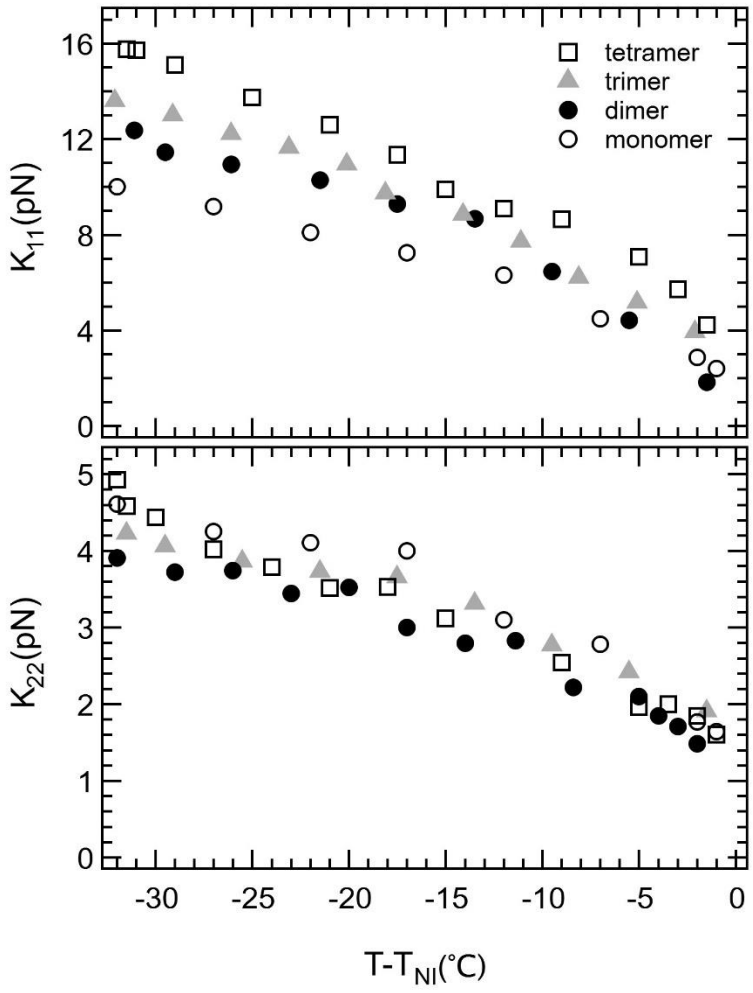

Figure 5-7: Splay ($\mathbf{K_{11}}$, top panel) and twist ($\mathbf{K_{22}}$, bottom panel) elastic constants plotted as a function of temperature relative to the nematic-isotropic transition for the studied n-mers.

By contrast, for values of $T - T_{NI}$ well into the nematic phase, K_{11} shows a systematic increase with *n*, though the increase is considerably weaker than one would expect if $\bar{L} \propto n$ and $K_{11}(n)/K_{11}(n=1) \simeq n$. For example, in the middle of the nematic range in Fig. 5.7 (at $T - T_{NI} = -17$℃), $K_{11}(\mathrm{n}=4)/K_{11}(\mathrm{n}=1) = 1.54$ and $K_{11}(n=2)/K_{11}(n=1) = 1.27$.

A similar result, $K_{11}(n=2)/K_{11}(n=1) = 1.20$ at $T - T_{NI} = -5$℃, was reported by DiLisi et al [21] for a different thermotropic monomer-dimer system. They proposed an explanation for the weaker than expected scaling with n based on including both end-end molecular interactions between n-mers and the excluded volume associated with the molecular ends, in addition to the entropy of mixing "top" and "bottom" ends on which the scaling $K_{11} \propto \bar{L} \propto n$ is predicated. The model including non-entropic interactions qualitatively accounts for the weaker dependence of K_{11} on n between thermotropic monomers and dimers, which our results suggest extends up to $n = 4$. In fact, results reported on a 24-mer, where $K_{11}(n=24)/K_{11}(n=1) \approx 10$ [22], indicate the simple scaling relation may not be accurate even for fairly long thermotopic oligomers. Finally, we should add that in n-mers composed of alternating rigid and flexible elements, the conformational relation between these elements may possibly depend on n, providing another reason why the overall length $\bar{L}$ would not necessarily increase linearly with n.

5.4 DISCUSSION

In the following discussion, we will compare the pretransitional behavior of the orientational viscoelastic parameters to the predictions of a coarse-grained model of the N to "pseudo-layered" N_{TB} phase transition. A coarse-grained theory is appropriate for analyzing experimental results when the experiment probes length scales significantly greater than the N_{TB} pitch p_0 – a condition that certainly holds for light scattering, since the optical wavelength is ~50 times larger than p_0.

Let us therefore consider the impact of fluctuating "pseudo-layered" N_{TB} domains close to the transition. In Chapter 4, we mentioned recent theoretical work [23,24] exploring a symmetry-based analogy between the N_{TB} and chiral smectic-A (SmA*) phases and between the N-–N_{TB} and N—SmA* phase transitions. In place of the usual smectic order parameter $\Psi = \Psi \exp(iq_0u)$, where Ψ is the amplitude of the smectic density wave and u is the local smectic layer displacement from equilibrium, one may define a pseudo-layer order parameter for the N_{TB} phase as $\sigma = \sin\beta\, e^{i\delta\emptyset}$, where β is the tilt angle of the local director $\hat{n}$ away from the average heliconical axis $\hat{z}$, and $\delta\emptyset$ is the deviation of the phase of $\hat{n}$ from its equilibrium value. The pseudo-layer spacing is the helical pitch, $p_0 = 2\pi/q_0$.

A coarse-grained Landau–de Gennes expansion of the free energy density for the N–N_{TB} transition can then be written down in terms of the pseudo-layer order parameter and coarse-grained director $\hat{t}$ (unit vector along the heliconical axis), in direct analogy to the conventional expansion for the N–SmA* transition. The Landau coefficients and elastic

constants appearing in this coarse-grained free energy density should be determined from averaging, over single pitch, a “local" model for the free energy of the N—N_{TB} transition — i.e., a model that describes how the nanoscale heliconical structure develops. One such model, proposed by Dozov [18], is the “negative elasticity" model. In this model, the energy of a uniaxial nematic is extended to include fourth order gradients in the director field, thus permitting one or more of the second-order elastic coefficients to become negative and thereby favor a non-uniform local director field. Specifically, the bend elastic constant K_{33} is assumed to be temperature dependent, $K_{33} = k_{33}^0(T - T^*)$, where k_{33}^0 is a material constant. When *T* decreases below T^*, K_{33} becomes negative, destabilizing the N phase against bend distortion of the director. To accommodate this bend without defects, the system may transition to either a twist-bend or splay-bend phase. The positive fourth order elastic terms stabilize the structure for a finite amplitude of the bend distortion. If the “bare" second-order nematic twist and splay constants are related by $K_{11} > 2K_{22}$, as we noted in the previous section for the studied n-mers, the twist-bend phase is favored. In that case, the fourth-order elasticity reduces to a single effective elastic constant *C* [18].

Dozov and Meyer [23,24] have presented the details of averaging the free energy in the “negative elasticity" model, and connecting its coefficients to the coarse-grained model, on the N_{TB} side of the transition. To compare with our experimental results, we need to follow their approach for the high temperature side (N phase). Once the relations between coefficients in the two models are determined, one can address the question of the pretransitional behavior of orientational elasticities and viscosities using standard results

for the nematic to smectic-A transition and employing the specific relations between coefficients.

According to de Gennes' original analysis [25,26] of the N–SmA transition, the pretransitional enhancements of the elastic constants arising from pretransitional fluctuations in smectic order are given by

$$\delta K_{11} \approx 0 \tag{5.6}$$
$$\delta K_{22} \propto \frac{\xi_{\perp}^2}{\xi_{\parallel}}$$
$$\delta K_{33} \propto \xi_{\parallel}$$

where $\xi_{\perp}$, $\xi_{\parallel}$ are temperature-dependent correlation lengths specifying the typical size of a fluctuating, pretransitional smectic domain. No pretransitional enhancement is expected for the splay constant; K_{11} should only exhibit a gradual increase due to its dependence on the nematic order parameter, $K_{11} \sim S^2$. However, K_{22} and K_{33} are expected to increase sharply due to the growth of the correlation lengths near the transition. Within mean-field theory and after employing the mapping of Landau coefficients between the local and coarse grained models of the N—N_{TB} transition, we obtain the following expressions for the correlation lengths, which apply to pseudo-layered N_{TB} domains above the transition [27]:

$$\xi_{\perp} = \sqrt{\frac{K_{11} + K_{22}}{2(K_{33} + Cq_0^2)}}\frac{1}{q_0} \approx \sqrt{\frac{K_{11} + K_{22}}{2[k_{33}^0 + Cq_0^{2'}(T_{TB})](T - T_{TB})}}\frac{1}{q_0} \tag{5.7}$$
$$\xi_{\parallel} = \frac{1}{q_0}$$

In these expressions, we assume q_0 (and therefore the pseudolayer spacing ($p_0 = 2\pi/q_0$) could be temperature-dependent on the high temperature side of the transition (i.e., within pretransitional pseudo-layer domains). The second expression for $\xi_\perp$ is obtained after expanding $q_0^2(T)$ around the transition temperature T_{TB} and keeping terms to linear order in $T - T_{TB}$; it is therefore accurate close to T_{TB}. The quantity $q_0^{2\prime}(T_{TB})$ is the first derivative of q_0^2 evaluated at T_{TB}, and the transition temperature is given by $T_{TB} = T^* - C\, q_0^2(T_{TB})/k_{33}^0$, where k_{33}^0 and T^* are parameters in the expression assumed for the temperature-dependent bend elastic constant: $K_{33} = k_{33}^0(T - T^*)$.

The alternative "local" model of the N_{TB} phase – the "polarization wave" model [28] described in Chapters 3 and 4 – expresses the Landau–de Gennes free energy as the sum of a standard Landau expansion of a polarization field $\vec{p}$ to fourth order, a gradient term in $\vec{p}$ with effective elastic constant κ, a bilinear coupling between $\vec{p}$ and bend distortions of the director field $\hat{n}$ with coupling coefficient $-\lambda$, and the standard second order Frank elastic energy for distortions in $\hat{n}$. One can show [27] that the polarization wave model produces results for the correlation lengths close to the transition that have the same T and q_0 dependence as in Eq. (5.7), but we will not go into the details here.

We now compare the predictions of Eqs. (5.6) and (5.7) to our experimental results for the nematic elastic constants K_{ii} in the studied n-mers. Strictly speaking, the theoretical results apply to a second order transition, while our optical observations of a propagating front indicate a weakly first order transition. Thus we may expect the predicted pretransitional behavior of the K_{ii} to be cut off at the actual transition temperature T_{TB}.

Let us first note that in agreement with the prediction of the coarse-grained model, the data for the splay constant K_{11} in Fig. 5.4(a) show no notable pretransitional behavior as $T \longrightarrow T_{TB}$. Second, Eqs. (5.6) and (5.7) imply

$$\frac{\delta K_{22}}{\delta K_{33}} \propto \left(\frac{\xi_{\perp}}{\xi_{\parallel}}\right)^2 \propto \frac{1}{T - T_{NTB}}$$

which indicates that K_{22} should exhibit a stronger pretransitional increase than K_{33}. The data for the dimer and tetramer in Figs. 5.4(b) and 5.4(c) are consistent with this prediction, although the observable increases in K_{22} are limited due to the first-order nature of the transition. In the dimer, where both K_{22} and K_{33} increase sharply close to T_{TB}, we note that in cooling the slope of K_{22} vs T starts increasing at a significantly higher temperature than the slope of K_{33}. This is consistent with a stronger temperature dependence of δK_{22}.

The third, and perhaps most illuminating, point of comparison centers on the prediction $\delta K_{33} \propto \xi_{\parallel} = 1/q_0(T)$ and the different pretransitional behaviors observed for the bend constant among the n-mers. (Note again that we allow for the possibility of a temperature-dependent q_0 associated with the fluctuating N_{TB} domains above the transition.) In the dimer, K_{33} decreases on cooling through the bulk of the N phase (Fig. 5.4(c)), as expected from both "local" models of the N—N_{TB} transition. It then turns sharply upward near $T \longrightarrow T_{TB}$. Based on the prediction $K_{33} \propto 1/q_0(T)$, this suggests a significant pretransitional decrease in q_0 as $T \longrightarrow T_{TB}$ from above. Carbon-edge [29] and selenium-edge [17] RXS experiments on dimers – the latter on compounds closely related to DTC5C9 – show that q_0 also decreases as $T \longrightarrow T_{TB}$ from below the transition. The

combination of results suggests that in N_{TB}-forming dimers, q_0 has significant T dependence on both sides of the transition.

By contrast, our data for K_{33} (Fig. 5.4(c)) in the homologous trimer reveal no pretransitional enhancement, which would be consistent with $q_0 \approx$ const in the expression for δK_{33} and a fixed (or weakly temperature-dependent) q_0 in the fluctuating N_{TB} domains above T_{TB}. In addition, the pretransitional increase of K_{22} is weaker in the trimer compared to the dimer (Fig. 5.4(b)), as expected according to Eqs. (5.6) and (5.7) whereby δK_{22} is also proportional to $1/q_0$. Interestingly, recent carbon-edge RXS results on a different trimer [30] demonstrate that $q_0 \approx$ const in the N_{TB} phase as well. Thus, in N_{TB}-forming trimers, q_0 might be a weakly temperature-dependent material parameter.

Finally, our measurements of K_{33} in the tetramer (Fig. 5.4(c)) are consistent with a T-dependent q_0 that decreases in the N phase as $T \longrightarrow T_{TB}$ (though evidently more weakly than in the dimer). Correspondingly, new carbon-edge RXS data on tetramers demonstrate a temperature-dependent, decreasing q_0 as the transition is approached on the N_{TB} side [31]. We can now speculate that the differences in pretransitional behavior of K_{22} and K_{33} between even ($n = 2,4$) and odd ($n = 3$) n-mers are fundamentally connected to the temperature dependence (or lack thereof) of the wavenumber q_0 characterizing the heliconical modulation.

We now turn to the pretransitional behavior of the orientational viscosities presented in Figure 5-5 .All of the measured viscosities increase with decreasing temperature through the bulk of the N phase, as expected for an activated (Arrhenius)

temperature dependence. Close to T_{TB}, however, their behavior exhibits clear differences, which we can compare to expectations from the coarse-grained theory of the transition.

For a conventional nematic–smectic-A transition, the singular contributions to these viscosities have been calculated as [32] $\delta\eta_{bend} = \delta\eta_{twist} = \delta\gamma_1$ and $\delta\eta_{splay} = 0$, where γ_1 is the viscosity for pure rotation of the uniaxial nematic director. In the mean field approximation [32,33], $\delta\gamma_1 \propto 1/(a\xi_{\parallel})$, where a is the leading Landau coefficient in the conventional free energy density for the N—SmA transition. Using the analogy developed above, we then find $\delta\gamma_1 \propto 1/[(T - T_{NTB})q_0]$, in the case of the "negative elasticity" model close to the transition. A similar result applies for the "polarization wave" model close to the transition.

The data in Figure 5-5(a) for η_{splay} show no definite evidence of a singular contribution close to the transition, in agreement with the prediction $\delta\eta_{splay} = 0$. On the other hand, η_{bend} is expected to diverge as $T \longrightarrow T_{TB}$, which is consistent with the definite pretransitional enhancement that we observe for this viscosity (Fig. 5.5(c)). Moreover, unlike the case of the bend elastic constant K_{33}, η_{bend} is still expected to diverge even if q_0 is temperature-independent. Thus, for the trimer, the absence of a pretransitional effect on K_{33} (attributed to fixed q_0) and the presence of one in η_{bend} are fully consistent with the coarse-grained theory and, in particular, with the N_{TB} /SmA* analogy on which it is based.

Our data for the viscosity $\eta_{twist-bend}$, which is dominated by twist, show much weaker evidence of pretransitional enhancement than η_{bend}. Although this appears to be

inconsistent with the prediction above, it may simply be that over the accessible pretransitional range, the enhancement of the twist viscosity is small compared to the non-singular part of $\eta_{twist-bend}$, which is nearly 10 times larger than the non-singular component of η_{bend}. A more accurate measurement of pure twist fluctuations would clarify the issue.

5.5 SUMMARY

We measured the orientational elastic constants and associated viscosities of homologous n-mers for $n = 1 - 4$ through the nematic range and including the pretransitional region above the nematic to twist-bend nematic phase transition for $n = 2 - 4$. The ratio of splay to twist elastic constants exceeds 2 in the majority of the nematic range for the three oligomers ($n = 2 - 4$); this satisfies a theoretical criterion for the occurrence of the twist-bend nematic phase at lower temperature. The bend and twist elastic constants show sharp enhancements close to the N—N_{TB} transition in even n-mers (dimer and tetramer), while in the odd n-mer (trimer) the bend constant shows no pretransitional increase. The splay constant shows no notable enhancement in any n-mer. Among the orientational viscosities, the bend viscosity exhibits strong pretransitional enhancement in the even n-mers and a somewhat weaker enhancement in the odd n-mer.

We discussed the pretransitional behavior of the viscoelastic parameters in terms of a coarse-graining of two proposed “local" models of the N_{TB} phase, which results in a free energy density analogous that for the nematic to smectic-A transition. The analysis of

our experimental results in this framework suggests that the wavenumber characterizing heliconical fluctuations in the N phase depends significantly on temperature in the dimer and tetramer as the N–N_{TB} transition is approached, but remains essentially constant in the trimer. At a qualitative level, we found generally good agreement between the observed pretransitional behavior of the viscoelastic parameters and the expected behavior based on the analogy between the N to "pseudo-layered" N_{TB} and conventional N to smectic-A (or A*) transitions.

5.6 REFERENCES

[1] M. Bradshaw and P. Raynes, *J. Phys. Fr.*, 1985, 46, 1513–1520.

[2] N. V. Madhusudana and R. Pratibha, *Molecular Crystals and Liquid Crystals*, 1982, 89, 249–257.

[3] B. Kundu, R. Pratibha and N. V. Madhusudana, *Phys. Rev. Lett.*, 2007, 99, 247802.

[4] G. Babakhanova, Z. Parsouzi, S. Paladugu, H. Wang, Y. A. Nastishin, S. V. Shiyanovskii, S. Sprunt and O. D. Lavrentovich, *Phys. Rev. E*, 2017, 96, 062704.

[5] J. K ˛edzierski, Z. Raszewski, M. A. Kojdecki, E. KruszelnickiNowinowski, P. Perkowski, W. Piecek, E. Miszczyk, J. Zielinski, ´ P. Morawiak, and K. Ogrodnik, *Opto-Electron Rev.* 18, 214 ,2010.

[6] P. G. de Gennes and J. Prost, *The Physics of Liquid Crystals*, Clarendon Press, Oxford, UK, 2nd edn., 1993.

[7] K. Adlem, M. Čopič, G. R. Luckhurst, a. Mertelj, O. Parri, R. M. Richardson, B. D. Snow, B. a. Timimi, R. P. Tuffin and D. Wilkes, *Phys. Rev. E*, 2013, 88, 022503.

[8] G. Cukrov, Y. M. Golestani, J. Xiang, Yu. A. Nastishin, Z. Ahmed, C. Welch, G. H. Mehl, and O. D. Lavrentovich, *Liq. Cryst*. 44, 219 ,2017.

[9] N. Sebastian, M. G. Tamba, R. Stannarius, M. R. de la Fuente, M. Salamonczyk, G. Cukrov, J. Gleeson, S. Sprunt, A. Jakli, C. Welch, Z. Ahmed, G. H. Mehl, and A. Eremin, *Phys. Chem. Chem. Phys.* 18, 19299 ,2016.

[10] M. Majumdar, P. Salamon, A. Jakli, J. T. Gleeson, and S. Sprunt, *Phys. Rev. E* 83, 031701, 2011.

[11] R. Borsali, D. Y. Yoon, and R. Pecora, *J. Phys. Chem. B* 102, 6337, 1998.

[12] M. Cui, Doctoral dissertation, Kent State University, 2000.

[13] V. Borshch, Y. K. Kim, J. Xiang, M. Gao, A. Jákli, V. P. Panov, J. K. Vij, C. T. Imrie, M. G. Tamba, G. H. Mehl and O. D. Lavrentovich, *Nat. Commun.*, 2013, 4, 2635-1–8.

[14] V. P. Panov, R. Balachandran, M. Nagaraj, J. K. Vij, M. G. Tamba, a. Kohlmeier and G. H. Mehl, *Applied Physics Letters*, 2011, 99, 261903.

[15] C. Meyer, G. R. Luckhurst and I. Dozov, *J. Mater. Chem. C*, 2015, 3, 318.

[16] M. A. Anisimov, P. E. Cladis, E. E. Gorodetskii, D. A. Huse, V. E. Podneks, V. G. Taratuta, W. Van Saarloos and V. P. Voronov, *Phys. Rev. A*, 1990, 41, 6749–6762.

[17] W. D. Stevenson, Z. Ahmed, X. B. Zeng, C. Welch, G. Ungar and G. H. Mehl, *Phys. Chem. Chem. Phys.*, 2017, 19, 13449–13454.

[18] I. Dozov, *Eur. Lett.*, 2001, 56, 247–253.*Fr.*, 1985, 46, 1513–1520.

[19] V. G. Taratuta, F. Lonberg and R. B. Meyer, *Phys. Rev. A*, 1988, 37, 1831R–1834R.

[20] T. Odijk, *Liquid Crystals*, 1986, 1, 553–559.

[21] G. A. DiLisi, C. Rosenblatt, A. C. Griffin and U. Hari, *Liquid Crystals*, 1990, 8, 437–443.

[22] S. Zheng-Min and M. Kleman, *Mol. Cryst. Liq. Cryst*., 1984, 111, 321–328.

[23] C. Meyer and I. Dozov, *Soft Matter*, 2016, 12, 574–580.

[24] I. Dozov and C. Meyer, *Liquid Crystals*, 2017, 44, 4–23.

[25] P. G. de Gennes, *Solid State Communications*, 1993, 88, 1039– 1042.

[26] P. G. de Gennes, *Mol Cryst Liq Cryst*, 1973, 21, 49–76.

[27] Z. Parsouzi, G. Babakhanova, M. Rajabi, R. Saha, P. Gyawali, T. Turiv, H. Wang, A. R. Baldwin, C. Welch, G. H. Mehl, J. T. Gleeson, A. Jakli, Oleg D. Lavrentovich, and Samuel Sprunt*, Physical Chemistry Chemical Physics*, 2019.

[28] S. M. Shamid, S. Dhakal and J. V. Selinger, *Phys. Rev. E*, 2013, 87, 052503.

[29] C. Zhu, M. R. Tuchband, A. Young, M. Shuai, A. Scarbrough, D. M. Walba, J. E. Maclennan, C. Wang, A. Hexemer and N. A. Clark, *Physical Review Letters*, 2016, 116, 147803.

[30] M. R. Tuchband, D. A. Paterson, M. Salamończyk, V. A. Norman, A. N. Scarbrough, E. Forsyth, E. Garcia, C. Wang, J. M. D. Storey, D. M. Walba, S. Sprunt, A. Jákli, C. Zhu, C. T. Imrie, and N. A. Clark, *PNAS*, 1821372116, 2019

[31] M. Salamonczyk, ´ unpublished.

[32] F. Jähnig and F. Brochard, *Journal de Physique*, 1974, 35, 301–313.

[33] D. Langevin, *J. Phys. Fr.*, 1976, 37, 901.

CHAPTER 6

CONCLUSION

In this dissertation, we used dynamic light scattering (DLS) to explore the twist-bend nematic (N_{TB}) phase in liquid crystalline oligomers. Specially selected scattering geometries were employed to characterize temperature-dependent hydrodynamic and nonhydrodynamic fluctuations modes associated with the N_{TB} structure. We demonstrated good agreement between the observed behavior of these modes and theoretical predictions based on a "coarse-grained" version of a Landau-de Gennes free energy for the nematic-to- N_{TB} transition. The coarse-graining approximation, appropriate in the limit of helical pitch much shorter than an optical wavelength, treats surfaces of constant phase in the heliconical structure as "pseudo-layers". Within this approximation, the fluctuation modes may be mapped onto those of a smectic-A phase, with an effective layer spacing equal to the pitch of the heliconical N_{TB} structure, an effective director parallel to the local pitch axis, and effective elastic constants that arise due to the short-pitch orientational modulation rather than from a true mass density wave.

We found that additional, fast orientational fluctuations observed in our experiments could be explained by the presence of a helical polarization field, which accompanies the heliconical director structure in the N_{TB} phase and which fundamentally distinguishes the N_{TB} phase from the other known nematic states, including, in particular, the cholesteric phase.

We also measured the effective "pseudo-layer" compression elastic constant, B_{eff}, in the N_{TB} phase, obtaining values in the range 10^3–10^4 Pa, or ~10^2–10^3 times lower than in the values for a smectic-A phase where the layer structure is defined by a true mass density wave. Our experimental results for the dispersion and temperature dependence of the hydrodynamic fluctuation mode validate the ''pseudo-layer'' description and quantitatively support a Landau-deGennes theory of the nematic to N_{TB} transition, which invokes a polarization field as the primary order parameter.

Finally, we compared the temperature dependencies in the nematic phase of the orientational elastic constants and corresponding viscosities in a homologous series of liquid crystal dimer, trimer, and tetramer containing odd-numbered hydrocarbon linkages between identical mesogenic groups. Each exhibits characteristic signatures of the N_{TB} phase at temperatures below the conventional nematic state. We discussed the observed pretransitional behavior of these viscoelastic parameters at the nematic to N_{TB} transition in the framework of the "pseudo-layered" N_{TB} / smectic-A analogy. At a qualitative level, we found generally good agreement between the observed pretransitional behavior of the viscoelastic parameters and the behavior expected from the symmetry-based analogy between nematic–N_{TB} and conventional nematic–smectic-A phase transitions. Our results also suggest that the wavenumber characterizing the "pseudo-layer" structure in pretransitional N_{TB} domains is temperature-dependent in the "even" n-mers (dimer and tetramer) but essentially constant in the "odd" n-mer (trimer) – hinting at a possible, new "odd-even" effect in homologous liquid crystal n-mers.

For the future, it would be interesting to pursue similar studies in different homologous n-mer series, perhaps extending to higher n (pentamers and hexamers). It would also be intriguing to make mixtures of n-mers (with $n > 1$) and the corresponding monomer, with the aim of identifying a true second-order nematic–N_{TB} transition. This would allow one to make a quantitative comparison of the measured pretransitional behavior of viscoelastic parameters to the available theoretical predictions (which so far only treat the case of a second-order transition). A modulated nematic phase with similar long wavelength symmetry to the twist-bend phase is the splay-bend phase, which is theoretically favored to occur in n-mers if the energy of twist distortions of the director sufficiently exceeds the energy of splay distortions. Light scattering studies of the fluctuation modes in a splay-bend phase – and an assessment of similarities to, and differences from, their nature or behavior in the twist-bend phase – would further advance our understanding of the fascinating physics and variety of structural states exhibited in liquid crystalline materials.